Unione Europea

PON Ricerca e Innovazione 2014- 2020

Ministero dell'Istruzione, dell'Università e della Ricerca

Dottorato di Ricerca in Ingegneria dei Prodotti e dei Processi Industriali

PhD in Industrial Product and Process Engineering - XXX Cycle

Imparting Superhydrophobic Properties through Janus Wrinkled Silica-gel Particles

MSc. Joshua Avossa

Department of Chemical, Materials and Production Engineering (DICMaPI)

Università degli Studi di Napoli Federico II

Tutors:

Prof. Francesco Branda

Prof. Giuseppe Mensitieri

ABBREVIATIONS

ACA	Apparent contact angle
AFM	Atomic force microscopy
APTES	Aminopropyltriethoxysilane
ATR	Attenuated total reflectance
CA	Contact angle
cmc	Critical micellar concentration
CPB	Cetylpiridinium Bromide
CTAB	Cetyltrimethylammonium bromide
DCDMS	Dichlorodimethylsilane
DLS	Dynamic light scattering
IR	Infrared
JWSP	Janus Wrinkled Silica-gel Particle
Mn	number average molecular weight
Mw	weight average molecular weight
O/W	oil in water
PDMS	Polydimethylsiloxane
PPgMA	Maleic anhydride-graft-polypropylene
PS	Polystyrene

$\bar{r}$	Average radius
rpm	Revolutions per minute
SEM	Scanning electron microscopy
TEM	Transmission electron microscopy
TEOS	Tetraethoxysilane
XPS	X-ray photoelectron spectroscopy
Z-pot	Zeta potential

1. SUPERHYDROPHOBIC SURFACES

1.2 SUPERHYDROPHOBICITY

In this Section, definition and properties of superhydrophobic surfaces are briefly defined. For further details about describing models, that correlate the surfaces parameters (surface tension and morphology) with liquid wettability parameters (contact angle, contact angle hysteresis and roll-off angle), see Section 2.2.

1.2.1 DEFINITIONS AND PARAMETERS DEFINING WETTABILITY

When a droplets of liquid is laid on a surface, the profile of the droplets forms with the surface plane an angle between the liquid-surface interface plane and the tangent plane of the droplets at the solid-liquid-gas point, called contact angle (Figure 1.1).

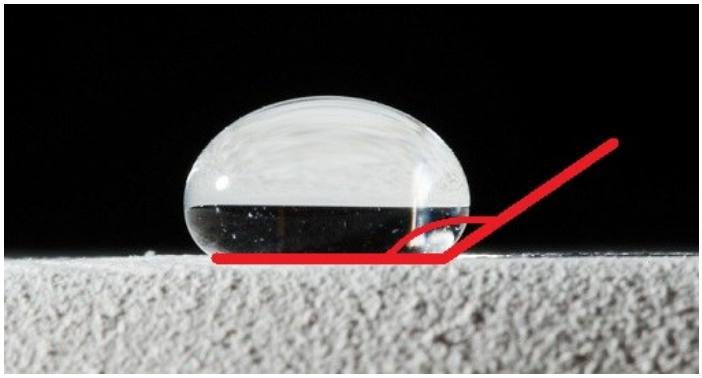

Fig. 1.1. Picture of a liquid droplet on a solid surface. In red, contact angle is underlined.

When water has a good affinity with the surface, the contact angle value is less than 90°. In this case, the surface is considered hydrophilic. If the wettability or the affinity of the liquid with the surface lows, the liquid dislikes the surface and the contact area reduces and consequently the contact angle increases. When water forms contact angle more than 90° the surface is

considered hydrophobic. At first glance, contact angle can be used as a directly measurable parameter for evaluating the wettability or the affinity of liquids to the surfaces.

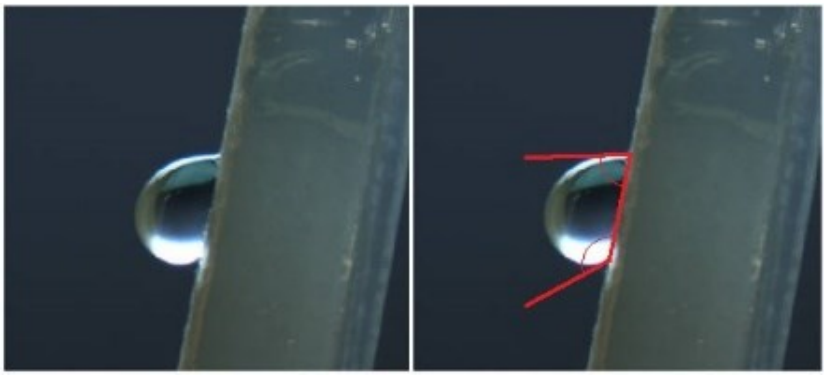

Fig. 1.2. Picture of a droplet moving onto an inclined surface (left) and the same picture showing the advancing and receding contact angles in red (right).

Achieving high slippery behaviour is possible only realizing surfaces that exhibit with liquid high contact angle values. An example of high repellence against water is showed by superhydrophobic surfaces. Superhydrophobicity is a surface related behaviour that manifests particular effects on water droplets in contact with the surface. Indeed, the droplets very easily roll-off from the superhydrophobic surfaces even at small inclination of the surface and very unlikely stick on such surfaces.

This behaviour depends both on the contact angle, that is usually more than 150°, and on the hysteresis of the contact angle. The latter parameter depends on the surface-liquid adhesion energy, and is defined as the difference of the contact angle measured during sliding or rolling off from the surface, or rather, the difference between downhill or advancing contact angle and the uphill or receding contact angle (figure 1.2). Superhydrophobic surfaces exhibit with water low hysteresis contact angle value, usually less than 5°, that together with high contact angle values cause an easy rolling off from the surface.

1.2.2 SUPERHYDROPHOBICITY IN NATURE

In nature, surfaces possessing high repellence to the water have something in common: hierarchical roughness; i.e. a surface with more than one length scale of texture, consisting of a finer length scale texture on an underlying coarser length scale of texture.

In figure 1.3 is reported some pictures of lotus leafs with microscopic details of the surface. The leaves are covered by ten microns bumps (convex cell papilla) completely covered by hundreds nanometers pillars (epicuticular wax crystals). The bumps at microns scale and the finer roughness made of the pillars, together with the low surface tension of the wax covering the surface, achieve superhydrophobicity. The outcome of the hierarchical texture enables the leaf to obtain self-cleaning properties. Or rather, dust particles on the surface are entrapped in the droplets of water during rolling off, carrying away the dust and perfectly cleaning the surface. The cleaning mechanism is illustrated in figure 1.4.

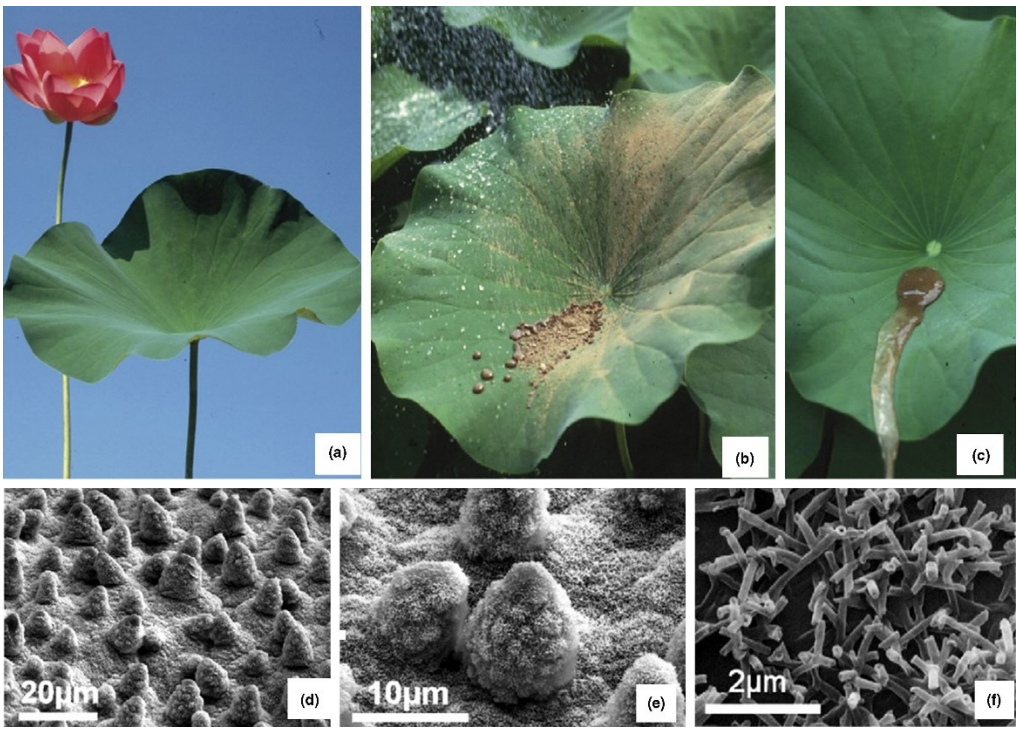

Fig. 1.3. Lotus leaf picture (a), and self-cleaning behaviour shown during raining (b) that completely clean the leaf surface (c). Micrographs of surface morphological details at

different magnifications are depicted (d,e,f), showing the cell papilla (e) and epicuticular wax crystal (f). [1].

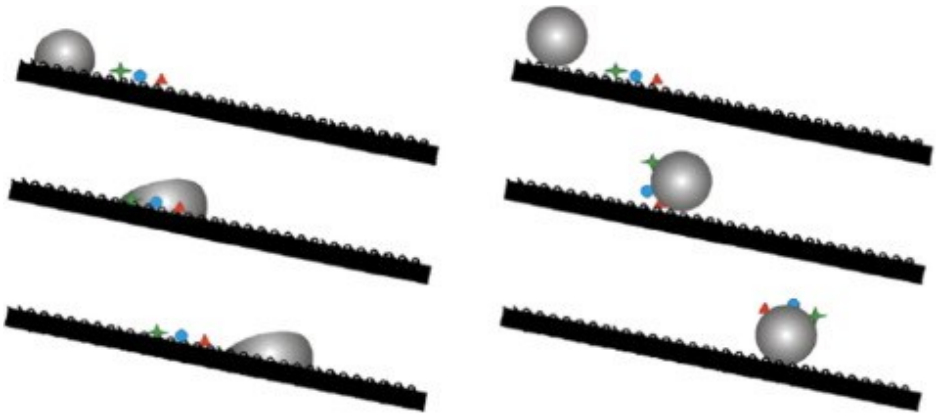

Fig. 1.4. Liquid droplet passing onto dust particles (green cross, blue circle and red triangle) on a normal surface (left) and a superhydrophobic surface (right). In the latter, Particles adhere at the droplet surface during rolling off and carrying them away.

Nature takes advantage of hierarchical low surface texture achieving superhydrophobicity in many situation: anti-bacterial properties of the bug's wings [2], slide abilities of some insects on water (water strider etc.) [3,4], water-repellent of feathers [5], anti-adhesion properties of some skin-breathing arthropods [6,7].

Researches about bio-inspired superhydrophobic surfaces are spread in the past decades, to mimic the interesting properties that nature achieved in hundreds of years.

1.2.3 PROCESSESS: SURFACE PATTERNING AND MODIFICATION

Herewith, the common processes involving formation of superhydrophobic and superolephobic surfaces (high slippery behaviour of apolar liquids) are discussed.

In past few decades, an increasing interest in the hierarchical surfaces manufacturing to achieve superhydrophobic and superomniphobic surface is raised. The possible processes can be divided in different categories.

If the formation of hierarchical texture is realized by adding material on the surface the processes involve techniques that spread materials that organize themselves in a hierarchical textured layer. Usually these techniques are: spraying [8,9], dip-coating [10–12], spin-coating [13,14], plasma spraying [15], gas aggregation cluster technique [16], thermal oxidation [17], electrohydrodynamics [18–22], etc. Usually such materials added on top of the substrate are not sufficient to achieve superhydrophobicity because sometimes the surface tension is not low enough. Therefore, a further step as a chemical modification is needed.

A different approach is removing material from the surface. During the removing process the technique creates the hierarchical demanded structures, i.e., lithography [23–25], solvent extraction [26], chemical etching [27]; in other cases, like plasma etching [28–30], material removing and surface chemistry modification happen simultaneously to build the hierarchical texture and reduce the solid-gas surface tension.

Usually formation of superhydrophobic surfaces is a multi-step procedure that involves more than one approach listed above. For instance, lithography and etching can be used together to produce masks for creating template for feature replication of omniphobic polymer membranes [31]. Xu et al. produced a transparent superhydrophobic coating by spreading polystyrene and silica sol onto a glass substrate by sol-gel dip-coating, then, after annealing of the polymer part a volcano-like structure is formed on top of the glass substrate[32].

1.2.4 MECHANICAL RESISTENT AND SELF-HEALING SURFACES

The main concern about superhydrophobic is the lack of mechanical resistance of the rough structure. Indeed, because of the structure full of pores and re-entrants, superhydrophobic surfaces are usually fragile. Therefore, in the past years an important objective during production of high slippery surfaces is the durability in term of mechanical resistance. The difficulty in achieving this goal depends on the performance of the slippery surface: the higher

the amount of pores and re-entrants the higher the contact angle but the weaker is the surface resistance to mechanical stresses.

Recently, many researchers tried to obtain surfaces with higher mechanical resistance. Zhang et al. obtained superhydrophobic behaviour on an elastic polydimethylsiloxane support, that can tolerate continuous impact of water droplets and knife scratches without modifying its superhydrophobicity [33]. Chen et al. produced a mechanical resistant superhydrophobic surface on paper, glass, metallic and polymeric supports by spraying an adhesive layer and then a nanoparticles dispersion on the substrates. Mechanical abrasion cycles and knife scratches tests on the supports do not change the superhydrophobic properties [34]. Golovin et al. produced an abrasion resistant (1 km of cycle) coating made of a polymer binder and 1H,1H,2H,2H-heptadecafluorodecyl polyhedral oligomeric silsesquioxane (F-POSS) as hydrophobic filler by spraying blends of the two compounds [9]. Sheng et al produced a electrospun waterproof membrane made of polyacrylonitrile and hydrophobic nanoparticles that resist to abrasion tests [22].

Another approach to improve durability of superhydrophobic surfaces is to introduce within the surface material low surface tension molecules in order to impart self-healing properties. In fact, any surface, no matter how durable, is susceptible to physical (and chemical) damages. During the damage, the low surface energy molecules preferentially migrate to the solid-air interface, restoring superhydrophobic behaviour.

Wu et al prepared an abrasion durable and self-healable superhydrophobic cotton fabric. The slippery behaviour can survive after thousands of abrasion cycles, and superhydrophobicity can be restored by simply stream ironing [35]. Liu et al used polydopamine nanocapsules containing octadecylamine molecules to impart superhydrophobicity to fabrics. When the surface fabric is destroyed by physical damages and lose its liquid repellency, octadecylamine migrates to the surface and restore superhydrophobicity [36].

1.2.5 APPLICATIONS

Anti-sticking, water slippery behaviour and self-cleaning property are features that nature exploited in different situations, as we saw in the subsection 1.2.2. Researchers all around the world are finding a way to exploit the interesting features of superhydrophobic surfaces for different applications.

A straightforward application for superhydrophobic surfaces is the production of self-cleaning glass [10] (automobile and aircrafts windshields, camera lenses, touch screens, solar panels, etc.) [37] and fabrics [36].

Very interesting is the application of superhydrophobic coatings in the infrastructures field, such as building material, marbles and sandstone: they can provide protection from environmental pollution and acid rain [38]. The coatings can be used for anti-icing purpose for roads and power lines in cold countries, providing economic and safety benefits [39].

As these surfaces are water resistant, hence they also resist the anchoring and growth of microorganisms on them. Thus their anti-fouling and anti-bacterial properties [40] are also expected to be remarkable. For instance, if applied to medical devices they can reduce infections and contaminations risks[41]. They can be applied as protective coatings on surfaces exposed to sea water, because otherwise they get easily covered by algae and other marine organisms [42]. Superhydrophobic surfaces can be used in microreactors and microfluidic devices [43] and for drag reduction [44], and in many other fields: high-density integrated circuit production [45], oil water separation [34], water collection[46], waterproof-breathable membranes [22], and so on.

References

[1] K. Koch, B. Bhushan, W. Barthlott, Multifunctional surface structures of plants: An inspiration for biomimetics, Prog. Mater. Sci. 54 (2009) 137–178. doi:10.1016/j.pmatsci.2008.07.003.

[2] E.P. Ivanova, J. Hasan, H.K. Webb, V.K. Truong, G.S. Watson, J.A. Watson, V.A. Baulin, S. Pogodin, J.Y. Wang, M.J. Tobin, C. Lobbe, R.J. Crawford, Natural bactericidal surfaces: mechanical rupture of Pseudomonas aeruginosa cells by cicada wings., Small. 8 (2012) 2489–2494. doi:10.1002/smll.201200528.

[3] J.W.M. Bush, D.L. Hu, M. Prakash, The Integument of Water-walking Arthropods: Form and Function, 2007. doi:10.1016/S0065-2806(07)34003-4.

[4] D.L. Hu, B. Chan, J.W.M. Bush, The hydrodynamics of water strider locomotion., Nature. 424 (2003) 663–666. doi:10.1038/nature01793.

[5] E. Bormashenko, O. Gendelman, G. Whyman, Superhydrophobicity of Lotus Leaves versus Birds Wings: Different Physical Mechanisms Leading to Similar Phenomena, Langmuir. 28 (2012) 14992–14997. doi:10.1021/la303340x.

[6] R. Helbig, J. Nickerl, C. Neinhuis, C. Werner, Smart skin patterns protect springtails, PLoS One. 6 (2011) e25105. doi:10.1371/journal.pone.0025105.

[7] J. Nickerl, M. Tsurkan, R. Hensel, C. Neinhuis, C. Werner, The multi-layered protective cuticle of Collembola: a chemical analysis, J. R. Soc. Interface. 11 (2014). doi:10.1098/rsif.2014.0619.

[8] L. Xiong, L.L. Kendrick, H. Heusser, J.C. Webb, B.J. Sparks, J.T. Goetz, W. Guo, C.M. Stafford, M.D. Blanton, S. Nazarenko, D.L. Patton, Spray-deposition and photopolymerization of organic-inorganic thiol-ene resins for fabrication of superamphiphobic surfaces, ACS Appl. Mater. Interfaces. 6 (2014) 10763–10774. doi:10.1021/am502691g.

[9] K. Golovin, M. Boban, J.M. Mabry, A. Tuteja, Designing Self-Healing Superhydrophobic Surfaces with Exceptional Mechanical Durability, ACS Appl. Mater. Interfaces. 9 (2017) 11212–11223. doi:10.1021/acsami.6b15491.

[10] J. Bravo, L. Zhai, Z. Wu, R.E. Cohen, M.F. Rubner, Transparent Superhydrophobic Films Based on Silica Nanoparticles Transparent Superhydrophobic Films Based on Silica Nanoparticles, 23 (2007) 7293–7298. doi:10.1021/la070159q.

[11] Y. Wang, Y. Zhu, C. Zhang, J. Li, Z. Guan, Transparent, superhydrophobic surface with varied surface tension responsiveness in wettability based on tunable porous silica structure for gauging liquid surface tension, ACS Appl. Mater. Interfaces. 9 (2017) 4142–4150. doi:10.1021/acsami.6b12779.

[12] J. Nine, T.T. Tung, F. Alotaibi, D.N.H. Tran, D. Losic, Facile Adhesion-Tuning of Superhydrophobic Surfaces between “ Lotus ” and “ Petal ” E ff ect and Their In fl uence on Icing and Deicing Properties, (2017). doi:10.1021/acsami.6b16444.

[13] S. Jiang, M.J. Schultz, Q. Chen, J.S. Moore, S. Granick, Solvent-free synthesis of janus colloidal particles, Langmuir. 24 (2008) 10073–10077. doi:10.1021/la800895g.

[14] Y. Lee, E.-A. You, Y.-G. Ha, Transparent, self-cleaning and waterproof surfaces with tunable micro/nano dual-scale structures, Nanotechnology. 27 (2016) 355701. doi:10.1088/0957-4484/27/35/355701.

[15] N. Sharifi, M. Pugh, C. Moreau, A. Dolatabadi, Developing hydrophobic and superhydrophobic TiO2 coatings by plasma spraying, Surf. Coatings Technol. 289 (2016) 29–36.

doi:10.1016/j.surfcoat.2016.01.029.

[16] M. Petr, J. Hanuš, O. Kylián, J. Kratochvíl, P. Solař, D. Slavínská, H. Biederman, Superhydrophobic fluorine-free hierarchical coatings produced by vacuum based method, Mater. Lett. 167 (2016) 30–33. doi:10.1016/j.matlet.2015.12.126.

[17] R. Weng, H. Zhang, L. Yin, W. Rong, Z. Wu, X. Liu, Fabrication of superhydrophobic surface by oxidation growth of flower-like nanostructure on a steel foil, RSC Adv. 7 (2017) 25341–25346. doi:10.1039/c6ra28239c.

[18] A. Tuteja, W. Choi, J.M. Mabry, G.H. McKinley, R.E. Cohen, Robust omniphobic surfaces., Proc. Natl. Acad. Sci. U. S. A. 105 (2008) 18200–18205. doi:10.1073/pnas.0804872105.

[19] L. Jiang, Y. Zhao, J. Zhai, A lotus-leaf-like superhydrophobic surface: A porous microsphere/nanofiber composite film prepared by electrohydrodynamics, Angew. Chemie - Int. Ed. 43 (2004) 4338–4341. doi:10.1002/anie.200460333.

[20] Q. Yang, L.I. Zhenyu, Y. Hong, Y. Zhao, S. Qiu, C.E. Wang, Y. Wei, Influence of solvents on the formation of ultrathin uniform poly(vinyl pyrrolidone) nanofibers with electrospinning, J. Polym. Sci. Part B Polym. Phys. 42 (2004) 3721–3726. doi:10.1002/polb.20222.

[21] L. Ye, J. Guan, Z. Li, J. Zhao, C. Ye, J. You, Y. Li, Fabrication of Superhydrophobic Surfaces with Controllable Electrical Conductivity and Water Adhesion, Langmuir. 33 (2017) 1368–1374. doi:10.1021/acs.langmuir.6b03848.

[22] J. Sheng, Y. Xu, J. Yu, B. Ding, Robust Fluorine-Free Superhydrophobic Amino-Silicone Oil/SiO2 Modification of Electrospun Polyacrylonitrile Membranes for Waterproof-Breathable Application, ACS Appl. Mater. Interfaces. 9 (2017) 15139–15147. doi:10.1021/acsami.7b02594.

[23] W. Choi, A. Tuteja, J.M. Mabry, R.E. Cohen, G.H. McKinley, A modified Cassie-Baxter relationship to explain contact angle hysteresis and anisotropy on non-wetting textured surfaces, J. Colloid Interface Sci. 339 (2009) 208–216. doi:10.1016/j.jcis.2009.07.027.

[24] P.B. Weisensee, E.J. Torrealba, M. Raleigh, A.M. Jacobi, W.P. King, Hydrophobic and oleophobic re-entrant steel microstructures fabricated using micro electrical discharge machining, J. Micromechanics Microengineering. 24 (2014) 95020. doi:10.1088/0960-1317/24/9/095020.

[25] M.A. Frysali, S.H. Anastasiadis, Temperature-and/or pH-responsive surfaces with controllable wettability: From parahydrophobicity to superhydrophilicity, (2017). doi:10.1021/acs.langmuir.7b02098.

[26] H.Y. ;l. &i. ;r&i. ;. Erbil, Transformation of a Simple Plastic into a Superhydrophobic Surface, Science (80-.). 299 (2003) 1377–1380. doi:10.1126/science.1078365.

[27] Y. Liu, Y. Bai, J. Jin, L. Tian, Z. Han, L. Ren, Facile fabrication of biomimetic superhydrophobic surface with anti-frosting on stainless steel substrate, Appl. Surf. Sci. 355 (2015) 1238–1244. doi:10.1016/j.apsusc.2015.08.027.

[28] N. Vourdas, A. Tserepi, E. Gogolides, Nanotextured super-hydrophobic transparent poly(methyl methacrylate) surfaces using high-density plasma processing, Nanotechnology. 18 (2007) 125304. doi:10.1088/0957-4484/18/12/125304.

[29] R. Hönes, V. Kondrashov, J. Rühe, Molting Materials: Restoring Superhydrophobicity after Severe Damage via Snakeskin-like Shedding, Langmuir. 33 (2017) 4833–4839. doi:10.1021/acs.langmuir.7b00814.

[30] D.P. Linklater, S. Juodkazis, S. Rubanov, E.P. Ivanova, Comment on “ Bactericidal E ff ects of Natural

Nanotopography of Dragon fl y Wing on Escherichia coli ," (2017). doi:10.1021/acsami.7b05707.

[31] R. Hensel, A. Finn, R. Helbig, H.G. Braun, C. Neinhuis, W.J. Fischer, C. Werner, Biologically Inspired Omniphobic Surfaces by Reverse Imprint Lithography, Adv. Mater. (2013) 2029–2033. doi:10.1002/adma.201305408.

[32] Q.F. Xu, J.N. Wang, I.H. Smith, K.D. Sanderson, Superhydrophobic and transparent coatings based on removable polymeric spheres, J. Mater. Chem. 19 (2009) 655. doi:10.1039/b812659c.

[33] X. Zhang, W. Zhu, G. He, P. Zhang, Z. Zhang, I.P. Parkin, Flexible and mechanically robust superhydrophobic silicone surfaces with stable Cassie–Baxter state, J. Mater. Chem. A. 4 (2016) 14180–14186. doi:10.1039/C6TA06493K.

[34] B. Chen, J. Qiu, E. Sakai, N. Kanazawa, R. Liang, H. Feng, Robust and Superhydrophobic Surface Modification by a "paint + Adhesive" Method: Applications in Self-Cleaning after Oil Contamination and Oil-Water Separation, ACS Appl. Mater. Interfaces. 8 (2016) 17659–17667. doi:10.1021/acsami.6b04108.

[35] J. Wu, J. Li, B. Deng, H. Jiang, Z. Wang, M. Yu, L. Li, C. Xing, Y. Li, Self-healing of the superhydrophobicity by ironing for the abrasion durable superhydrophobic cotton fabrics., Sci. Rep. 3 (2013) 2951. doi:10.1038/srep02951.

[36] Y. Liu, Z. Liu, Y. Liu, H. Hu, Y. Li, P. Yan, B. Yu, F. Zhou, One-step modification of fabrics with bioinspired polydopamine@octadecylamine nanocapsules for robust and healable self-cleaning performance, Small. 11 (2015) 426–431. doi:10.1002/smll.201402383.

[37] R. Bhattacharyya, H.W. Division, B. Atomic, Novus International Journal of Technological Applications of Superhydrophobic Coatings : Needs and Challenges, 2 (2014) 1–9.

[38] P.N. Manoudis, A. Tsakalof, I. Karapanagiotis, I. Zuburtikudis, C. Panayiotou, Fabrication of super-hydrophobic surfaces for enhanced stone protection, Surf. Coatings Technol. 203 (2009) 1322–1328. doi:10.1016/j.surfcoat.2008.10.041.

[39] L. Cao, A.K. Jones, V.K. Sikka, J. Wu, D. Gao, Anti-Icing Superhydrophobic Coatings, Langmuir. 25 (2009) 12444–12448. doi:10.1021/la902882b.

[40] F. Hizal, N. Rungraeng, J. Lee, S. Jun, H.J. Busscher, H.C. Van Der Mei, C.H. Choi, Nanoengineered Superhydrophobic Surfaces of Aluminum with Extremely Low Bacterial Adhesivity, ACS Appl. Mater. Interfaces. 9 (2017) 12118–12129. doi:10.1021/acsami.7b01322.

[41] B.J. Privett, J. Youn, S.A. Hong, J. Lee, J. Han, J.H. Shin, M.H. Schoenfisch, Antibacterial fluorinated silica colloid superhydrophobic surfaces, Langmuir. 27 (2011) 9597–9601. doi:10.1021/la201801e.

[42] L.D. Chambers, K.R. Stokes, F.C. Walsh, R.J.K. Wood, Modern approaches to marine antifouling coatings, Surf. Coatings Technol. 201 (2006) 3642–3652. doi:10.1016/j.surfcoat.2006.08.129.

[43] A. Tropmann, L. Tanguy, P. Koltay, R. Zengerle, L. Riegger, Completely Superhydrophobic PDMS Surfaces for Microfluidics, Langmuir. 28 (2012) 8292–8295. doi:10.1021/la301283m.

[44] R. Truesdell, A. Mammoli, P. Vorobieff, F. Van Swol, C.J. Brinker, Drag reduction on a patterned superhydrophobic surface, Phys. Rev. Lett. 97 (2006) 1–4. doi:10.1103/PhysRevLett.97.044504.

[45] C.C. Tuan, N.P. James, Z. Lin, Y. Chen, Y. Liu, K.S. Moon, Z. Li, C.P. Wong, Self-Patterning of Silica/Epoxy Nanocomposite Underfill by Tailored Hydrophilic-Superhydrophobic Surfaces for 3D Integrated Circuit (IC) Stacking, ACS Appl. Mater. Interfaces. 9 (2017) 8437–8442. doi:10.1021/acsami.6b15771.

[46] K. Ji, J. Zhang, J. Chen, G. Meng, Y. Ding, Z. Dai, Centrifugation-Assisted Fog-Collecting Abilities of

Metal-Foam Structures with Different Surface Wettabilities, ACS Appl. Mater. Interfaces. 8 (2016) 10005–10013. doi:10.1021/acsami.5b11586.

[47] P.G. De Gennes, Soft matter, Rev. Mod. Phys. 64 (1992) 645–648. doi:10.1103/RevModPhys.64.645.

[48] S. Jiang, Q. Chen, M. Tripathy, E. Luijten, K.S. Schweizer, S. Granick, Janus particle synthesis and assembly, Adv. Mater. 22 (2010) 1060–1071. doi:10.1002/adma.200904094.

[49] D.S. Moon, J.K. Lee, Tunable synthesis of hierarchical mesoporous silica nanoparticles with radial wrinkle structure, Langmuir. 28 (2012) 12341–12347. doi:10.1021/la302145j.

[50] S. Jiang, S. Granick, Controlling the geometry (Janus balance) of amphiphilic colloidal particles, Langmuir. 24 (2008) 2438–2445. doi:10.1021/la703274a.

[51] L. Hong, S. Jiang, S. Granick, Simple Method to Produce Janus Colloidal Particles in Large Quantity, Langmuir. 22 (2006) 9495–9499. doi:10.1021/la062716z.

2. THEORETICAL BACKGROUND

2.1 INTRODUCTION

Synthetic procedure for Janus wrinkled silica-gel particles (JWSP) is a multi-step process. The whole project can be considered multi-disciplinary. Indeed, from the beginning (synthesis of wrinkled particles) until the end (application of the JWSPs onto the substrate) different technologies and chemical fields are involved.

In this chapter, different theoretical backgrounds related to the steps of the project are discussed (sol-gel chemistry and Pickering emulsion), together with the theoretical background of superhydrophobic surfaces.

2.2 SUPERHYDROPHOBICITY – THEORETICAL BACKGROUND

In this Section, first, surface wettability and related parameters (contact angle, hysteresis etc.) are defined.

How liquids can interact with surfaces is explained through models (Young, Wenzel and Cassie-Baxter) describing the type of surface wetting, underlining the correlation between liquids parameters and surface properties.

2.2.1 MODELS AND PARAMETERS DEFINING SURFACE WETTABILITY

Surface wettability is an interface related property that depends on the liquid and the type of interface. There are different equations and models that describe the behaviour of liquids on surfaces. In accordance with the surfaces structure types (smooth, rough, hierarchical) we can experiment different liquids behaviours.

Young equation

The most used parameter defining surface wettability is the contact angle (CA). Young first defined this parameter in the followed equation [1]:

$$\gamma_{lg}\, cos\theta + \gamma_{sl} = \gamma_{sg} \qquad (2.1)$$

Where γ_{lg} , γ_{sl} and γ_{sg} are the liquid-gas, solid-liquid and solid-gas interfacial tensions respectively. θ is the angle between the solid-liquid and liquid-gas interfaces, the so-called contact angle (figure 2.1).

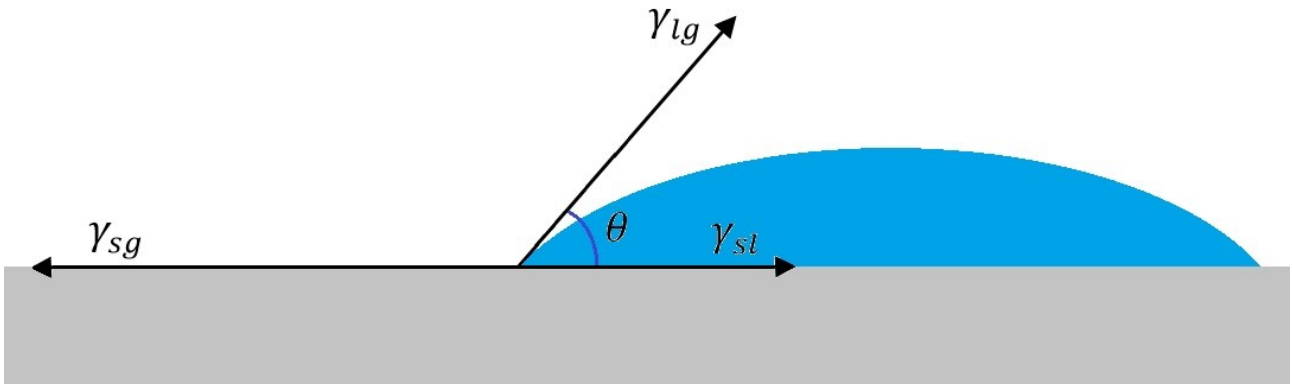

Fig. 2.1. Droplet of liquid on a surface with highlighted surface tension vectors and contact angle.

If water or an apolar solvent exhibit a CA lower than 90° the surface is hydrophilic or oleophilic respectively. Instead, if CA is higher than 90°, the surface possesses a hydrophobic or oleophobic behaviour.

Young equation (equation 2.1) is valid for flat surfaces. Indeed, deviation from the ideal behaviour is higher the rougher the surface. In the case of non-flat surfaces, Wenzel and Cassie-Baxter models are used to correlate morphological properties and the surface tensions involved with the angle formed between the droplets of liquid with the solid surface, called in this case

apparent contact angle (ACA) to distinguish from the ideal CA, that is the angle calculated from Young equation (equation 2.1).

Wenzel model

Wenzel model [2] or "fully wetted" model (figure 2.2), takes in account the roughness of a solid surface. Wenzel considers that liquids touch the solid surface covering all the asperities. Therefore, the liquid-solid contact area (actual interface) is higher than the ideal case in where the surface is smooth (geometric interface) enhancing the wetting properties. The model is described in the equation 2.2.

$$cos\theta^* = r\, cos\theta \qquad (2.2)$$

θ^* is the ACA. r is the roughness factor defined as the actual and geometric interface ratio.

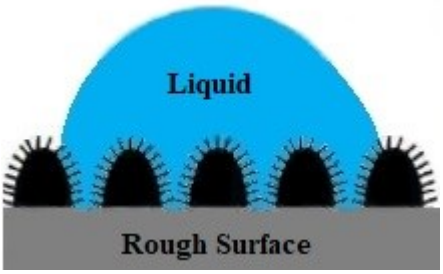

Fig. 2.2. Liquid on rough surface realizing "fully wetted" state.

The equation shows the enhancing effect of the roughness factor. Indeed, two surfaces made of the same material but one smooth and the other rough, the liquid exhibit different contact angles. If the liquid on the smooth surface exhibits a CA less than 90°, the liquid on the rough one will have an ACA value less than CA value. Instead, If the liquid on the smooth surface exhibits a CA more than 90°, the liquid on the rough one will have an ACA value higher than CA value. Therefore, in the case liquid is water, if the surface is hydrophilic or hydrophobic, the rough surface will be more hydrophilic or more hydrophobic than the smooth surface respectively.

Cassie-Baxter model

Cassie-Baxter model or fakir model, considers the liquid not touching completely the solid underneath. The liquid lay on a composite interface made of liquid-gas and solid-gas interfaces (figure 2.3). Therefore, the ACA value depends on the liquid-gas and liquid-solid interfaces extents, each part contributes to the final value. The Cassie-Baxter equation:

$$cos\theta^* = r_\phi \phi_s \, cos\theta + (1 - \phi_s) cos\theta_g \qquad (2.3)$$

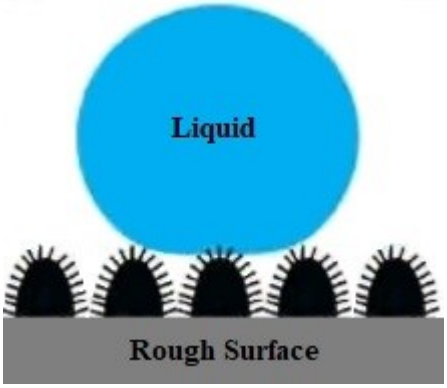

Fig. 2.3. Liquid, on a surface realizing "Fakir" state, lay on a composite interface made of liquid-gas and liquid-solid interfaces.

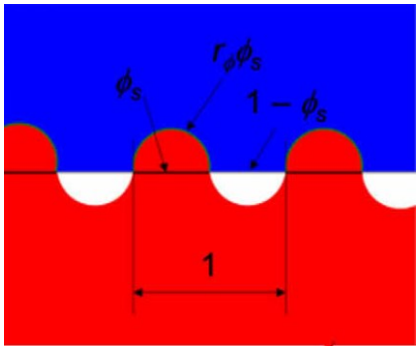

Figure 2.3. Schematic representation of the Cassie-Baxter equation parameters.

Where the r_ϕ is the roughness factor of the wetted surface and ϕ_s is the fraction of geometric interface occupied by solid protrusions. For the reason, $1 - \phi_s$ represents the fraction of

geometric interface constituted by the liquid-gas interface, and $r_\phi \phi_s$ is the wetted surface area. These parameters are illustrated in figure 2.4. θ and θ_g are the ideal CA of the solid-liquid and gas-liquid interfaces respectively, the latter value is 180° [3].

2.2.2 THE HYSTERESIS OF CONTACT ANGLE

If liquids exhibit high apparent contact angle and a low energy of adhesion droplets can roll-off from the surfaces very easily without sticking on them.

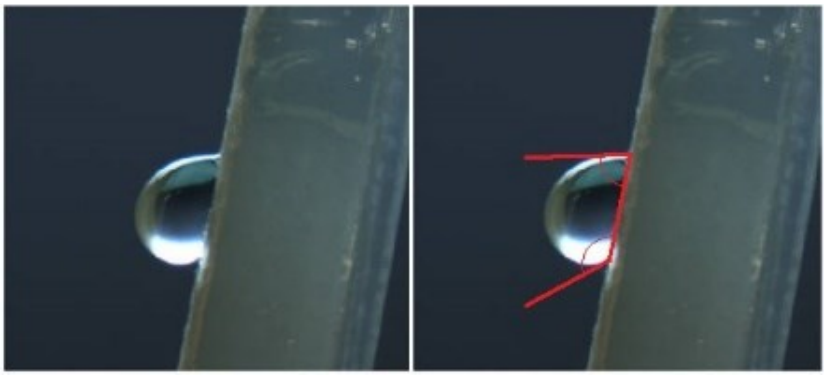

Fig. 2.4. Picture of a droplet moving onto an inclined surface (left) and the same picture showing the advancing and receding contact angles in red (right).

A droplet on a horizontal surface has a characteristic shape that depends on the contact angle. If the surface is tilted slowly, we can observe a change in the droplet shape until the droplet start to roll or slide onto the surface. During the tilting of the droplet the shape change from a sphere to a complex shape with different contact angles around the entire perimeter of the droplet [4]. When the droplet starts to move, the maximum contact angle value is on the downhill side and it is called advancing, while the minimum on the uphill side of the droplet perimeter is called receding contact angle (figure 2.4). The difference of these two angles is called hysteresis of the contact angle $\Delta\theta$ (CAH).

The energy of adhesion is usually related (equation 2.4) [5] to the receding and advancing contact angles:

$$E = \gamma_{lg} \, (\cos \theta_R - \cos \theta_A) \qquad (2.4)$$

θ_R and θ_A are the receding and advancing contact angles respectively, that droplets during rolling or sliding form with surfaces. An experimental parameter linked to the adhesion energy is the hysteresis of the contact angle $\Delta\theta$ (CAH) that is the difference between the advancing and the receding angles (figure 2.4).

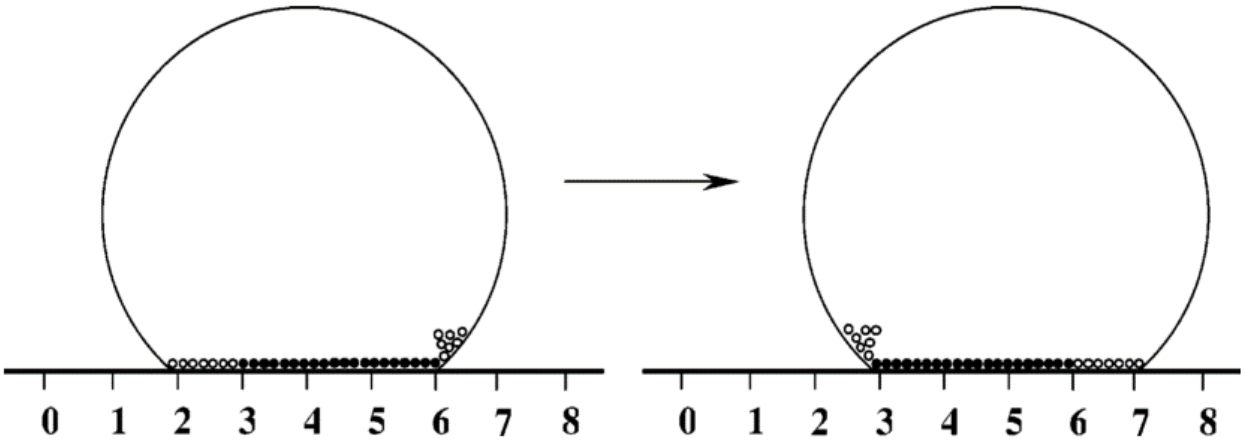

Fig. 2.5. 2-D representation of the droplet movement. The open circles represent the molecules that move during the process, instead, the shaded circles do not move.

In 1945, Pease was the first to suggest that hysteresis is a one-dimension issue, or rather, affected only by the droplet perimeter, the liquid-solid-gas contact line [6]. His work was taken into consideration by very few researchers compared with Wenzel and Cassie-Baxter models . Recently, different research groups [7–9] have commented on the importance of events that occur at the contact line during advancing and receding. Indeed, during the motion of the droplet, the only interfacial molecules of liquid that move are those on the three-phase contact line (the droplet perimeter). In figure 2.5 is reported a 2-D representation of this event: a droplet,

moving on a horizontal surface from one to another equivalent contact area, advances from 6 to 7 and recedes from 2 to 3. The shaded circles in Figure 2.5 between 3 and 6 represent interfacial water molecules that do not move as the droplet does. Consistent with the no-slip boundary condition of fluid mechanics, the only interfacial water molecules that move during this movement (open circles in figure 2.5) are those that wet new surfaces and dewet previously wet surfaces [4].

The above hypothesis was confirmed by different experiments. For instance, Choi et al demonstrated that a droplet of liquid moving onto an anisotropic textured surface has different values of advancing and receding contact angle depending on the direction of movement of the droplet, even though the parameters r_ϕ and ϕ_s (equation 2.3) remain unchanged. This behaviour can be explained through the hypothesis that the droplet during its movement onto the surface forms a contact line that depends on the direction of the droplet [3]. In figure 2.6 is reported an image the anisotropic textured surface with the side views of droplets along the two axis.

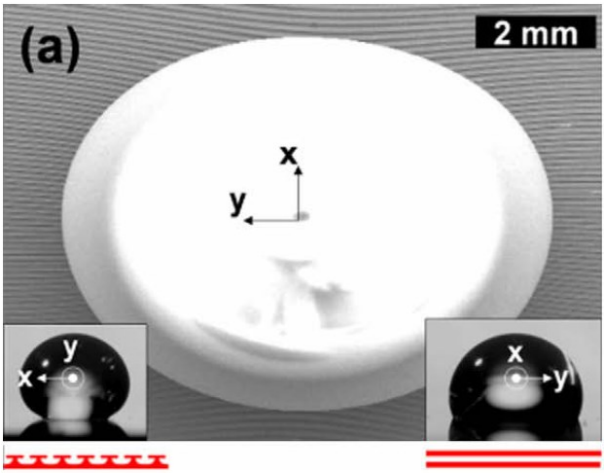

Fig. 2.6. top view of a drop on a texture surface. Charge accumulation on the large drop from the electron beam results in the local lensing and distortion of the hoodoo stripes surface at the top of the image. In the insets, side view of droplets along the two axis.

In conclusion, we can say CAH is a parameter that depends on the contact line between the three phases (solid, liquid and gas). Therefore, the models describing the CA (subsection 2.2.1) cannot estimate the CAH value. Recently a modified Cassie-Baxter relation was proposed that more accurately predicts the apparent advancing and receding contact angles, based on the details of the local surface texture in the proximity of the contact line between the three phases (solid, liquid and gas) [3]. This takes into account the model for the movement of a droplet emerging from the above reported discussion [4]. Events that occur at any point on the contact line can contribute to hysteresis. No events occur over the area between the liquid and the solid away from the contact line. It is assumed that on surfaces with non-uniform roughness, the solid-liquid interface fraction ($r_\phi \phi_s$) and the liquid-gas interface fraction (1-ϕ_s) of Cassie Baxter equation represent the local area fractions of the solid–liquid interface and the liquid–air interface, respectively, in the vicinity of the three-phase (solid–liquid–air) contact line [3,10].The lower solid-liquid area fraction f_{SL} leads to a lower contact angle hysteresis (CAH). Consequently, the Cassie-Baxter state is preferred in designing superomniphobic surfaces with high apparent contact angles (θ^*) and low contact angle hysteresis [10]. Hierarchically structured surfaces that can support a contacting liquid droplet in the Cassie-Baxter state display even lower contact angle hysteresis compared with surfaces with a single scale of texture [10]. Hierarchical textured surfaces, i.e. surfaces with more than one length scale of texture, consisting of a finer length scale texture on an underlying coarser length scale of texture surfaces, are typical structure nature has been using to achieve superhydrophobic properties [11–16]. The reason for such a choice can be understood in the view of the above models.

In conclusion contact angle hysteresis is related [10] to energy barriers that a liquid droplet must overcome during its movement along a solid surface and thus characterizes the resistance to the droplet movement. Lower solid–liquid contact area leads to lesser contact line pinning (that is, lower resistance to droplet movement) and consequently lower contact angle hysteresis. Typically, hierarchically structured surfaces have significantly lower solid–liquid contact area

compared with surfaces that possess a single scale of texture. This results in significantly lower contact angle hysteresis

2.2.3 CASSIE-WENZEL TRANSITION

Superhydrophobicity can be achieved only if liquids stay on the surface in the fakir state (figure 2.3), in which the droplet lay on the protrusions of solid, leaving underneath a gas cushion that permits to the liquids to roll off from the surface without wetting it. Unfortunately, fakir state is metastable and the fully-wetted state is stable, because of the gas-liquid interface characterized by higher interfacial energy than the solid-liquid interfacial energy. For such a reason, the system would like to substitute gas-liquid interface area with solid-liquid one, then, the liquid penetrates into the roughness fully wetting the solid, and the so-called Cassie-Baxter transition occurs [17]. Once the transition happens the droplet is pinned irreversibly to the surface.

A possible strategy to avoid the Cassie-Baxter transition is to increase the energy barrier between these states (fakir and fully-wetted) by increasing the liquid-gas interface area ($1 - \phi_s$) in the equation 2.4), and reducing the ideal contact angle (θ in the equation 2.1 and 2.3) by reducing the solid-gas surface tension γ_{sg} (equation 2.1). Nevertheless, reducing the surface tension has some limitations, indeed the lowest surface tension solids are the fluorinated materials [18] so we cannot use materials with a lower surface tension than the fluorinated ones. Instead, theoretically, there is no limit for the expansion of the liquid-gas interface. Experimentally and confirmed by nature, the best way to increase the liquid-gas interface and reducing the solid-liquid contact area is to have at the surface a hierarchical structure [11–16] (i.e. surfaces with more than one length scale of texture, consisting of a finer length scale texture on an underlying coarser length scale of texture surfaces)

2.2.4 CONCLUSION

According to the type of surface we can estimate the CA value by using three different models: Young, Wenzel and Cassie-Baxter. The wettability properties depend on the CA and particularly on the CAH. Indeed the CAH value is linked to the energy of the adhesion of the liquid in contact with the surface. Low CAH values permit a high slippery behaviour, and together with a high contact angle value (>150°) the surface can be considered superhydrophobic or superoleophobic. Liquid manifesting low CAH and high CA values can roll off from the surface without pinning phenomena. Typically, surfaces with such behaviour are characterized by low surface tension solid-gas and an hierarchical texture.

2.3 SILICA-GEL PARTICLES – THEORETICAL BACKGROUNG

Stöber in the 1968, discovered a process that from organosilane compounds (called precursors) can form silica-gel particles from tens of nanometers until microns, in alcoholic solution with acid or base catalysts at mild condition. The method, which from molecules bring to the formation of a gel matrix, is called sol-gel process.

During the decades, sol-gel chemistry is spread for realizing different kind of materials. Indeed, mesoporous (pores from 2 until 50 nm) silica-gel particles was discovered by combining sol-gel chemistry and the surfactants and polymer self-assembly properties.

In this chapter is discussed , first, sol-gel chemistry related to the Stöber method, then mesoporous silica-gel particles process used in this work.

2.3.1 STOBER METHOD

Organosilanes, molecules possessing a silicon atom, linked to one or more groups that are organic, can react with water forming hydroxylated species according to the reaction:

$$SiX_4 + n\,H_2O \rightarrow SiX_{4-n}(OH)_n + n\,HX \qquad (2.5)$$

X is an organic group, for instance $-OCH_3$ $-OCH_2CH_3$ or other alcohoxide groups, that can be involved in hydrolysis reaction. The reaction is faster if the steric hindrance of the alcohoxide groups is smaller. Once the silanes react with water, the hydroxylated products can react in a condensation reaction (equation 2.6) that brings to the formation of dimers, and for further condensation, oligomers that turn in chains or particles in dependence to the reaction condition. The condensation reaction is stated here:

$$2 \equiv Si(OH) \; -> \; \equiv Si\ O\ Si \equiv \; + H_2O \qquad (2.6)$$

During the proceeding of the siloxanes condensation a gel of silica is formed.

Stöber was the first that found a way to control the formation of monodisperse silica-gel particles by using sol-gel method [19]. The reaction involves an organosilane, usually tetraethoxysilane (TEOS), reacting with water in an ethanol solution. Ammonia is used as catalyser that speeds up the hydrolysis and condensation reactions and for increasing the pH. Indeed, according to "aggregation" Bogush mechanism [20], at high pH, siloxanes monomers react forming small clusters few nanometers in diameter (that Bogush calls "nuclei"). Nuclei continuously form during aggregation process. The new nuclei aggregate preferentially with the particles already formed, making their size to increase, until nanometer nuclei are present in the reaction mixture. Such preference of the small nuclei to aggregate with the bigger particles, explains the monodispersity of sol-gel particles obtained by Stöber method.

With a series of experimental results Bogush et al developed a tool to predict the average diameter of particles by using experimental equations that correlate the concentration of the species within the reaction mixture [21].

$$d = A\,[H_2O]^2 exp(-B[H_2O]^{\frac{1}{2}}) \qquad (2.7)$$

$$A = \; [TEOS]^{\frac{1}{2}}\,(82 + 51[NH_3] + 1200[NH_3]^2 - 366[NH_3]^3)$$

$$B = 1.05 + 0.523[NH_3] - 0.128[NH_3]^2$$

Where d is the average diameter in nanometers and the species in brackets are given in mol/L. The equation 2.7 takes in account the correction made by Razink et al [22]. In fact, in the Bogush paper the equation of the A parameter contains a typographical error, causing the presence of a minus sign before $51[NH_3]$.

The equation 2.7 is valid at 25°C and for a concentration range of 0.1-0.5 for TEOS, 0.5-17.0 M for water and 0.5-3.0 M for ammonia. Outside these ranges, the monodispersity is not guaranteed and/or the average diameter cannot be estimated with high accuracy.

2.3.2 WRINKLED SILICA-GEL PARTICLES

Since Mobil oil company synthesised the first mesoporous silica particles, several researchers have focused on the synthesis of new type of porous particles [23–31] and on the application. Indeed, for the very large surface area per volume, mesoporous silica particles are used for many purposes and in many fields: solar cells [23], biological nanocarrier [32], drug delivery [33–35], catalysis [29,36],

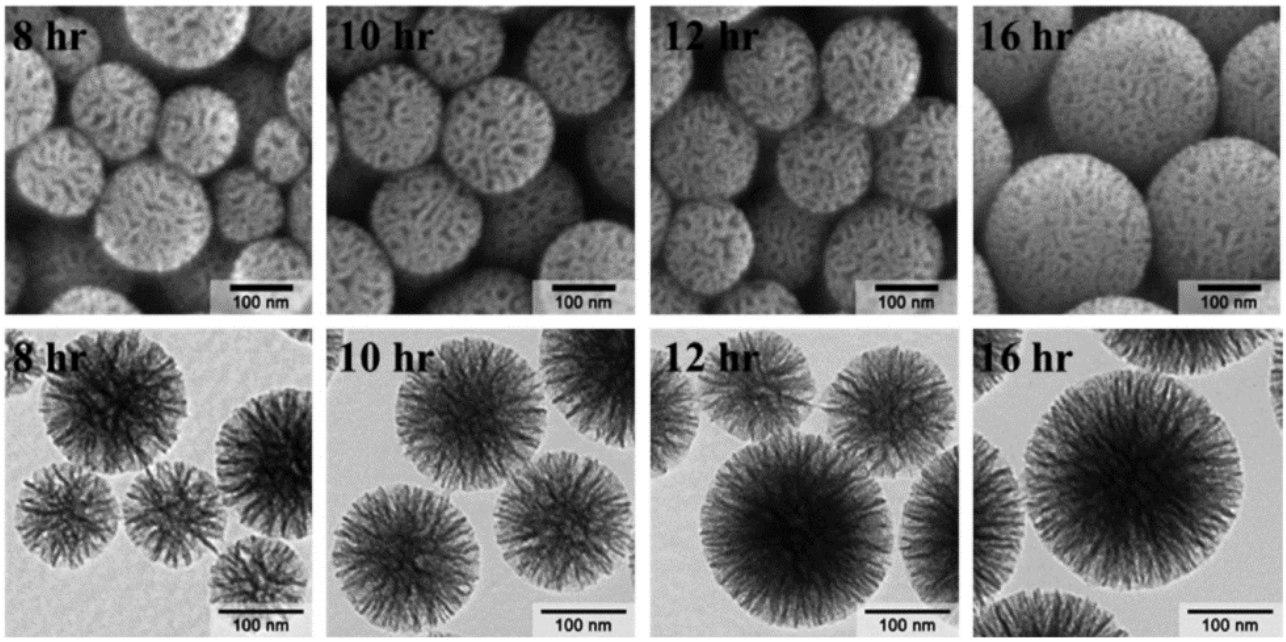

Fig. 2.8. SEM and TEM micrographs of the wrinkled particles following Moon et al procedure at different reaction time.

Recently, spherical silica with nanometer size and radial interconnected wrinkle structure have been synthesised (figure 2.8). The pores structure enhances the accessibility of functional materials and molecules, making the particles an optimum candidate as support materials for drug delivery and catalysis.

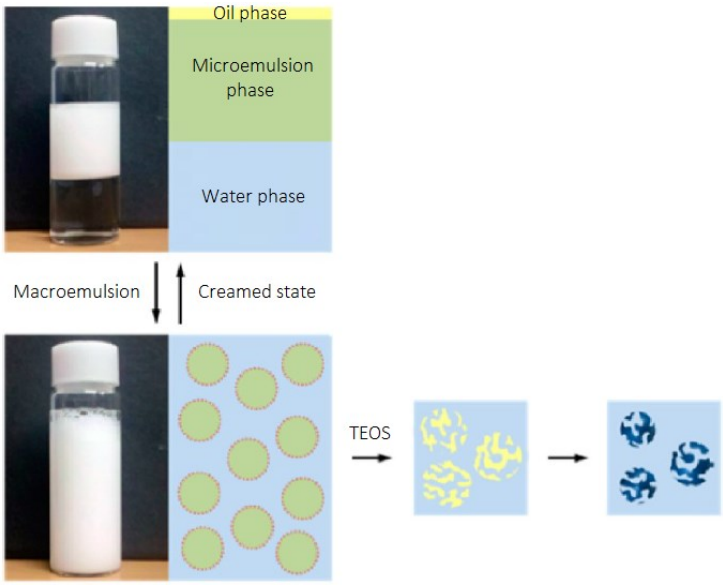

Fig. 2.9. Schematic representation of the Winsor III system (upper picture) and macroemulsion with formation of wrinkled silica-gel particles (lower picture), with related samples.

Formation of wrinkled structure is possible by combining sol-gel chemistry with the behaviour of the emulsion phases. Moon and Lee [37] demonstrated that wrinkle structure is produced in a bicontinuous microemulsion phase dispersed in water as macroemulsion. In their procedure, cyclohexane representing the oil phase, water, Cetylpiridinium bromide (CPB) and isopropyl alcohol with the role of stabilizers and urea as catalyst were mixed together. So as illustrated in figure 2.9, the ratio between the components permits the formation of the so called Winsor III system [38] characterized by a microemulsion phase in equilibrium with oil and water phases. Under stirring the microemulsion breaks up in small droplets forming a macroemulsion, in

where water is the dispersant. At this stage, TEOS is added into the system, and goes into the oil phase because of its hydrophobic behaviour. Water, thanks to the effect of urea, gradually hydrolyses TEOS according to the reaction 2.5. The pH of the water phase is higher then 7, this means all the hydrolysed products (silicate monomers) are negatively charged, therefore, they electrostatically interact with the positively charged surfactants (CPB) that cover the oil-water interface stabilizing microemulsion phase. At the interface the silicates react according to the reaction 2.6 forming the sol-gel skeleton of the particles.

2.3.3 SUPERHYDROPHOBIC SURFACE BASED ON SILICA PARTICLES

After the discussion regards the common processes involving formation of superhydrophobic and superolephobic surfaces shown in the subsection 1.2.3, in this subsection, we focus the attention on silica particles as patterning agent to build up superhydrophobic surfaces.

As we know from the section 1.2, the way particles are applied onto substrate is important for realizing hierarchical structures achieving superhydrophobicity.

If the substrate already possess micrometric roughness (such as fabric, sponge and foam) applying hydrophobic silica particles reduce the surface tensions of the interface and adds a roughness at nanometre level that guarantees the formation of the hierarchical structure. For instance, Salehabadi et al decorated sponges with hydrophobic fumed silica particles realizing superhydrophobic sponges [39]. Khan et al deposited silica particles onto papers and polyurethane foam [40]. Guo et al synthetized silica-gel particles on PET fabric in situ and then they rendered the fabric superomniphobic and superhydrophobic by surface reaction with perfluorodecyltrichlorosilane and dodecyltrimethoxysilane respectively [41].

For flat substrate, the procedure for applying silica particles is crucial, since the material added onto the substrate need to form hierarchical structure. For instance, a way to improve the roughness is using a mixture of different silica particles with different average diameter in order to avoid particles close-packing on the surface. Song et al used a mixture of three different silica

particles with average diameter of 5 μm, 600 nm and 200 nm applied on the substrate by spin-coating. Zhi et al formed a superhydrophobic surface building two layer of particles: the first possess bigger particles made of 50-100 μm in diameter and the upper layer contains particles of 7-40 nm in diameter [42]. Zhang et al used a mixture of Polyvinylpyrrolidone and aggregates of 1 μm of particles of 50 nm in diameter [43]. Bravo et al built up a surface applying polyamine and a mixture of 50 – 20 nm in diameter silica particles using layer by layer technique [44]. Wang used 50-150 nm fluorinated silica particles on fabrics, paper and glass realizing in all cases superhydrophobic surfaces [45].

Then, raspberry, mesoporous particles and aggregates of smaller particles can build up hierarchical structure once applied on the surface thanks to their nano roughness. Sun et al formed superhydrophobic surfaces by deposition of clusters (100 μm in diameter) of silica particles (450 nm) on glass [46]. Anitha et al synthetized mesoporous silica particles from rice husk and after silane treatment enhanced the wetting nature of the particles resulted in superhydrophobicity [47]. Bai et al synthesised hollow mesoporous silica particles and used loaded with dodecyltrimethoxysilane. Superhydrophobic surfaces were fabricated by spray coating of the loaded particles that stack structure and polydimethylsiloxane (PDMS) as hydrophobic interconnection [48]. Yildirim et al prepared superhydrophobic coatings by spin-coating of sol containing hydrophobic particles and mesoporous fluorinated particles [49]. Pereira et al realized superomniphobic surfaces by in situ incorporation of fluorinated mesoporous silica nanoparticles of ~45 nm [50].

An other way for hierarchical structure formation is using spray-coating technique of mixtures of polymers and particles. Hejazi et al spray-coated a surface with a mixture of polyurethane tetrahydrofuran and ethanol with hydrophobic silica particles. During the solvent evaporation, the polyurethane formed a rough layer decorated of hydrophobic particles[51].

Brassard et al studied the effect of varying diameter of fluorinated silica particles applied on flat substrate by spin-coating. They used particles from 40 up to 300 nm and found that

superhydrophobicity is achieved from ~120 nm on thanks to surface roughness with size up to ~0.7 μm [52].

2.3.4 CONCLUSION

In this paragraph, the chemistry of the sol-gel process, for formation of Stöber particles and Moon and Lee wrinkled silica-gel particles [37], were briefly described. The high porosity of the wrinkled particles explain the choice to use this system for building a hierarchical texture by applying such particles on surfaces. Then, we outlined the possibilities of using silica particles to build up superhydrophobic surfaces.

2.4 PICKERING EMULSION – THEORETICAL BACKGROUND

The past decade has witnessed tremendous progress in diversifying synthetic strategies for the preparation of Janus particles (particles with two sides possessing different physical-chemical properties, so as reminded in subsection 1.3.3) with the aim to include diverse functionalities, as well as finding ways toward a scale-up [53]. In this PhD project, we choose one of this approach: the reaction of particles at an oil in water (O/W) Pickering emulsion of a molten wax. In this Section, the emulsification process is explained by reviewing on the forces involved in the formation of the dispersed droplets in the continuous phase, and the type of emulsion stabilizers.

2.4.1 EMULSION

An emulsion is constituted by a liquid phase dispersed in a non-miscible liquid. The fine dispersion of one phase within the other, usually, is a thermodynamically unfavourable process. Indeed, to fine disperse a phase in the other, the total energy of the system should increase, because of the formation of new interface among the liquids.

$$\Delta G = A\,\gamma \qquad (2.8)$$

In the equation 2.8 is reported the variation of the total free energy of Gibbs ΔG when the system, constituted by two macroscopically separated phases, undergoes to a fine dispersion of one phase into the other. ΔG is directely proportional to the variation of the liquid-liquid interface area A after the mixing and to the liquid-liquid interfacial tension γ. Once the system is mixed, coalescence events bring back the system to the initial state characterized by the minimum energy. Forming a stable emulsion is still possible by adding into the mixture a stabilizer, usually molecules (surfactants or polymers) or colloidal particles that reduce the interfacial energy among the liquids and create a barrier to coalescence.

Along with the stabilizer, the energy input is an important parameter to break up the emulsion in fine droplets.

2.4.2 FORCES INVOLVED IN THE EMULSIFICATION PROCESS

To break apart the droplets in the continuous phase, a force should be applied by mixing systems (ultrasounds, magnetic stirring, rotor-stator systems, etc.). Nevertheless, the forces applied should be higher then the forces that keep the droplets together, otherwise, the droplet will not be disrupted.

Laplace pressure

The pressure inside the droplets is higher than the pressure in the surrounding continuous phase. This pressure difference (inside and outside the droplet) is called Laplace pressure, which depends on the droplet shape and curvature and the interfacial tension (equation 2.9).

$$\Delta P = \frac{2\gamma}{R_d} \qquad (2.9)$$

The above equation is valid for spherical droplets with radius R_d and interfacial tension γ. Therefore the smaller the droplet the higher its internal pressure.

Weber number

The external force, opposing the force that keeps the droplet together, is complex to estimate because of the fluidic dynamic complexity of the phenomenon and the uncertainty of the external flow regime. For this reason, Weber number, a dimensionless parameter is used for quantifying and simplifying the breaking up process.

Weber number is the ratio between the external disruptive forces (shear stress) and the forces that keep the droplets together, that in many situation corresponds only to the Laplace pressure. Instead, for very short time mixing, the viscosity of the dispersed phase needs to be taken into account together with Laplace pressure, because the viscosity causes a slow reaction to the external stress.

The common expression for Weber number, considering spherical droplets and long mixing time is reported in the following equation:

$$We = \frac{\tau R_d}{2\gamma} \qquad (2.10)$$

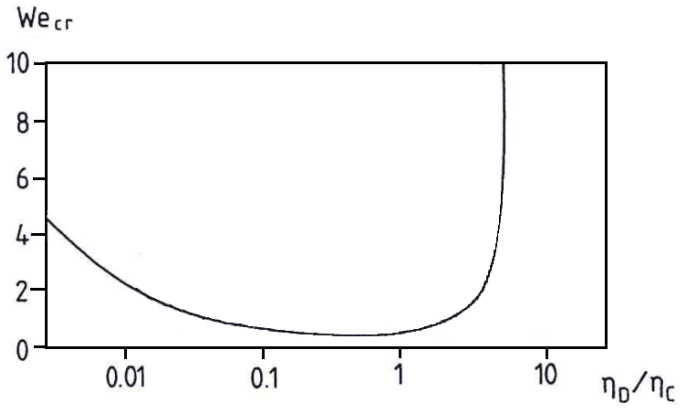

Fig. 2.10. Critical Weber number for laminar flow versus the viscosity ratio of the dispersed and continuous phases [54]**.**

We is the Weber number, τ rappresents the external stress that depends on the type of regime: laminar, turbolent, high tubolent, and R_d is the drop radius. If the Weber number excedes a

critical value, called critical Weber number We_{cr}, the breaking up of the droplets occurs. We_{cr} is usually a number around one, but more precisely, is a function of the viscosity ratio of the dispersed and continuous phases, and the flow regime too. For instance, Grace et al estimated the critical Weber number for laminar flow [54], the graph is reported in figure 2.10.

Disruptive forces

The mixing system imposes a shear flow that exerts a stress on the droplet that cause the breaking apart of the dispersed phase (if the critical Weber number is exceeded). In the case of a laminar flow, the disruptive stress is estimated according the following equation:

$$\tau = \eta\left(\frac{dv}{dz}\right) = \eta\dot{v} \qquad (2.11)$$

Where η is the viscosity of the continous phase and $\dot{v}$ is the shear rate.

In the case of a turbulent flow regime the disruptive stress can be estimated through the Kolmogorov theory (equation 2.12).

$$\tau = \sqrt{\varepsilon\eta} \qquad (2.12)$$

Where ε is the power density (W/m^3) or rather the amount of energy per volume.

When the droplet radius is larger than the value in the equation 2.13,

$$R_d > \frac{\eta^2}{\rho\gamma} \qquad (2.13)$$

turbulent regime becomes very intense, and the shear stress can be estimated with Bernouilli equation:

$$\tau = \sqrt[3]{\varepsilon^2\, R_d^5\, \rho} \qquad (2.14)$$

Where ρ is the density of the continuous phase.

According to the type of flow regime, it is possible to estimate if the parameters are well set to finely break up and disperse one phase into the other. Nevertheless, once the droplets are dispersed in the continuous phase they try to coalesce into larger droplets, the driving force for

the coalescence process is the reduction of the total free energy due to the interface area reduction (see equation 2.8). For stabilizing the droplets and avoiding coalescence the system needs stabilizers.

2.4.3 STABILIZERS

The stabilizers can be amphiphilic molecules, polymers and crystals, and colloidal particles.

Amphiphilic molecules have a side manifesting more affinity with a phase and the other side more affinity for the other phase. They reduce the interfacial tension among the phases and stabilize the emulsion, avoiding the coalescence by steric hindrance and by electrostatic repulsion if the stabilizer contains charged moieties.

Polymers and crystals stabilize the emulsion by forming a network that entraps droplets of the dispersed phase, in this way the droplets cannot encounter each other and coalesce, because of the high viscosity of the continuous phase.

Even colloidal particles could be used as stabilizer, but only if the particles has a partial affinity with both phases. In this case, the particles adsorb onto the interface working as an amphiphilic molecules: one part is within the dispersed phase and the other part stick out into the continuous phase. This type of emulsion, called Pickering emulsion, is characterized for better emulsion stability if compared to classical surfactants as emulsifiers.

2.4.4 PICKERING EMULSION

The high stability given from colloidal particles is due to two main reasons:

1. Particles reduce liquid-liquid interface (characterized by high surface tension).
2. Formation of a shield of particles obstructs the coalescence of the dispersed droplets in the continuous phase.

In this subsection, we evaluate the stability of a Pickering emulsion by a thermodynamic type of experiment. Imaging a system constituted of two phases (phase 1 and 2) and spherical smooth

particles, we calculate the free energy of the system versus the immersion depth of the particle into these two phases [55]. Figure 2.11 can help to visualize the system.

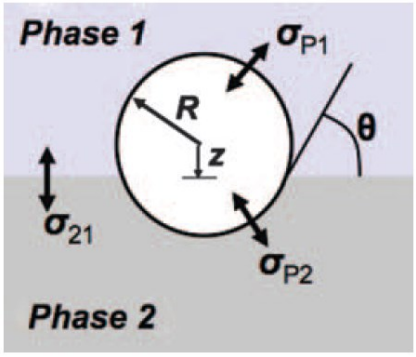

Fig. 2.11. Schematic representation of a spherical smooth particle at two non-miscible liquids interface [56]**.**

In this calculation, all dynamics (kinetics) and external force fields, such as gravitational, electrical, optical and magnetic are ignored. We also do not consider electrostatic (Coulombic) interactions, dielectric effects and van der Waals interactions. We simply consider the energy related to the three type of interfaces within the system. Then each term is multiplied by the corresponding contact area and sum all together, varying the height of the particles z [56].

$$z_0 = \frac{z}{R} \qquad (2.15)$$

z_0 is the ratio between z and the particle radius R.

$$S_P = 4\pi R^2 \; ; A_c = \pi R^2 \qquad (2.16)$$

S_P is the particles surface area and A_c is the area of the circle with radius R.

$$E_{P1} = \sigma_{P1} S_P \frac{(1+z_0)}{2} \qquad (2.17)$$

$$E_{P2} = \sigma_{P2} S_P \frac{(1-z_0)}{2} \qquad (2.18)$$

$$E_{12} = -\sigma_{12} A_c (1 - z_0^2) \qquad (2.19)$$

E_{P1}, E_{P2} and E_{12} are the free energy of the particle-phase 1, particles-phase 2 and phase 1-phase 2 interfaces respectively, and σ_{P1}, σ_{P2} and σ_{12} are the related surface tensions.

When the particle is in both two phases ($-1<z_0<1$), we need to count the interfacial free energy from the particle-phase 1 and particles-phase 2, while the interfaces between phase 1 and phase 2 is occupied by the particle. For the reason, the E_{12} negatively contribute to the total energy of the system E_0 (equation 2.20).

$$E_0 = \frac{E_{P1}+E_{P2}+E_{12}}{k_B T} \qquad (2.20)$$

When the particles is half in the phase 1 and phase 2 $z = 0$.

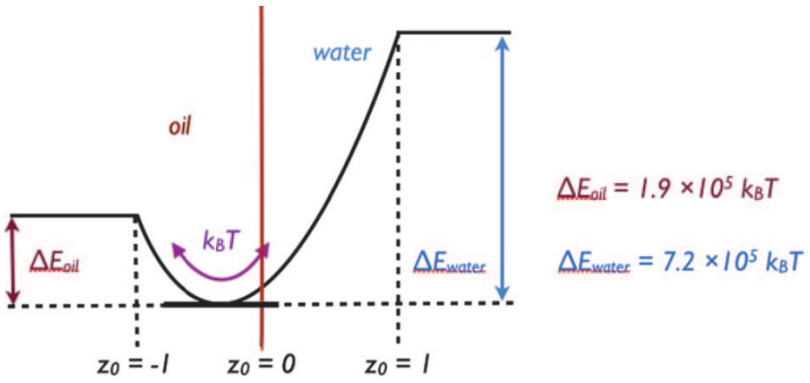

Fig. 2.12. Schematic representation of quadratic energy for a polystyrene spherical smooth particle with radius of 100 nm at water-hexadecane interface [55]**.**

In figure 2.12 shows the energy of polystyrene spherical particle E_0 with radius of 100 nm at a water-hexadecane interface. According to the graph, the equilibrium state (minimum energy) correspond to a position where the particles is partially immersed in both phases ($z_0 \sim 0$).

The energy barrier for particles to escape at the interface drops considerably in the case of rough particles. Ballard and Bon [57] showed this effect experimentally by using Lycopodium spores that were decorated in a mesh of interpenetrating polymer nanoparticles. They theoretically supported the results by showing the energy of four systems: oil-water interfaces stabilized by

smooth polystyrene and polyHEMA particles, buckyball type mesh polystyrene and polyHEMA particles reported in figure 2.13. In the graph is clear that in the case of rough particles there is no high energy barrier for the particles to escape from interface, for the reason, rough particles are weaker stabilizer than smooth particles in Pickering emulsion.

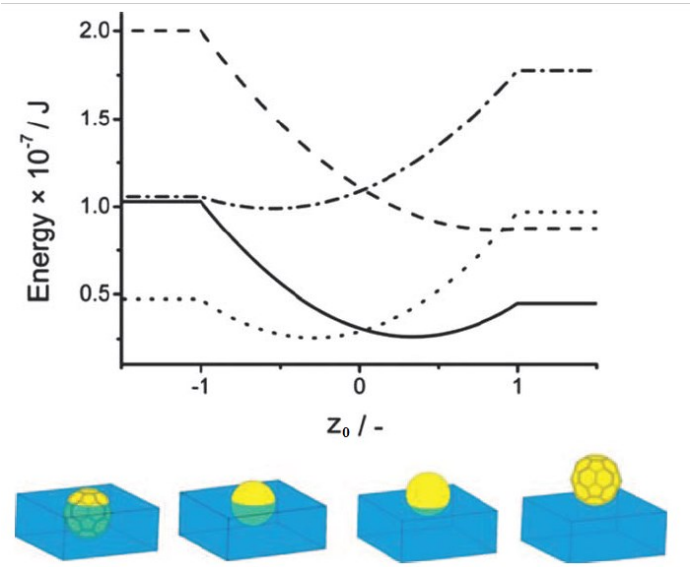

Fig. 2.13. Position of a smooth sphere of polystyrene (——) and of polyHEMA (· · ·) and a buckyball type structure of polystyrene (– – –) and polyHEMA (– · –) at the oil–water interface and illustration of predicted contact angles for (from left to right) a buckyball type structure of polyHEMA, a polyHEMA sphere, a polystyrene sphere and a polystyrene buckyball structure [57]**.**

2.4.5 CONCLUSION

In this Section the disruptive forces and different type of stabilizers, necessary elements for the production of an emulsion are described.

Among the stabilizer agents, the attention was focused on the Pickering emulsion obtained by using colloidal particles. The high stability effect coming from colloidal particles was explained with thermodynamic estimations of the energy barrier that obstructs the removing of particle

from the oil-water interface, drawing a comparison between smooth and rough particles. Such a comparison is important in our project for the interest in the Pickering emulsion preparation by using wrinkled silica-gel particles as stabilizer.

References

[1] T. Young, An Essay on the Cohesion of Fluids, Philos. Trans. R. Soc. London. 95 (1805) 65–87. doi:10.1098/rstl.1805.0005.

[2] R.N. Wenzel, Resistance of Solid Surfaces, Ind. Eng. Chem. 28 (1936) 988–994. doi:10.1021/ie50320a024.

[3] W. Choi, A. Tuteja, J.M. Mabry, R.E. Cohen, G.H. McKinley, A modified Cassie-Baxter relationship to explain contact angle hysteresis and anisotropy on non-wetting textured surfaces, J. Colloid Interface Sci. 339 (2009) 208–216. doi:10.1016/j.jcis.2009.07.027.

[4] L. Gao, T.J. McCarthy, Contact angle hysteresis explained, Langmuir. 22 (2006) 6234–6237. doi:10.1021/la060254j.

[5] R. Di Mundo, F. Palumbo, Comments regarding "an essay on contact angle measurements," Plasma Process. Polym. 8 (2011) 14–18. doi:10.1002/ppap.201000090.

[6] D.C. Pease, The Significance of the Contact Angle in Relation to the Solid Surface, J. Phys. Chem. 49 (1945) 107–110. doi:10.1021/j150440a007.

[7] J.P. Youngblood, T.J. McCarthy, Ultrahydrophobic Polymer Surfaces Prepared by Simultaneous Ablation of Polypropylene and Sputtering of Poly(tetrafluoroethylene) Using Radio Frequency Plasma, Macromolecules. 32 (1999) 6800–6806. doi:10.1021/ma9903456.

[8] W. Chen, A.Y. Fadeev, M.C. Hsieh, D. Öner, J. Youngblood, T.J. McCarthy, Ultrahydrophobic and Ultralyophobic Surfaces: Some Comments and Examples, Langmuir. 15 (1999) 3395–3399. doi:10.1021/la990074s.

[9] C.W. Extrand, Designing for Optimum Liquid Repellency, Langmuir. 22 (2006) 1711–1714. doi:10.1021/la0525401.

[10] A.K. Kota, G. Kwon, A. Tuteja, The design and applications of superomniphobic surfaces, NPG Asia Mater. 6 (2014) e109. doi:10.1038/am.2014.34.

[11] E.P. Ivanova, J. Hasan, H.K. Webb, V.K. Truong, G.S. Watson, J.A. Watson, V.A. Baulin, S. Pogodin, J.Y. Wang, M.J. Tobin, C. Lobbe, R.J. Crawford, Natural bactericidal surfaces: mechanical rupture of Pseudomonas aeruginosa cells by cicada wings., Small. 8 (2012) 2489–2494. doi:10.1002/smll.201200528.

[12] J.W.M. Bush, D.L. Hu, M. Prakash, The Integument of Water-walking Arthropods: Form and Function, 2007. doi:10.1016/S0065-2806(07)34003-4.

[13] D.L. Hu, B. Chan, J.W.M. Bush, The hydrodynamics of water strider locomotion., Nature. 424 (2003) 663–666. doi:10.1038/nature01793.

[14] E. Bormashenko, O. Gendelman, G. Whyman, Superhydrophobicity of Lotus Leaves versus Birds Wings: Different Physical Mechanisms Leading to Similar Phenomena, Langmuir. 28 (2012) 14992–14997. doi:10.1021/la303340x.

[15] R. Helbig, J. Nickerl, C. Neinhuis, C. Werner, Smart skin patterns protect springtails, PLoS One. 6 (2011) e25105. doi:10.1371/journal.pone.0025105.

[16] J. Nickerl, M. Tsurkan, R. Hensel, C. Neinhuis, C. Werner, The multi-layered protective cuticle of Collembola: a chemical analysis, J. R. Soc. Interface. 11 (2014). doi:10.1098/rsif.2014.0619.

[17] T. Koishi, K. Yasuoka, S. Fujikawa, T. Ebisuzaki, X.C. Zeng, Coexistence and transition between Cassie

and Wenzel state on pillared hydrophobic surface., Proc. Natl. Acad. Sci. U. S. A. 106 (2009) 8435–8440. doi:10.1073/pnas.0902027106.

[18] D.W. Grainger, C.W. Stewart, Fluorinated Coatings and Films: Motivation and Significance, in: Fluorinated Surfaces, Coatings, Film., n.d.: pp. 1–14. doi:10.1021/bk-2001-0787.ch001.

[19] W. Stöber, A. Fink, E. Bohn, Controlled growth of monodisperse silica spheres in the micron size range, J. Colloid Interface Sci. 26 (1968) 62–69. doi:10.1016/0021-9797(68)90272-5.

[20] G.H. Bogush, C.F. Zukoski IV, Uniform silica particle precipitation: An aggregative growth model, J. Colloid Interface Sci. 142 (1991) 19–34. doi:10.1016/0021-9797(91)90030-C.

[21] G.H. Bogush, M.A. Tracy, C.F. Zukoski, Preparation of monodisperse silica particles: Control of size and mass fraction, J. Non. Cryst. Solids. 104 (1988) 95–106. doi:https://doi.org/10.1016/0022-3093(88)90187-1.

[22] J.J. Razink, N.E. Schlotter, Correction to "Preparation of monodisperse silica particles: Control of size and mass fraction" by G.H. Bogush, M.A. Tracy and C.F. Zukoski IV, Journal of Non-Crystalline Solids 104 (1988) 95-106, J. Non. Cryst. Solids. 353 (2007) 2932–2933. doi:10.1016/j.jnoncrysol.2007.06.067.

[23] J.S. Kang, J. Lim, W.-Y. Rho, J. Kim, D.-S. Moon, J. Jeong, D. Jung, J.-W. Choi, J.-K. Lee, Y.-E. Sung, Wrinkled silica/titania nanoparticles with tunable interwrinkle distances for efficient utilization of photons in dye-sensitized solar cells, Sci. Rep. 6 (2016). doi:10.1038/srep30829.

[24] W. Pan, J. Ye, G. Ning, Y. Lin, J. Wang, A novel synthesis of micrometer silica hollow sphere, Mater. Res. Bull. 44 (2009) 280–283. doi:10.1016/j.materresbull.2008.06.006.

[25] H. Zhang, Z. Li, P. Xu, R. Wu, Z. Jiao, A facile two step synthesis of novel chrysanthemum-like mesoporous silica nanoparticles for controlled pyrene release, Chem. Commun. 46 (2010) 6783–6785. doi:10.1039/C0CC01673J.

[26] Z. Tao, Mesoporous silica-based nanodevices for biological applications, RSC Adv. 4 (2014) 18961–18980. doi:10.1039/C3RA47166G.

[27] A. Zhang, L. Gu, K. Hou, C. Dai, C. Song, X. Guo, Mesostructure-tunable and size-controllable hierarchical porous silica nanospheres synthesized by aldehyde-modified Stober method, RSC Adv. 5 (2015) 58355–58362. doi:10.1039/C5RA09456A.

[28] R. Das, S. Ghosh, M.K. Naskar, Hierarchical hollow collapsed kippah-shaped silicalite-1 with a controllable bimodal pore system by an emulsion based steam assisted conversion approach, RSC Adv. 6 (2016) 95204–95209. doi:10.1039/C6RA19640C.

[29] F. Gao, R. Jin, D. Zhang, Q. Liang, Q. Ye, G. Liu, Flower-like mesoporous silica: a bifunctionalized catalyst for rhodium-catalyzed asymmetric transfer hydrogenation of aromatic ketones in aqueous medium, Green Chem. 15 (2013) 2208–2214. doi:10.1039/C3GC40547H.

[30] L. Wu, Z. Jiao, M. Wu, T. Song, H. Zhang, Formation of mesoporous silica nanoparticles with tunable pore structure as promising nanoreactor and drug delivery vehicle, RSC Adv. 6 (2016) 13303–13311. doi:10.1039/C5RA27422B.

[31] V. Polshettiwar, D. Cha, X. Zhang, J.M. Basset, High-surface-area silica nanospheres (KCC-1) with a fibrous morphology, Angew. Chemie - Int. Ed. 49 (2010) 9652–9656. doi:10.1002/anie.201003451.

[32] S. Zhao, M. Xu, C. Cao, Q. Yu, Y. Zhou, J. Liu, A redox-responsive strategy using mesoporous silica nanoparticles for co-delivery of siRNA and doxorubicin, J. Mater. Chem. B. 5 (2017) 6908–6919. doi:10.1039/C7TB00613F.

[33] S. Huang, L. Song, Z. Xiao, Y. Hu, M. Peng, J. Li, X. Zheng, B. Wu, C. Yuan, Graphene quantum dot-decorated mesoporous silica nanoparticles for high aspirin loading capacity and its pH-triggered release, Anal. Methods. 8 (2016) 2561–2567. doi:10.1039/C5AY03176A.

[34] W. Zhao, H. Zhang, S. Chang, J. Gu, Y. Li, L. Li, J. Shi, An organosilane route to mesoporous silica nanoparticles with tunable particle and pore sizes and their anticancer drug delivery behavior, RSC Adv. 2 (2012) 5105–5107. doi:10.1039/C2RA20166F.

[35] Q. Gan, J. Zhu, Y. Yuan, H. Liu, J. Qian, Y. Li, C. Liu, A dual-delivery system of pH-responsive chitosan-functionalized mesoporous silica nanoparticles bearing BMP-2 and dexamethasone for enhanced bone regeneration, J. Mater. Chem. B. 3 (2015) 2056–2066. doi:10.1039/C4TB01897D.

[36] V. Polshettiwar, J. Thivolle-Cazat, M. Taoufik, F. Stoffelbach, S. Norsic, J.-M. Basset, "Hydro-metathesis" of Olefins: A Catalytic Reaction Using a Bifunctional Single-Site Tantalum Hydride Catalyst Supported on Fibrous Silica (KCC-1) Nanospheres, Angew. Chemie Int. Ed. 50 (2011) 2747–2751. doi:10.1002/anie.201007254.

[37] D.S. Moon, J.K. Lee, Tunable synthesis of hierarchical mesoporous silica nanoparticles with radial wrinkle structure, Langmuir. 28 (2012) 12341–12347. doi:10.1021/la302145j.

[38] P.A. Winsor, Hydrotropy{,} solubilisation and related emulsification processes, Trans. Faraday Soc. 44 (1948) 376–398. doi:10.1039/TF9484400376.

[39] S. Salehabadi, J. Seyfi, I. Hejazi, S.M. Davachi, A.H. Naeini, M. Khakbaz, Nanosilica-decorated sponges for efficient oil/water separation: role of nanoparticle???s type and concentration, J. Mater. Sci. 52 (2017) 7017–7027. doi:10.1007/s10853-017-0935-7.

[40] S.A. Khan, U. Zulfiqar, S.Z. Hussain, U. Zaheer, I. Hussain, S.W. Husain, T. Subhani, Fabrication of superhydrophobic filter paper and foam for oil???water separation based on silica nanoparticles from sodium silicate, J. Sol-Gel Sci. Technol. 81 (2017) 912–920. doi:10.1007/s10971-016-4250-6.

[41] X.J. Guo, C.H. Xue, S.T. Jia, J.Z. Ma, Mechanically durable superamphiphobic surfaces via synergistic hydrophobization and fluorination, Chem. Eng. J. 320 (2017) 330–341. doi:10.1016/j.cej.2017.03.058.

[42] J. Zhi, L.Z. Zhang, Durable superhydrophobic surfaces made by intensely connecting a bipolar top layer to the substrate with a middle connecting layer, Sci. Rep. 7 (2017) 1–12. doi:10.1038/s41598-017-10030-9.

[43] K. Zhang, X. Yang, N. Zhu, Z.C. Wang, H. Yan, Environmentally benign paints for superhydrophobic coatings, Colloid Polym. Sci. 295 (2017) 709–714. doi:10.1007/s00396-017-4053-5.

[44] J. Bravo, L. Zhai, Z. Wu, R.E. Cohen, M.F. Rubner, Transparent Superhydrophobic Films Based on Silica Nanoparticles Transparent Superhydrophobic Films Based on Silica Nanoparticles, 23 (2007) 7293–7298. doi:10.1021/la070159q.

[45] H. Wang, J. Fang, T. Cheng, J. Ding, L. Qu, L. Dai, X. Wang, T. Lin, One-step coating of fluoro-containing silicananoparticles for universal generation of surface superhydrophobicity, Chem. Commun. (2008) 877–879. doi:10.1039/B714352D.

[46] C. Sun, Z.Z. Gu, H. Xu, Packing the silica colloidal crystal beads: A facile route to superhydrophobic surfaces, Langmuir. 25 (2009) 12439–12443. doi:10.1021/la902785k.

[47] C. Anitha, S.S. Azim, S. Mayavan, Fluorine free superhydrophobic surface textured silica particles and its dynamics–Transition from impalement to impingement, J. Alloys Compd. 711 (2017) 197–204. doi:10.1016/j.jallcom.2017.03.338.

[48] X. Bai, C.H. Xue, S.T. Jia, Surfaces with Sustainable Superhydrophobicity upon Mechanical Abrasion, ACS Appl. Mater. Interfaces. 8 (2016) 28171–28179. doi:10.1021/acsami.6b08672.

[49] A. Yildirim, H. Budunoglu, B. Daglar, H. Deniz, M. Bayindir, One-pot preparation of fluorinated mesoporous silica nanoparticles for liquid marble formation and superhydrophobic surfaces, ACS Appl. Mater. Interfaces. 3 (2011) 1804–1808. doi:10.1021/am200359e.

[50] C. Pereira, C. Alves, A. Monteiro, C. Magén, A.M. Pereira, A. Ibarra, M.R. Ibarra, P.B. Tavares, J.P. Araújo, G. Blanco, J.M. Pintado, A.P. Carvalho, J. Pires, M.F.R. Pereira, C. Freire, Designing novel hybrid materials by one-pot co-condensation: From hydrophobic mesoporous silica nanoparticles to superamphiphobic cotton textiles, ACS Appl. Mater. Interfaces. 3 (2011) 2289–2299. doi:10.1021/am200220x.

[51] I. Hejazi, J. Seyfi, G.M.M. Sadeghi, S.H. Jafari, H.A. Khonakdar, A. Drechsler, S.M. Davachi, Investigating the interrelationship of superhydrophobicity with surface morphology, topography and chemical composition in spray-coated polyurethane/silica nanocomposites, Polym. (United Kingdom). 128 (2017) 108–118. doi:10.1016/j.polymer.2017.09.020.

[52] J.D. Brassard, D.K. Sarkar, J. Perron, Synthesis of monodisperse fluorinated silica nanoparticles and their superhydrophobic thin films, ACS Appl. Mater. Interfaces. 3 (2011) 3583–3588. doi:10.1021/am2007917.

[53] A. Walther, A.H.E. Mu, Janus Particles : Synthesis , Self-Assembly , Physical Properties , and Applications, (2013). doi:10.1021/cr300089t.

[54] H.P. GRACE†, DISPERSION PHENOMENA IN HIGH VISCOSITY IMMISCIBLE FLUID SYSTEMS AND APPLICATION OF STATIC MIXERS AS DISPERSION DEVICES IN SUCH SYSTEMS, Chem. Eng. Commun. 14 (1982) 225–277. doi:10.1080/00986448208911047.

[55] P. Pieranski, Two-dimensional interfacial colloidal crystals, Phys. Rev. Lett. 45 (1980) 569–572. doi:10.1103/PhysRevLett.45.569.

[56] T. Ngai, S. Bon, eds., Particle-Stabilized Emulsions and Colloids, The Royal Society of Chemistry, 2015. doi:10.1039/9781782620143.

[57] N. Ballard, S.A.F. Bon, Hybrid biological spores wrapped in a mesh composed of interpenetrating polymernanoparticles as “patchy” Pickering stabilizers, Polym. Chem. 2 (2011) 823–827. doi:10.1039/C0PY00335B.

3. EXPERIMENTAL PART

3.1 INTRODUCTION

In this chapter the experimental procedure for the Janus wrinkled silica-gel particles (JWSP) is described. First the synthesis of smooth and wrinkled silica-gel particles is described, followed by Pickering emulsion preparation by using liquid wax, water and silica-gel particles as stabilizers. Then surface functionalization of one face to make wrinkled particles hydrophilic-hydrophobic Janus particles and finally, the second surface functionalization for grafting polymer chains (compatible with polypropylene) to JWSPs is described.

3.2 MATERIALS

Acetone (>99.9% purity), aminopropyltriethoxysilane APTES (99% purity), ammonium hydroxide solution (~25 % wt), cetylpiridinium bromide CPB (>97% purity), cetyltrimethylammonium bromide CTAB (>90% purity), chloroform (>99% purity), cyclohexane (99.5% purity), dichlorodimethylsilane DCDMS (>99.5% purity), ethanol (>99.9% purity), hydrochloride acid (37 % wt), iso-propanol (99.5% purity), maleic anhydride-graft-polypropylene PPgMA (Mw ~ 9,100, Mn ~3,900 by GPC, maleic anhydride 8-10 % wt), n-hexane (85%), paraffin wax (53-57 °C melting range) , tetraethoxysilane TEOS (99.999% purity), anhydrous toluene (99,8% purity) were purchased from Sigma-Aldrich and used without further purification. Double distilled water was purchased from Microtech Srl.

3.3 SILICA-GEL PARTICLES

The synthetic procedure of smooth Stöber and wrinkled silica-gel particles is described in this Section (for theoretical details see Section 2.3).

3.3.1 STOBER PARTICLE SYNTHESIS

Stöber silica-gel particles were synthesised by using the experimental equation of Bogush [1] taking into account the correction found by Razink [2]. In order to obtain particles of 300 nm diameter, the concentration of ethanol, water, ammonia and tetraethoxysilane (TEOS) are 18 mol/L, 0.17 mol/L and 1.0 mol/L respectively. After the addition of TEOS, the mixture was stirred for 1 h, then the particles were rinsed and concentrated by centrifugation (at 12000 rpm for 3 min) where the supernatant was replaced by ethanol; finally the mixture was sonicated until the particles were completely dispersed. The same procedure was then repeated three times by replacing the supernatant with water. The final concentration of the silica-gel particles water dispersion, evaluated by weighting the residue of a known amount of dispersion, was 10.88% on the total mass solution basis.

A small amount of dry silica particles were put on a carbon tape on an aluminium stub and sputter-coated with a thin gold-layer for SEM analysis.

DLS measurements were performed for measuring the average diameter of the particles. Samples were prepared by diluting particles dispersions at ∼1mg/mL, for avoiding double scattering phenomenon. Each measurement was repeated at least 3 times.

3.3.2 WRINKLED PARTICLES SYNTHESIS

In this PhD work, Moon and Lee procedure is followed [3].

First, 8.96 g of CPB and 5.38 g of urea were dissolved in 268 mL of water. Subsequently, 268 mL of cyclohexane and 8.24 mL of iso-propanol were added to the solution. With vigorous stirring, 24.0 mL of TEOS was added dropwise to the mixed solution. After stirring for 30 min at room temperature, the reaction mixture was heated up to 70 °C, and this state was maintained

for 16 h. The reaction mixture was centrifuged at 12000 rpm for 6 min, dispersed in acetone by sonication, then centrifuged again and dispersed in acetone:water=2:1 twice. At the end of this step, particles were rinsed in 500 mL of ethanol and 40 mL of hydrochloride acid solution for 24 hours at 70 °C. Subsequently, the procedure was implemented to better clean the particles surface. Dispersion was centrifuged at 12000 rpm for 3 min and sonicated in ethanol, each step for 8 times, to remove small nanoparticles and then, they were rinsed in 500 mL of ethanol and 40 mL of acid chloride solution for 24 hours again at 70 °C to completely remove the surfactant from silica-gel nanoparticles, and washed trice in ethanol. The concentration of the solution is evaluated by weighing the residue of a dispersion aliquot.

A small amount of dry wrinkled particles were put on a carbon tape on an aluminium stub and sputter-coated with a thin gold-layer for SEM analysis.

The particles were analyzed by TEM by immersing and removing carbon grids into diluted particles dispersion in ethanol (∼1mg/mL) and after letting dry the solvent, the grid was introduced into the TEM sample holder.

DLS measurements were performed for measuring the average diameter of the particles. Samples were prepared by diluting particles dispersions at ∼1mg/mL, for avoiding double scattering phenomenon. Each measurement was repeated at least 3 times.

Wrinkled particles coated glass substrate were analyzed by AFM technique. The coated substrate were prepared by applying particles layers on the glass by dip-coating technique.

3.4 PICKERING EMULSION

The procedure for preparing O/W emulsions of liquid paraffin wax and water by using smooth Stöber and wrinkled silica-gel particles is described in this Section.

3.4.1 EMULSION WITH STOBER PARTICLES

The samples were prepared at fixed ratio of wax and water (1:10 g/g); 97.92 mg of silica-gel particles, instead, the optimizable parameters are: CTAB concentration, the type of mixer and the method of wax addition.

First, CTAB and particles solution were prepared by slow addition of a CTAB stock solution (0.192 mmol/L ~cmc/5) into the silica dispersion under magnetic stirring. The concentration of particles in the final solutions and the pH was 3.93 mg/mL and 9.0 respectively.

Zeta potential of the particles in silica-CTAB dispersions were measured to evaluate the CTAB-surface particles interaction at different CTAB concentration and fixed amount of particles (3.93 mg/mL).

The silica-CTAB dispersions (~20 mL) were heated at 75 °C in an oven. The hot mixtures were placed on a heating plate and the mixing was started, when the mixer was turned on, the melted wax was added into the vortex. The mixer apparatus used in this work are high shear disperser (T25 digital ULTRA-TURRAX ®, S 25N-18G dispersing element) and an overhead stirrer (IKA ® RW18 basic). The heating plate was regulated for maintaining the temperature at 75 °C for 2 minutes (zero time corresponds when all the liquid wax was poured). After this time the dispersions were quenched by pouring the emulsion into 100 mL of cold water (~4 °C) for rapidly solidifying the wax and avoiding aggregation phenomenon. The mixtures were filtered and the colloidosomes were rinsed with 200 mL of distilled water.

The supernatants from each preparation were centrifuged (12000 rpm for 4 min) to collect residues and particles. Afterwards, the centrifuged residues were mixed at 5000 rpm for 30 min in white spirit to solubilize wax residues, and then the dispersion in white spirit was centrifuged and dried in the oven at 100°C overnight. The difference between the initial amount of particles and the dried residue gave the yield of the process.

Procedure I

This procedure is the same used for the preparation of colloidosomes by Stöber particles (subsection 3.3.1). Since in this procedure we used CTAB-particles dispersions, the interactions of wrinkled particles with CTAB had to be investigated. CTAB aqueous solution were poured drop by drop into particles dispersion up to reach the desired CTAB concentration (~1mg/mL of particles concentration). Subsequently, Zeta potential measurements of wrinkled particles were collected for the sample as prepared.

Procedure II

The adopted protocol is a modification of the Jiang et al procedure [4–6]. First,~26 g of the ethanol dispersion containing 2.6 g of wrinkled silica-gel particles were centrifuged and dispersed in acetone and then were poured in a beaker with 59 g of paraffin. The acetone was evaporated first under air flow and then under vacuum to remove all the acetone. The paraffin with dry wrinkled silica-gel particles were heated up to 75 °C and then stirred in order to disperse the particles into the melted paraffin. 590 g of water at 75 °C were then added to the system and the mixture was stirred at 1300 rpm for 15 min to produce an emulsion. Subsequently the system was quenched by pouring the mixture into 1.5 L of cool water (around 4 °C) in order to obtain solidified paraffin wax spheres covered by wrinkled micro-particles (colloidosomes). The suspension was then filtered with a Whatman filter, and the deposit washed with water. The colloidosomes were dried under vacuum (1 mmHg) for 2 days.

Procedure III

A CTAB-particles dispersion is prepared by slow addition of a CTAB stock solution (0.9606 mM) into a particles water dispersion, containing 0.1508 g of particles, until the final CTAB concentration is 0.12mM in 40g of water. The dispersion was centrifuged (12000 rpm 3min) and the residue was dried out at 120 °C for 1.5 h.

Dry particles and 16 g of melted paraffin wax was tip-sonicated for 10 minutes, then the mixture was added into 160 g of hot water (75 °C) and the system was emulsified by an high shear mixer (Ultraturrax) at 9000 rpm for 2 min. Later on, the emulsion was quenched by pouring into 200 mL of cold water. The suspension was then filtered with a Whatman filter, and the deposit washed with water. The colloidosomes were dried under vacuum (1 mmHg) for 2 days.

3.4.3 SEM SAMPLE PREPARATION

All the colloidosomes prepared in this project were analysed by SEM. Before scanning, dry colloidosomes powder were put onto aluminum stubs covered by carbon tape and sputter-coated with a thin gold-layer to enhance the imaging quality.

3.5 SURFACE FUNCTIONALIZATION

In this Section, the first face functionalization obtaining the hydrophobic-hydrophilic JWSPs and then the second functionalization for grafting the polymer part onto Janus particles are illustrated.

3.5.1 HYDROPHILIC-HYDROPHOBIC JANUS PARTICLES

Functionalization was performed through vapour deposition following a procedure reported in the literature [4]. The vapour deposition apparatus is shown in figure 3.1.

Dry nitrogen was bubbled through 8.0 g of DCDMS for 30 min that carried the silane vapour through the support containing the colloidosomes (wax particles covered by silica-gel particles). In order to promote homogeneous surface chemical modification, the “reactor chamber” was gently rolled every 5-10 min to move colloidosomes around. The bubble speed was chosen as 2-3 bubbles/s. After exposure to the silane vapour for the needed time,a dry nitrogen flow was passed through the apparatus containing the colloidosomes for 30 min to blow away any residual silane vapour.

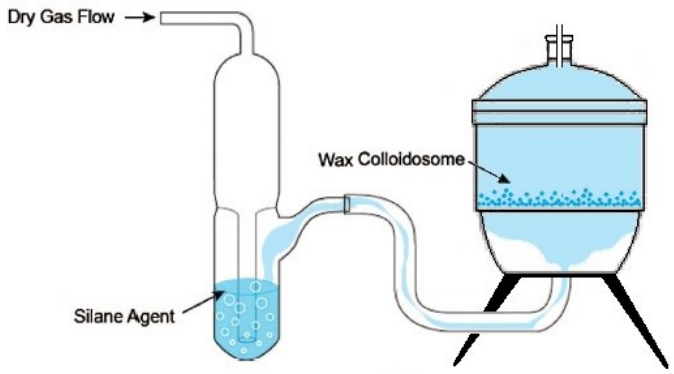

Fig. 3.1 Apparatus for the surface functionalization of wrinkled particles immobilized on the wax colloidosomes.

In order to take the Janus particles out of the colloidosomes, a rinsing in n-hexane was needed. Therefore, the particles were rinsed and centrifuged thrice in n-hexane and thrice in ethanol and then stored in ethanol dispersion.

SEM micrographs were collected to verify the unchanging of the mesoporous structure after the functionalization. A small amount of dry silica particles were put on a carbon tape on an aluminium stub and sputter-coated with a thin gold-layer for SEM analysis.

IR spectra of the functionalized particles were collected. Dry powder samples were located onto the attenuated total reflectance (ATR) accessory, and by means of a metal tip, the sample was compressed on the reflecting crystal to enhance the adhesion and hence increasing the IR adsorption obtaining a spectrum with a good intensity-noise ratio.

DLS measurements were performed for measuring the average diameter of the particles. Samples were prepared by diluting particles dispersions at ~1mg/mL, for avoiding double scattering phenomenon. Each measurement was repeated at least 3 times.

The wettability properties of Janus particles coated substrate were evaluated. The coated substrate was prepared by drop-casting from an ethanol dispersion of particles, then, by a camera, the contact angle of different liquids and the hysteresis of contact angle and roll-off

angle of water droplets were collected. Each parameter was collected at least three times and in different position of the substrate.

Hydrophilic-hydrophobic Janus particles coated glass substrate were analyzed by AFM technique. The coated substrate were prepared by applying particles layers on the glass by dip-coating technique.

3.5.2 POLYMER GRAFTING ON JANUS PARTICLES

Reaction with APTES

The grafting of the polymer part (anhydride-*graft*-polypropylene) can be performed by using a coupling compound: aminopropyltriethoxysilane (APTES) [7] APTES is expected to link to silica particles through condensation reaction of its alcoxy groups with JWSPs surface silanols. Moreover, the reaction may be promoted between the APTES amino groups and PPgMA maleic anhydride side groups, hence the grafting step with APTES is necessary.

A dispersion of JWSPs in ethanol was prepared with a concentration of 5 mg/mL, then APTES was added to the system reaching a concentration 1.13 mmol/L of APTES. The mixture was stirred overnight and then cleaned by centrifugation (12000 rpm 3 min) substitution of the supernatant with ethanol then sonicating and sonication for three times.

Because of the low amount of APTES at the particles surface, XPS turned to be the only technique can detect the presence of nitrogen, atom that belongs to the APTES molecules only. Dry powder sample was mounted on a conducting copper holders and the XPS was recorded on as presented sample.

Reaction with PPgMA

APTES grafted JWSPs dispersion in ethanol is centrifuged to collect the particles, then dried out in the oven at 120 °C for 1.5 h. The particles were dispersed into xylene and sonicated until complete dispersion of the particles residue.

A polymer solution of maleic anhydride-graft-polypropylene (PPgMA) were prepared by mixing PPgMA pellets into xylene at 100 °C under magnetic stirring until complete dissolution (∼10 min). Polymer solution was poured into APTES grafted JWSPs toluene dispersion at 80°C under magnetic stirring. The reaction was carried out for 3 hours. The amount of the species are: 80 mg of APTES grafted JWSPs, 20 mg of PPgMA and 20 mL xylene.

After the reaction, the mixture was centrifuged (12000 rpm 4 min) and the residue was sonicated in xylene. This cleaning step was repeated three times to remove unreacted PPgMA.

PPgMA grafted JWSPs were analyzed by TEM by immersing and removing carbon grids into diluted particles dispersion in xylene (∼1mg/mL) and after letting dry the solvent, the grid was introduced into the TEM sample holder.

IR spectra of the PPgMA grafted JWSPs were collected. Dry powder samples were located onto the attenuated total reflectance (ATR) accessory, and by means of a metal tip, the sample was compressed on the reflecting crystal to enhance the adhesion and hence increasing the IR adsorption obtaining a spectrum with a good intensity-noise ratio.

PPgMA grafted JWSPs xylene dispersion was used to coat polypropylene substrate by dip-coating method. After sample drying, SEM micrographs of the substrate were collected before and after annealing at 160 °C for 1h.

References

[1] G.H. Bogush, M.A. Tracy, C.F. Zukoski, Preparation of monodisperse silica particles: Control of size and mass fraction, J. Non. Cryst. Solids. 104 (1988) 95–106. doi:https://doi.org/10.1016/0022-3093(88)90187-1.

[2] J.J. Razink, N.E. Schlotter, Correction to "Preparation of monodisperse silica particles: Control of size and mass fraction" by G.H. Bogush, M.A. Tracy and C.F. Zukoski IV, Journal of Non-Crystalline Solids 104 (1988) 95-106, J. Non. Cryst. Solids. 353 (2007) 2932–2933. doi:10.1016/j.jnoncrysol.2007.06.067.

[3] D.S. Moon, J.K. Lee, Tunable synthesis of hierarchical mesoporous silica nanoparticles with radial wrinkle structure, Langmuir. 28 (2012) 12341–12347. doi:10.1021/la302145j.

[4] S. Jiang, M.J. Schultz, Q. Chen, J.S. Moore, S. Granick, Solvent-free synthesis of janus colloidal particles, Langmuir. 24 (2008) 10073–10077. doi:10.1021/la800895g.

[5] L. Hong, S. Jiang, S. Granick, Simple Method to Produce Janus Colloidal Particles in Large Quantity, Langmuir. 22 (2006) 9495–9499. doi:10.1021/la062716z.

[6] S. Jiang, S. Granick, Janus balance of amphiphilic colloidal particles., J. Chem. Phys. 127 (2007) 161102. doi:10.1063/1.2803420.

[7] W.-C. Liaw, P.-C. Huang, C.-S. Chen, C.-L. Lo, J.-L. Chang, PPgMA/APTS compound coupling compatabilizer in PP/clay hybrid nanocomposite, J. Appl. Polym. Sci. 109 (2008) 1871–1880. doi:10.1002/app.28294.

4. CHARACTERIZATION TECHNIQUES

4.1 INTRODUCTION

Every Section of this chapter focus on a specific characterization technique used in this PhD project. Therefore, each Section contains: theoretical background and the type of instrument used in this project.

4.2 X-RAY PHOTOELECTRON SPETROSCOPY

In this project, X-ray photoelectron spectroscopy (XPS) technique was used to detect the relative amount of atom species at the surface of Janus particles modified with aminopropyltriethoxysilane. XPS, also known as ESCA (Electron Spectroscopy for Chemical Analysis), is the most widely used surface analysis technique because of its relative simplicity in use and data interpretation.

4.2.1 XPS THEORY

XPS is a technique based on the photoelectric effect, as enunciated by Einstein in 1905. Early experimental observations showed that there is a threshold in frequency below which light, regardless of intensity, fails to eject electrons from a metallic surface. This is a natural consequence of the postulate that light consists of photons of energy E

$$E = h\nu \qquad (4.1)$$

where h is the Planck's constant and ν is the frequency [1]. The energy associated with the threshold frequency ν_c is a measure of the strength of the potential barrier at the surface of the

material that prevents conduction electrons from escaping into empty space. This is called the work function ϕ [2] so that

$$\phi = h\nu_c \qquad (4.2)$$

Typical values of work function are in the range 2 to 6 eV.

At frequencies above ν_c, the excess energy of the photon above ϕ provides photoelectrons with a kinetic energy, whose maximum value is

$$E_{kin}^{max} = h\nu - \phi \qquad (4.3)$$

The maximum kinetic energy is associated with electrons emitted from the Fermi level E_F, i.e. from the highest lying occupied electronic states of the material. Electrons whose energy levels lie below the E_F emerge with correspondingly less kinetic energy:

$$E_{kin} = h\nu - \phi - E_B \qquad (4.4)$$

where E_B is the electron binding energy.

With photon energies in the ultraviolet region of the electromagnetic spectrum only loosely bound valence band electrons can be ionized, but under irradiation with soft X-rays both core and valence levels are accessible. Laboratory based x-ray photoelectron spectroscopy (XPS) experiments are commonly carried out using Al Kα or Mg Kα lines, with photon energies of 1486.6 eV and 1253.6 eV respectively. Core level binding energies are essentially characteristic of an element so that core XPS provides a means of chemical analysis.

XPS sampling depth

Soft X-rays may penetrate several hundreds of nanometres into a solid, so that photoelectrons are generated with a significant flux quite deep into the bulk of the solid. However, the electrons may be inelastically scattered as they propagate toward the surface. The electron mean free path λ is a measure of the mean distance that an electron travels before suffering an inelastic scattering event inside a solid. The photoelectron flux is attenuated from a value I_0 at a distance

d beneath the surface to a value I at the surface according to a Beer Lambert type attenuation law:

$$I = I_0 - e^{-\frac{d}{\lambda}} \qquad (4.5)$$

90% of flux comes from a region within 3λ of the surface. Figure 4.1 shows the electron mean free path λ as a function of kinetic energy for a few selected materials [3]. It can be seen that in the kinetic energy range of interest in XPS measurements (5 eV to 1500 eV) the mean free path of electrons varies from about 5 Å to 15 Å. This means that the peaks in X-ray photoelectron spectra are due to those electrons generated within the first few atomic layers of the material. This gives rise to the characteristic surface sensitivity of XPS when applied to solids.

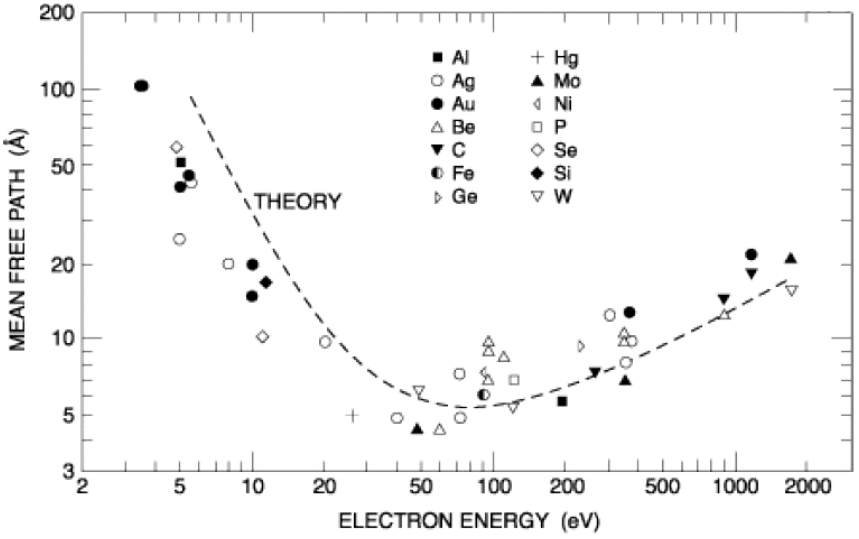

Fig. 4.1. Mean-free paths in different elements as a function of kinetic energy. The general trend is called "universal curve" since the data shows no systematic dependence on the nature of the solid.

Binding energy

A rigorous theory of binding energies makes use of first principle methods to calculate the difference between the total energy of a final state (N-1) and its initial ground state N [3].

However, a simple approach for the estimation of the changes of binding energies of core electrons in ionic solids referring only to macroscopic thermodynamic quantities is based on a Born-Haber cycle and the so-called equivalent core approximation.

Figure 4.2 depicts this method for a crystalline insulator. If an ion of nuclear charge Z is taken out of the solid, its energy changes by the Madelung energy E_M^Z. The resulting free ion is then photoionized, a process that requires the binding energy of the orbital under consideration in the free ion E_B (ion). In the "equivalent core approximation", the photoionized ion is a approximated by a (Z+1)-ion: the equivalent-core approximation model assumes that provided the spatial extension of a core electron is small compared to that of the valence electrons, the photoionization of a core level can be approximated by the hypothetical addition of a proton to the nucleus. The ion is put back into the lattice, gaining the Madelung energy for the (Z+1)-ion. The sum of the energies of the cycle estimates the binding energy measured by XPS for the chosen orbital in the solid. It is the sum of the binding energy of that orbital in the free ion and the Madelung term for unit charge.

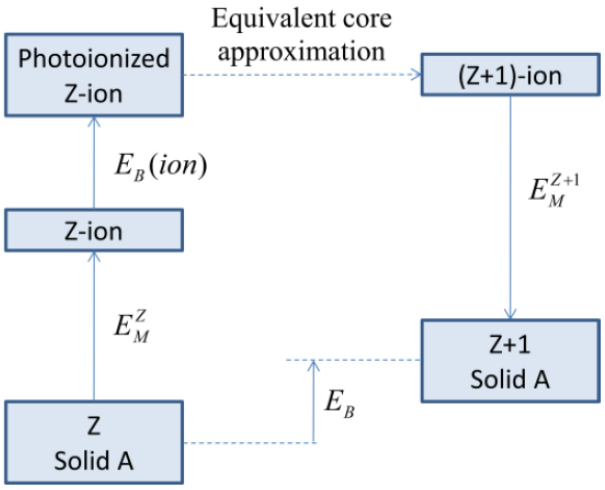

Fig. 4.2. Born-Harber cycle describing photoionization of an insulator, which includes the equivalent core approximation.

4.2.2 XPS INSTRUMENT

XPS were taken with Thermo Scientific K-Alpha spectrometer using a 72 W monochromated Al K alpha source ($h\nu$ = 1486.6 eV). The X-rays are microfocused at the source to give a spot size on the sample of 400 microns in diameter. The analyser is a double focusing 180 degree hemisphere with mean radius 125 mm. It is run in constant analyser energy (CAE) mode. The pass energy was set to 200 eV for survey scans and 50 eV for high resolution regions. All XPS were referenced according to the adventitious C 1s peak (285 eV).

4.3 ATTENUATED TOTAL REFLECTANCE SPECTROSCOPY

Functional group detection was necessary to understand the excellence of functionalization reaction done in this work. We collected IR spectra of the samples by using Attenuated Total Reflectance technique (ATR).

4.3.1 IR SPECTROSCOPY THEORY

Infrared (IR) spectroscopy is a non-destructive technique for gaining structural information and identifying the chemical bonds in unknown compounds. This information is important for qualitative as well as quantitative determination of the chemical compounds used in various scientific areas of research.

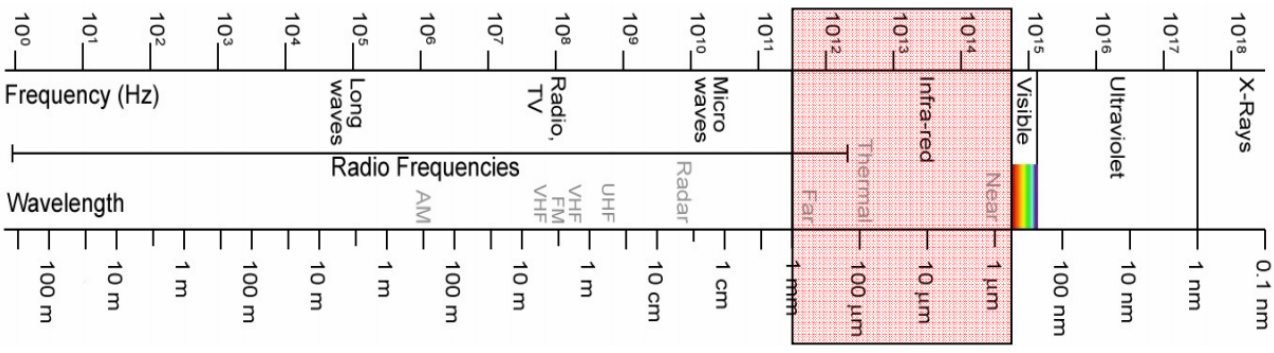

Fig. 4.3. Electromagnetic spectrum with IR zone hightlighted.

The infrared range of the electromagnetic spectrum covers the wavelength region from 25 μm to 1 mm, which conforms to the wavenumber range 40.000-100 cm^{-1} (figure 4.2). It is split in the Near-IR (NIR), the Mid-IR (MIR) and the Far-IR (FIR) region. It is neighbour to the visible region on one side and the microwave region on the other. All regions in the electromagnetic region can be described by energy E and its relationship with frequency ν measured in hertz (Hz), which is the number of waves per second (equation 4.1).

We can convert the frequency ν to wavenumber $\bar{\nu}$, the units employed in IR spectroscopy by equation 4.6 that transforms the equation 4.1 into the equation 4.7.

$$\nu = c\bar{\nu} \qquad (4.6)$$

$$E = hc\bar{\nu} \qquad (4.7)$$

where the wavenumber $\bar{\nu}$ is measured in cm^{-1} and c is the speed of light (3.0x10 cm/s).

IR spectroscopy is a spectroscopy technique based on the energy absorption due to the vibrational transitions of molecules and solids. The chemical bonds within the molecule has different type of vibrations. If the length of the bond changes, the vibration is called stretching, and bending if the bong angles changes.

Usually, molecules at ambient temperature stay in the fundamental vibration state (characterized by the minimum energy of vibration). Adsorption of IR radiation with a frequency belonging within the 2.5-25 μm range (corresponding with the Medium IR with wavenumber between 4000 e 400 cm^{-1}), may induce vibrational transition to an excited state.

The simplest model for describing an harmonic oscillation of a biatomic molecule is the Hooke law. Where the energy levels can be derived from the equation 4.8.

$$E_v = \left(u + \frac{1}{2}\right) h\omega \qquad (4.8)$$

Where u is the quantic vibrational number (0, 1, 2, …), h is the Planck constant and ω is the vibrational frequency given from the following equation:

$$\omega = \frac{1}{2\pi}\sqrt{\frac{k}{\mu}} \quad (4.9)$$

k, strength constant of the chemical bond, μ is the reduced mass of the biatomic system (equation 4.10).

$$\mu = \frac{M_1+M_2}{M_1M_2} \quad (4.10)$$

M_1 and M_2 are the mass of the atoms.

Therefore, the adsorption energy (necessary for the vibrational transition) increases if the strength of the bond increase and if μ, or rather the mass of the biatomic system, decreases.

The general rules that have to be fulfilled, for the molecules to adsorb IR waves, are two: the change in the vibrational states has to cause a variation in the dipole of the molecule and the second is stated in the equation 4.11

$$\Delta v = \pm 1 \quad (4.11)$$

An IR spectrum report the absorbance or the transmittance versus the wavenumber.

Functional groups can be detected, because the vibrational transition of specific functional groups belong to particular region of the spectrum. Moreover many molecules has characteristic signal defined as “finger print” in the region at lower wavenumber. Liquids, solids and gases can be analysed through this technique [4,5].

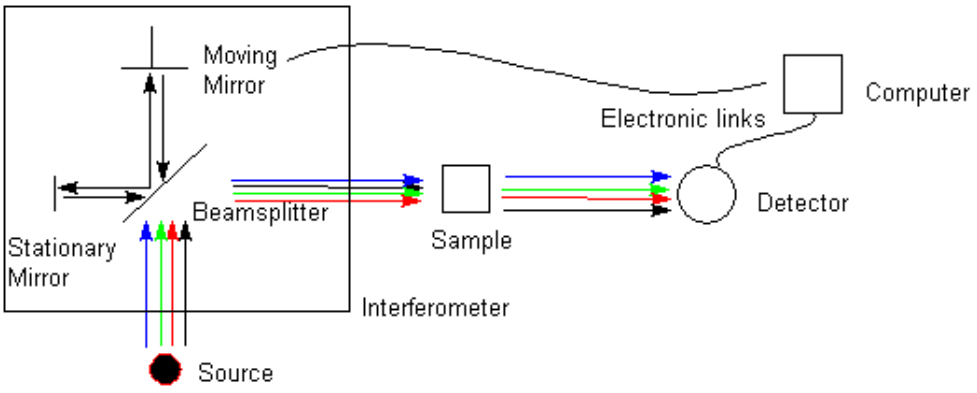

Fig. 4.4. Schematic of a FT-IR spectrophotometer.

An Fourier-transform IR spectrophotometer (figure 4.4) is composed of an interferometer that permits to scan the frequency all at once by using white light emitted from a silicon carbide cylinder. A semi-reflecting mirror (beamsplitter) divides the beam in two parts, one goes on a mirror, the other on a mobile mirror. The motion of the mirror causes a interference between the two reflected beams, when they unify again to go through the sample and arrive to the detector, obtaining the so called interferogram (intensity versus time). Then, the Fourier-transform is applied for converting the interferogram into the IR spectrum.

Transmission and ATR spectroscopy

Since Stimson in 1952 [6] first applied KBr pellets in IR spectroscopy of solid samples transmission spectroscopy has been one of the most used IR techniques. ATR spectroscopy [7] is equally a much employed technique. The theory behind these techniques is quite different, considering that they are based on the same principles. In transmission, the light source goes through the sample (embedded in an inert medium) to the detector. The sample is normally dispersed in KBr for the MIR region and in CsI for the FIR region, as these are inert in the respective regions. The ATR technique is a surface examination technique. An internal reflecting element crystal is used to focus and direct the light beam to the surface of investigation. Usually the beam only penetrates about 1-5 μm into the sample. The beam is absorbed by the sample and is reflected back out to the crystal and the beam continues to the detector (figure 4.5).

Not only the theory behind the techniques are different but also the output spectra look different. There are several distinct features that differentiate ATR spectra from transmission spectra when comparing the two techniques. The ATR spectra looks more distorted than the transmission spectrum, especially changes in intensity are observed and some bands, particularly the very strong bands, appear to shift to a lower frequency. These ATR distortion

are quite known from the MIR [8]. Band shift between the two methods can be anywhere from 1-50 cm^{-1}, where 1- 10 cm^{-1} is normal, and 40-50 cm^{-1} appears only in very extreme cases.

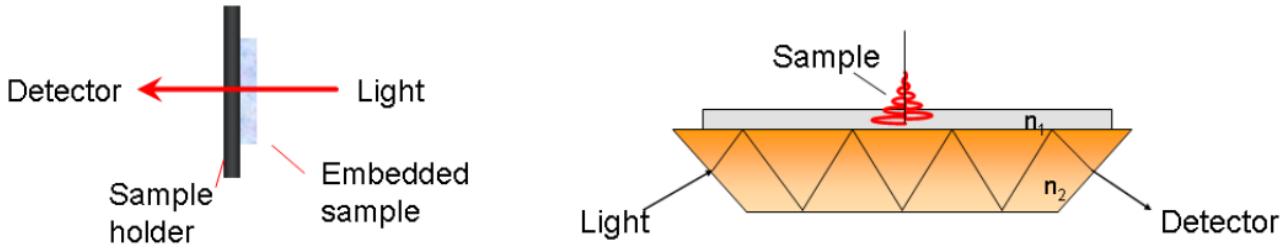

Fig. 4.5. Schematic rappresentation of transmission and ATR techniques. Images from ThermoFisher ©.

4.3.2 ATR INSTRUMENT

In this work, we used a Fourier transform infrared (FT-IR) transmittance spectra were recorded with a Nikolet FT-IR spectrometer (ThermoFisher) using a single reflection attenuated total reflectance (ATR) accessory with a resolution of 4 cm^{-1} and 32 scans.

4.4 ATOMIC FORCE MICROSCOPY

Atomic Force Microscopy (AFM) permitted to obtain topography details of surfaces. In this project AFM was used to analyse substrates coated with wrinkled silica-gel particles and hydrophilic-hydrophobic Janus wrinkled silica-gel particles.

4.4.1 AFM APPARATUS

The AFM consists of a cantilever with a sharp tip (probe) that is used to scan the surface. The cantilever is typically silicon or silicon nitride with a tip radius of curvature on the order of nanometers. When the tip is brought into proximity of a sample surface, forces between the tip and the sample lead to a deflection of the cantilever according to Hooke's law. Depending on the situation, forces that are measured in AFM include mechanical contact force, van der Waals

forces, capillary forces, chemical bonding, electrostatic forces, magnetic forces, solvation forces, etc.

Typically, the deflection is measured using a laser spot reflected from the top surface of the cantilever into an array of photodiodes (see Figure 4.6).

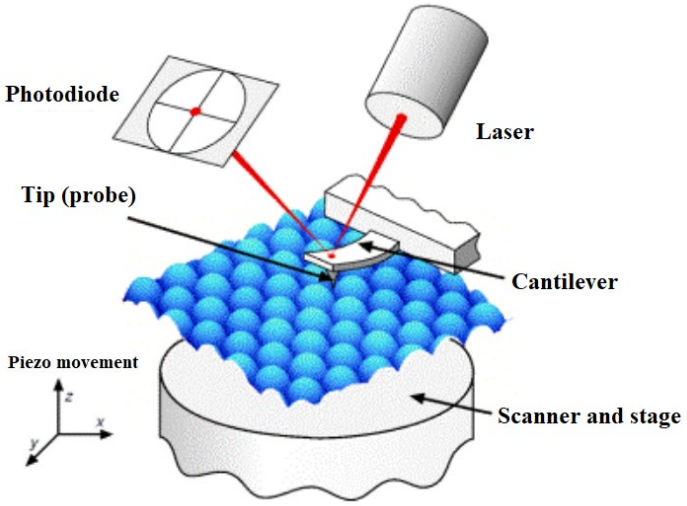

Fig. 4.6. Schematic illustration of an AFM. The tip is attached to a cantilever, and is raster-scanned over a surface. The cantilever deflection due to tip-surface interactions is monitored by a photodiode sensitive to laser light reflected at the tip backside.

Other methods that are used include optical interferometry, capacitive sensing or piezoresistive AFM cantilevers. These cantilevers are fabricated with piezoresistive elements that act as a strain gauge. Using a Wheatstone bridge, strain in the AFM cantilever due to deflection can be measured, but this method is not as sensitive as laser deflection or interferometry. If the tip was scanned at a constant height, a risk would exist that the tip collides with the surface, causing damage. Hence, in most cases a feedback mechanism is employed to adjust the tip-to-sample distance to maintain a constant force between the tip and the sample. Traditionally, the sample is mounted on a piezoelectric tube, that can move the sample in the z direction for maintaining a constant force, and the x and y directions for scanning the sample. Alternatively a 'tripod'

configuration of three piezo crystals may be employed, with each responsible for scanning in the x,y and z directions. In new designs, the tip is mounted on a vertical piezo scanner while the sample is being scanned in x and y using another piezo block. The resulting map of the area z = f (x, y) represents the topography of the sample. The AFM analysis can be operated in a number of modes, depending on the application. In general, possible imaging modes are divided into static (also called contact) modes and a variety of dynamic (non-contact or "tapping") modes where the cantilever is vibrated.

Non-contact mode AFM does not suffer from tip or sample degradation effects that are sometimes observed after taking numerous scans with contact AFM. This makes non-contact AFM preferable to contact AFM for measuring soft samples.

4.4.2 AFM INSTRUMENT

We investigated the topography of the samples by means of an Atomic Force Microscope (AFM – Witec Alpha 300 RAS) working in tapping mode with non-contact cantilevers (resonance frequency of 280 kHz and spring constants of k = 42 N/m). This operation mode is well suited for imaging soft samples since it reduces the tip to sample interaction. Therefore, it avoids the perturbation of particle-to-particle adhesion, which would result in the presence of artefacts in the topographic images.

4.5 DINAMIC LIGHT SCATTERING

Dynamic Light Scattering (DLS) is a scattering technique that was used to estimate the size distribution of wrinkled and Janus particles. In this Section, information about theory, type of instrument used and sample preparations are reported.

4.5.1 DLS THEORY

Dynamic Light Scattering (DLS), also known with the general name of Quasi-Elastic Scattering (QES) is a technique aimed at obtaining dynamical information about the system under investigation [9–11]. If QES measurements are performed using visible light the Brownian diffusion of a dilute particle suspension can be characterized.

QES Principles

In the case of light scattering, the electric component of the incoming wave is responsible for the interaction with the electrons of the sample. In particular, the incoming electric field induces an oscillating dipole moment according to the particle polarizability.

$$\vec{\mu} = \alpha \overrightarrow{E_i} \qquad (4.12)$$

$$E_i(\vec{r}, t) = n_i E_0 \exp i[\overrightarrow{k_i} \cdot \vec{r} - \omega_i t] \qquad (4.13)$$

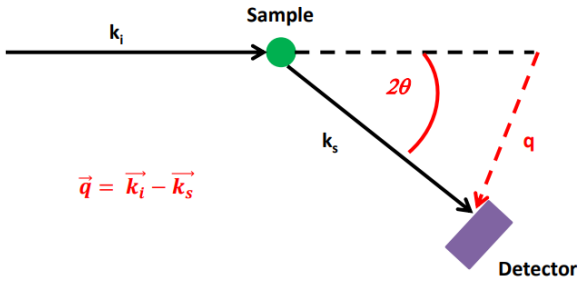

Fig. 4.7. Schematic representation of a scattering experiment leading to the definition of the scattering vector q.

In the general expression of the induced dipole, the polarizability is a tensor, since it depends on the shape and the size of the particle. However, in the special case of spherical particles, a highly symmetric system, the polarizability is a constant. Equation 4.12 also underlines that the induced dipole moment oscillates with the same frequency of the incoming electric field. If no other interaction occurs between the incoming wave and the sample, i.e. absorption, the induced

dipole moment will be the secondary source of the scattered electric field. At distance R from the sample, the expression of the scattered electric field can be derived considering the scheme reported in figure 4.7.

$$E_s(\vec{R},t) = \frac{-k_f^2 E_0}{4\pi R\varepsilon_0} \exp i(k_f \mathrm{R} - \omega_i \mathrm{t}) \delta\varepsilon_{if}(\vec{q},t) \qquad (4.14)$$

In particular, the sample was considered as characterized by a mean dielectric constant ε_0, while $\delta\varepsilon_{if}$ represent the fluctuation of the dielectric constant in the sample, which related to the particle spatial distribution. The dielectric constant fluctuation was already expressed in equation 4.14 as the Fourier transform in q-space of the corresponding function of r (equation 4.15).

$$\delta\varepsilon(\vec{q},t) = \oint \varepsilon(\vec{q},t) e^{i(\vec{q},\vec{r})}\, d\vec{r} \qquad (4.15)$$

A similar expression of the scattered electric field can be obtained in terms of polarizability, which can be easily related to structural properties of the particles.

$$E_s(\vec{R},t) = \frac{-k_f^2 E_0}{4\pi R\varepsilon_0} \exp i(k_f \mathrm{R} - \omega_i \mathrm{t}) \delta\alpha_{if}(\vec{q},t) \qquad (4.16)$$

$$\delta\alpha_{if}(\vec{q},t) = (n_i \cdot n_f)\alpha \sum_{j=1}^{N} e^{iq(r_j(t))} \qquad (4.17)$$

As the dielectric constant, the polarizability varies in space and time (equation 4.17) because of the spatial distribution of the particles and their motions (vibration, rotation and translation).
The scattered intensity arising from a particle suspension, measured at fixed q value, thus at constant incident wavelength and fixed scattering angle, is reported in figure 4.8. Since the scattered intensity depends on the positions particles, which do change with time, the scattered intensity will look like a noise pattern, composed by fluctuations around an average value. The scattered intensity can be converted in the corresponding autocorrelation function to extract information about the particle motion. This is actually a standard approach to treat randomly

fluctuating quantities. Before dealing with the intensity autocorrelation function, the electric field autocorrelation is introduced, recalling equation (4.16).

$$\langle E_S^*(\vec{R},0)E_S(\vec{R},t)\rangle = \frac{-k_f^4|E_0|^2}{16\pi^2R^2\varepsilon_0^2}\langle\delta\alpha_{if}(\vec{q},0)\delta\alpha_{if}(\vec{q},t)\rangle e^{(-i\omega_i t)} \qquad (4.18)$$

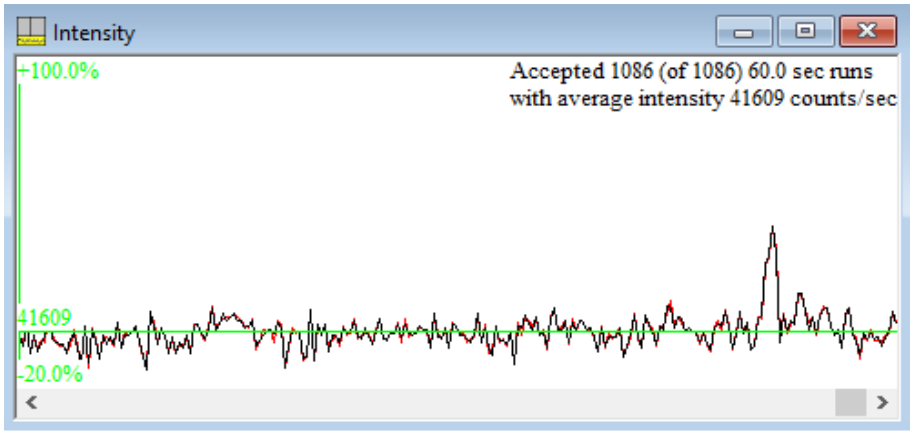

Fig. 4.8. Scattered intensity as function of time. Data shown in the picture refers to a suspension of inorganic nanoparticles.

The autocorrelation function, reported in equation 4.18, gives information about how the scattered electric field changes at time *t* with respect to its initial value at time *0*. The bracket indicates that the product between the two scattered electric field values is averaged over the measurement time, which has to be large with respect to the typical fluctuation time. The electric field autocorrelation function can be converted into the electric field spectral density by means of Fourier transformation.

$$I_E(\omega) = \frac{1}{2\pi}\int_{-\infty}^{+\infty}\langle E^*(0)E(t)\rangle\, e^{i\omega t}dt \qquad (4.19)$$

Fourier transform connect a function of time (the electric field autocorrelation function) with a function of frequency, ω, (the electric field spectral density). The shape of the I_E in the frequency domain is governed by the difference between ω_f and ω_i, respectively the scattered

and incident frequency. Equation 4.20 is obtained by substituting equation 4.18 into equation 4.19.

$$I_E(\vec{q}, \omega_f, R) = \frac{1}{2\pi} \frac{-k_f^4 |E_0|^2}{16\pi^2 R^2 \varepsilon_0^2} \int_{-\infty}^{+\infty} \langle \delta\alpha_{if}(\vec{q}, 0) \delta\alpha_{if}(\vec{q}, t) \rangle e^{(i\omega_f - \omega_i t)}\, dt \qquad (4.20)$$

Where n_i and n_f define the direction of the incoming and the scattered wave.

In the case of an elastic scattering event, ω_f and ω_i are the same, and the spectral density is a line. However, owing to the *Uncertainty Principle*, it is impossible to detect a line spectrum. Indeed, there is always a finite probability for the incoming wave to exchange energy with the sample. All these considerations explain the broadening of the line in the spectral density to give a peak. This peak is also known as elastic peak. Besides the *Uncertainty Principle*, the elastic peak is additionally broadened because of the motions of the scatterers. The techniques that aim to characterization of the broadening of the purely elastic peak are named Quasi-Elastic Scattering (QES) techniques.

Whatever is the probe used for the experiment, the motions of the scatterers within the sample produce fluctuations of the scattered intensity. The temporal correlation function of these fluctuations provides information about the diffusion coefficient of the scatterers.

DLS Principles

In DLS field it is possible to identify two different kind of approach for determining the electric field autocorrelation function, also known as $g^1(t)$. The first one is the filter method, which consists on analyzing the scattered intensity in terms of frequency, and thus measuring the spectral density. As reported in equation 4.20, once the spectral density is measured, the electric field autocorrelation function can be calculated. On the other hand, the optical mixing methods directly measure the autocorrelation functions. Among the optical mixing method, the homodyne and heterodyne methods can be distinguished. The homodyne method, which will be discussed in this section, measures the scattered intensity from the sample and calculates its

autocorrelation function, also known as $g^2(t)$. The heterodyne method combines the intensity scattered from the sample with a fraction of the intensity coming from the laser source. By using this approach, it can be demonstrated that even if more complex instrumental setup and data analysis with respect to the homodyne method are involved, $g^1(t)$ can be directly determined. Typical samples analyzed by means of DLS are dilute suspensions of particles, where the scattered intensity from each particle can be considered independent. Under this condition, $g^2(t)$ is related to $g^1(t)$ according to equation 4.21.

$$g^2(t) = I_S^2(1 + \beta|g^1(t)|^2) \qquad (4.21)$$

Where I_S^2 represent the square of the average intensity scattered by the sample and β is an efficiency factor, related to the instrumental setup. In particular, if the illuminated area is small compared to the coherence area $\beta \sim 1$. Hence, equation C.10 demonstrates that by measuring the scattered intensity autocorrelation function, the scattered electric field autocorrelation function can be calculated. The time fluctuations of the scattered electric field are produced by the polarizability fluctuations, which are related to the motion of the particles. From the evaluation of $g^1(t)$, characteristic parameters of the dynamics of the particles within the suspension can be derived upon identifying a suitable model to describe the particle motion. In the case of Brownian motion, for an ensemble of equal particles, the particle displacement is related to its translational diffusion coefficient (D) by equation 4.22.

$$\Delta r_j = 6D\Delta t \qquad (4.22)$$

If the equation 4.22 is substituted in the expression of the scattered electric field (equation 4.16) and $g^1(t)$ is calculated according to equation 4.18, equation 4.23 is obtained.

$$g^1(t) = e^{-Dq^2t} \qquad (4.23)$$

In particular, the above reported simple expression of $g^1(t)$ takes into account of the electric field autocorrelation function normalization for the incoming intensity. Equation 4.23 holds for

a system composed by particle, showing all the same size and shape. However, in a real sample $g^1(t)$ depends on a the distribution of diffusion coefficients reflecting the sizes and shapes of the particles. In other words, equation 4.23 has to be reformulated in order to take into account of the polydispersity of the system under investigation.

$$g^1(t) = \int G(\Gamma) e^{-\Gamma t} d\Gamma \quad (4.24)$$

Where $\Gamma = Dq^2$ and is the inverse of the characteristic diffusion time of the particles, which also represent the time at which the correlation between the scattered electric field values is lost.

In conclusion, the scattered electric field autocorrelation function can be calculated from DLS measurement of the intensity autocorrelation function. The collected data can be analyzed according to equation 4.24 and the mean diffusion coefficient as well as its distribution function can be estimated. Suitably developed algorithms are available in order to perform data analysis even in the case of complex systems composed by different populations of diffusing particles.

Under the specific condition of spherical non-interacting particles that diffuse in a continuum medium, the Stokes-Einstein relation (equation 4.25) can be used to calculate the hydrodynamic radius (R_h)of the particles from their diffusion coefficient.

$$D = \frac{K_B T}{6\pi\eta R_h} \quad (4.25)$$

Where η is the viscosity of the medium. Thus, DLS can also be used to determine the hydrodynamic radius of the particles in the suspension, which is the effective radius of the particle plus the solvation shells that are diffusing with it.

4.5.2 DLS INSTRUMENT

Size distribution was measured by Zetasizer (Nanoseries, Malvern) using laser dynamic scattering (λ = 632.8 nm) technique.

4.6 SCANNING ELECRON MICROSCOPY

Scanning Electron Microscopy was used for taking 3-D images of the surfaces and particles analysed in this work.

4.6.1 MICROSCOPE STRUCTURE

A scanning electron microscope (SEM) is a type of electron microscope that provides images by scanning over it with a focused beam of electrons. The electrons of the beam interact with electrons of the sample, producing various signals that can be detected and that contain information about the topography and composition of the surface of the sample. The electron beam is generally scanned in a raster scan pattern. The position of the beam is combined with the detected signal to produce an image. Specimens can be observed in high vacuum, low vacuum and in wet condition. The types of signals produced by a SEM include secondary electrons, back-scattered electrons (BSE), characteristic X-rays, light (cathodoluminescence), specimen current and transmitted electrons. Due to the very narrow electron beam, SEM micrographs have a large depth of field yielding a characteristic three-dimensional appearance useful for understanding the surface structure of a sample. A wide range of magnifications is possible, from about 10 times (about equivalent to that of a powerful hand-lens) to more than 500,000 times, about 250 times the magnification limit of the best light microscopes. Back-scattered electrons (BSE) are beam electrons that are reflected from the sample by elastic scattering. BSE are often used in analytical SEM along with the spectra made from the characteristic X-rays, because the intensity of the BSE signal is strongly related to the atomic number (Z) of the specimen. BSE images can provide information about the distribution of different elements in the sample. Characteristic X-rays are emitted when the electron beam removes an inner shell electron from the sample, causing a higher-energy electron to fill the shell and release energy. These characteristic X-rays are used to identify the composition and measure the abundance of elements in the sample. In a typical SEM, an electron beam is

thermionically emitted from an electron gun fitted with a tungsten filament cathode. Tungsten is normally used in thermionic electron guns because it has the highest melting point and lowest vapor pressure of all metals, thereby allowing it to be heated for electron emission, and because of its low cost. Other types of electron emitters include lanthanum hexaboride (LaB_6) cathodes, which can be used in a standard tungsten filament.

The electron beam, which typically has an energy ranging from 0.2 keV to 40 keV, is focused by one or two condenser lenses to a spot about 0.4 nm to 5 nm in diameter. The beam passes through pairs of scanning coils or pairs of deflector plates in the electron column, typically in the final lens, which deflect the beam in the x and y axes so that it scans in a raster fashion over a rectangular area of the sample surface.

When the primary electron beam interacts with the sample, the electrons lose energy by repeated random scattering and absorption within a teardrop-shaped volume of the specimen known as the interaction volume, which extends from less than 100 nm to around 5 μm into the surface. The size of the interaction volume depends on the landing energy of the electron, the atomic number of the specimen and the density of the specimen. The energy exchange between the electron beam and the sample results in the reflection of high-energy electrons by elastic scattering, emission of secondary electrons by inelastic scattering and the emission of electromagnetic radiation, each of which can be detected by specialized detectors. The beam current absorbed by the specimen can also be detected and used to create images of the distribution of specimen current. Electronic amplifiers of various types are used to amplify the signals, which are displayed as variations in brightness on a computer monitor (or, for vintage models, on a cathode ray tube). Each pixel of computer video-memory is synchronized with the position of the beam on the specimen in the microscope, and the resulting image is therefore a distribution map of the intensity of the signal being emitted from the scanned area of the specimen. In older microscopes image may be captured by photography from a high resolution cathode ray tube, but in modern machines image is saved to a computer data storage. All

samples must also be of an appropriate size to fit in the specimen chamber and are generally mounted rigidly on a specimen holder called a specimen stub. For conventional imaging in the SEM, specimens must be electrically conductive, at least at the surface, and electrically grounded to prevent the accumulation of electrostatic charge at the surface.

4.6.2 INSTRUMENT

Scanning electron microscopy (SEM) analysis was performed by means of a FEI Quanta 200 FEG (Eindhoven, The Nederlands) equipped with a secondary electron detector.

4.7 TRANSMISSION ELECTRON MICROSCOPY

Images of particles that permit to differentiate the electric density of the material was collected by means of Transmission Electron Microscopy (TEM) technique. Below the structure of the microscope the type of instrument used and sample preparation are discussed.

4.7.1 MICROSCOPE STRUCTURE

Transmission electron microscopy (TEM) is a microscopy technique in which a beam of electrons is transmitted through a specimen to form an image. The sample is most often an ultrathin section less than 100 nm thick or a suspension on a grid. An image is formed from the interaction of the electrons with the sample. The image is then magnified and focused onto an imaging device, such as a fluorescent screen or a sensor such as a charge-coupled device.

From the top down, the TEM consists of an emission source, made of a tungsten filament or needle, or a lanthanum hexaboride (LaB_6) single crystal source [12]. Gun is connected to a high voltage source (typically ~100–300 kV) and, given sufficient current, the gun will begin to emit electrons into the vacuum. The electron source typically is mounted in a Wehnelt cylinder to provide preliminary focus of the emitted beam. The upper lenses of the TEM then further focus the electron beam to the desired size and location [13]. The lenses of a TEM allow for beam

convergence, giving the TEM the ability to change magnification by modifying the amount of current that flows through the coil, quadrupole or hexapole lenses. The quadrupole lens is an electromagnetic coils at the vertices of the square, enabling the generation of a lensing magnetic fields, the hexapole configuration enhances the lens symmetry by using six, rather than four coils. In figure 4.9 a schematic of the instrument is reported.

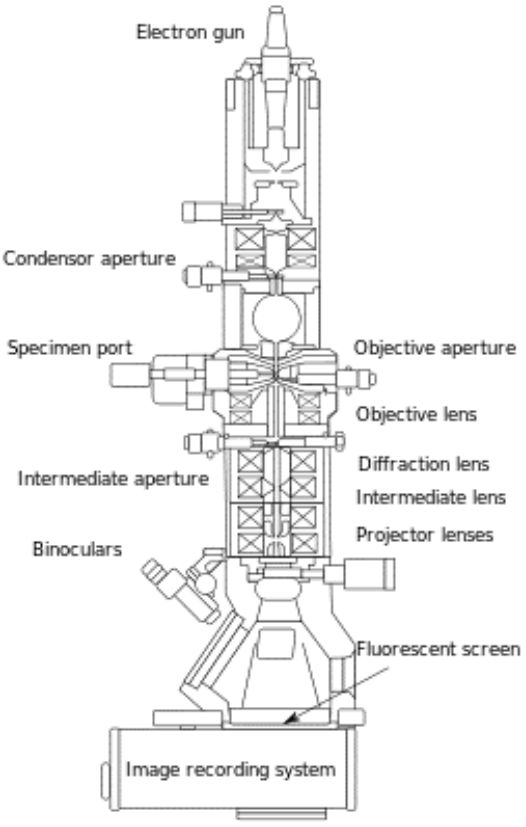

Fig. 4.9. Schematic of a TEM instrument

4.7.2 INSTRUMENT

Bright field transmission electron microscopy (TEM) analysis was performed on a FEI TECNAI G12 Spirit-Twin (LaB_6 source) equipped with a FEI Eagle-4k CCD camera, operating with an acceleration voltage of 120 kV.

4.8 ZETA POTENTIAL MEASURMENTS

Zeta potential was used to evaluate the interaction and stability of particles-surfactant dispersions. Herewith, theory, type of instrument used and samples preparation are reported.

4.8.1 THEORY BEHIND ZETA POTENTIAL

Zeta potential is a scientific term for [14] in dispersions. From a theoretical viewpoint, the zeta potential is the in the interfacial double layer at the location of the. Slipping plane is located in the bulk fluid away from the interface of the colloid. In other words, zeta potential is the potential difference between the dispersion medium and the stationary layer of fluid attached to the (figure 4.10).

The zeta potential is an indicator of the of colloidal dispersions. The magnitude of the zeta potential indicates the degree of electrostatic repulsion between adjacent, similarly charged particles in a dispersion. If the potential is small, attractive forces may exceed this repulsion and the dispersion may flocculate. Therefore, colloids with high zeta potential (negative or positive) are electrically stabilized while colloids with low zeta potentials tend to coagulate or flocculate.

Zeta potential is not measurable directly but it can be calculated using theoretical models and an electrophoretic mobility or dynamic electrophoretic mobility experiments.

Electrophoresis is used for estimating zeta potential of particulates. In practice, the Zeta potential of dispersion is measured by applying an electric field across the dispersion. Particles within the dispersion with a zeta potential will migrate toward the electrode of opposite charge with a velocity proportional to the magnitude of the zeta potential. This velocity is measured using the technique of the laser Doppler anemometer. The frequency shift or phase shift of an incident laser beam caused by these moving particles is measured as the particle mobility, and this mobility is converted to the zeta potential. Electrophoretic mobility is proportional to electrophoretic velocity, which is the measurable parameter. There are several theories that link

electrophoretic mobility with zeta potential. They are described in the article on electrophoresis and in details in books on colloid and interface science [15,16].

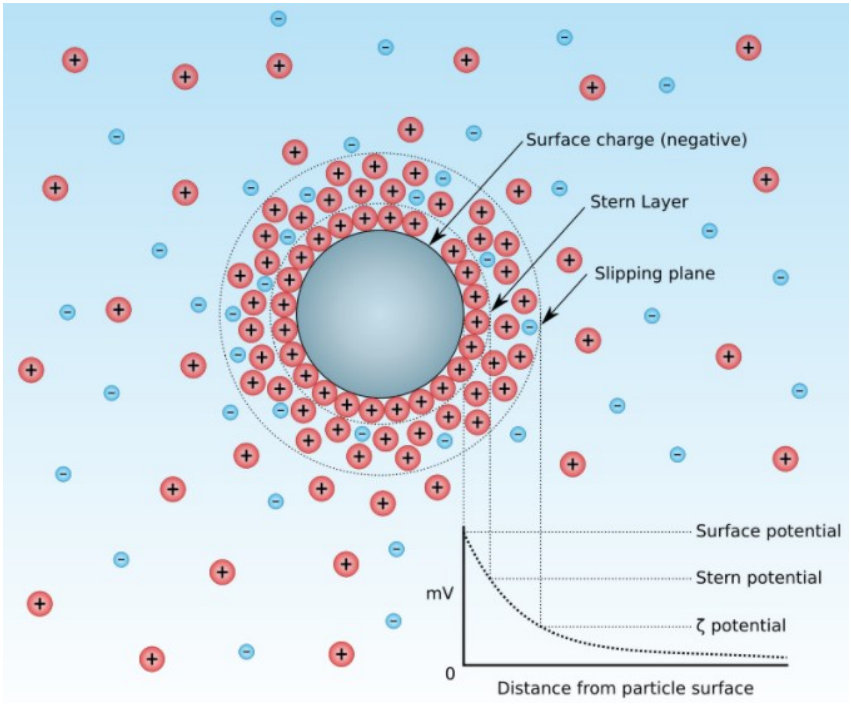

Fig. 4.10. Schematic of a colloidal particle surrounded by Stern and Gouy layers.

There are two different experimental techniques that can measure electrophoretic velocity: microelectrophoresis and electrophoretic light scattering. In this work we use electrophoretic light scattering method. It allows measurement in an open cell or a capillary cell. Moreover, it can be used to characterize very small particles.

4.8.2 ZETA POTENTIAL APPARATUS

The instrument used for the measurement of the Zeta potential was performed by Dynamic Light Scattering (DLS) with a Zetasizer Nano ZS particle size analyzer (Malvern Instruments Ltd).

4.9 WETTABILITY PARAMETERS MEASUREMENTS

The contact angles and roll-off angles of distilled water were measured using a Dataphysics OCA 30 instrument at room temperature (~21 ºC). Apparent contact angles are evaluated through the pictures of droplets on liquids on top of the surface by means of the camera and an image software (the volume of the droplet is ~10µL). Contact Angle hysteresis (CAH) was evaluated by the tilted plane method where a droplet of distilled water is placed on an inclined plane and its contact angles are measured when it starts sliding down [17]. Indeed, when the solid surface is tilted the droplet at first deforms; the contact angle hysteresis was calculated as the difference between the advancing (which is the maximum) and the receding (which is the minimum) contact angles on a tilted solid surface when the droplet begins to roll.

References

[1] R.C. Ropp, Solid State Chemistry, Clarendon Press, 2003. doi:10.1016/B978-0-444-51436-3.X5000-7.

[2] L. Cardona M. Ley, Photoemission in Solids I, Springer Berlin Heidelberg, San Diego, CA, 1978. doi:10.1007/3-540-08685-4.

[3] S. Hüfner, Photoelectron Spectroscopy: principles and aplications, Springer (2003)

[4] M.G. McKee, G.L. Wilkes, R.H. Colby, T.E. Long, Correlations of Solution Rheology with Electrospun Fiber Formation of Linear and Branched Polyesters, Macromolecules. 37 (2004) 1760–1767. doi:10.1021/ma035689h.

[5] A.R. West, Solid State Chemistry And Its Applications, Springer, 2014.

[6] M.M. Stimson, M.J. O'Donnell, The Infrared and Ultraviolet Absorption Spectra of Cytosine and Isocytosine in the Solid State1,2, J. Am. Chem. Soc. 74 (1952) 1805–1808. doi:10.1021/ja01127a054.

[7] L.A. Averett, P.R. Griffiths, K. Nishikida, Effective Path Length in Attenuated Total Reflection Spectroscopy, Anal. Chem. 80 (2008) 3045–3049. doi:10.1021/ac7025892.

[8] N.J. Harrick, F.K. du Pré, Effective Thickness of Bulk Materials and of Thin Films for Internal Reflection Spectroscopy, Appl. Opt. 5 (1966) 1739–1743. doi:10.1364/AO.5.001739.

[9] A. Lomakin, D.B. Teplow, G.B. Benedek, Quasielastic light scattering for protein assembly studies., Methods Mol. Biol. 299 (2005) 153–174.

[10] M. Wadsäter, J.B. Simonsen, T. Lauridsen, E.G. Tveten, P. Naur, T. Bjørnholm, H. Wacklin, K. Mortensen, L. Arleth, R. Feidenhans'l, M. Cárdenas, Aligning Nanodiscs at the Air–Water Interface, a Neutron Reflectivity Study, Langmuir. 27 (2011) 15065–15073. doi:10.1021/la203100n.

[11] C. Stubenrauch, P.-A. Albouy, R. v. Klitzing, D. Langevin, Polymer/Surfactant Complexes at the Water/Air Interface: A Surface Tension and X-ray Reflectivity Study, Langmuir. 16 (2000) 3206–3213. doi:10.1021/la991277j.

[12] R.F. Egerton, Physical Principles of Electron Microscopy, Springer US, 2005.

[13] H.H. Rose, Optics of high-performance electron microscopes, Sci. Technol. Adv. Mater. 9 (2008) 14107. doi:10.1088/0031-8949/9/1/014107.

[14] McNaught, A.Wilkinson, IUPAC Compendium of Chemical Terminology, Blackwell Scientific Publications, Oxford, 2009. doi:10.1351/goldbook.

[15] J. Lyklema, Fundamentals of interface and colloid science. Volume 2: Solid-liquid interfaces. With special contributions by A. de Keizer, B.H. Bijsterbosch, G.J. Fleer and M.A. Cohen Stuart., (1995). http://agris.fao.org/agris-search/search.do?recordID=NL2012065016#.WdsujJiaCM4.mendeley (accessed October 9, 2017).

[16] A.. Dunkin, P.J. Goetz, Ultrasound for Characterizing Colloids — Particle Sizing, Zeta Potential, Rheology, Elsevier, San Diego, CA, 2002. doi:10.1016/S1383-7303(02)80018-7.

[17] H.B. Eral, D.J.C.M. 'T Mannetje, J.M. Oh, Contact angle hysteresis: A review of fundamentals and applications, Colloid Polym. Sci. 291 (2013) 247–260. doi:10.1007/s00396-012-2796-6.

5. RESULTS AND DISCUSSION

5.2 SILICA-GEL PARTICLES

In this Section, besides talking about wrinkled silica-gel particles data, smooth Stöber particles data are shown.

5.2.1 MORPHOLOGY AND SIZE

In figure 5.1 are shown TEM and SEM micrographs of the rinsed wrinkled silica-gel particles. Colloidal particles with an inter-winkled distance in the nano-size range were obtained. SEM micrographs show nanometer roughness detail of particles surface, in agreement with Moon and Lee results [5].

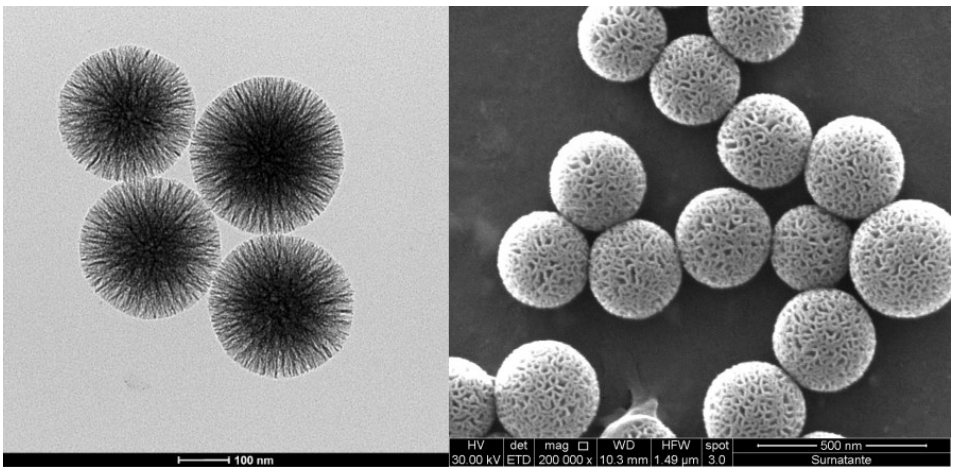

Fig. 5.1. TEM (left) and SEM (right) micrographs of wrinkled silica-gel particles.

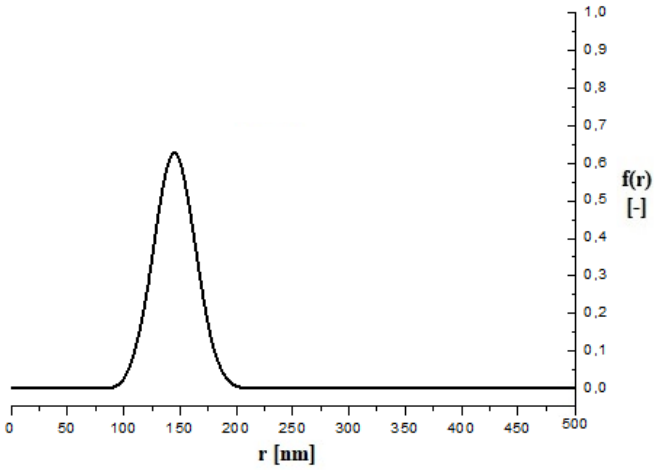

Fig. 5.2. Radius distribution of wrinkled silica-gel particles determined by DLS.

The results of Dynamic Light Scattering (DLS) measurement, reported in Figure 5.2, indicates that the particle radius is in the sub-micrometer range, about 150 nm. The size distribution of wrinkled particles, radius distribution function [6] versus radius, resulted to be rather narrow.

In figure 5.3 are reported SEM images of Stöber silica-gel particles. The average size and standard deviation, 148 nm and 13 nm respectively, were calculated by measuring over 100 radii of particles on SEM micrographs using the ImageJ software.

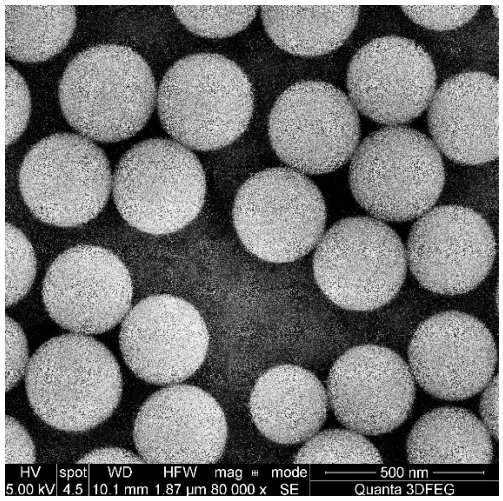

Fig. 5.3. SEM micrograph of Stöber silica-gel particles.

5.2.2 PARTICLES STABILITY IN SURFACTANT SOLUTION

It is well known that silica colloidal particles directly obtained by sol-gel processes are rather hydrophilic and therefore not suitable to be used as Pickering agents on the stabilization of oil phases, such as molten paraffin wax, in aqueous solutions at high pH [7]. Zhu et al has clearly shown this effect for dodecane-water emulsions stabilized by silica particles [8]. It is, however, possible to stabilize oil-water emulsions when reaching the zero-charge surface point of the silica particles, by decreasing pH [9], or by using cationic surfactants as additional stabilizers. In our work, we use sol-gel silica particles negatively charged (pH>3) and so highly hydrophilic, hence in some preparation procedures, cetyltrimethylammonium bromide (CTAB) was added as co-surfactant to reduce the silica surface hydrophilicity. The adsorption of positively charged surfactants on negatively charged surfaces can be followed by zeta potential measurements, which reflect the adsorption of charged species in the Stern plane [10,11]. Hence, the affinity of the chosen surfactant (CTAB) towards the silica surface was evaluated by measuring the zeta potential of silica-CTAB water dispersions at different surfactant concentrations.

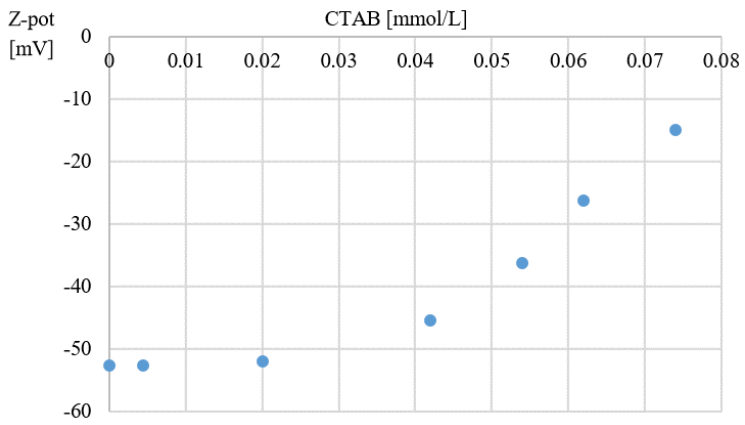

Fig. 5.4. Zeta potential of smooth particles in water dispersion at different CTAB concentrations.

In figure 5.4 the zeta potential (Z-pot) of the aqueous dispersions of smooth Stöber silica-gel particles are plotted against the CTAB concentration. Initially, upon increasing the surfactant concentration the Z-pot of smooth particles remains constant (up to the measured value of 0.020 mmol/L), which indicates no significant adsorption of CTAB. As the CTAB concentration rises (beyond 0.040 mmol/L) the zeta potential value rapidly increases indicating an adsorption of CTAB on the smooth silica-gel surface, and therefore an increase of the silica particles hydrophobicity can be expected. A similar trend was observed by Binks et al [10]. In detail, they measured the Z-pot of commercial silica particles (Ludox HS-30) in 2 % wt particles water dispersion from 0 up to 100 mmol/L CTAB concetration. Z-pot of Ludox particles varied from ∼-36 mV at low CTAB up to 0.1 mmol/L concentration, then increase to ∼-12 mV at 10 mmol/L. In our case, we reach ∼-12 mV at ∼0.7 mmol/L, Hence at a lower concentration than Binks samples. The differences among the two series may be ascribed to the different concentration of the particles within the dispersion: we used ∼0.5 % wt of particles within the aqueous dispersion, against 2 % wt of Binks'sample. Therefore the higher amount of silica surface need a bigger amount of CTAB to significantly change the Z-pot.

Beyond 0.074 mmol/L CTAB, the smooth particles started to flocculate at the last drops addition, after which precipitation occurs within a few seconds. This can be explained by the weak electrostatic repulsion between the silica particles, i.e., at this concentration the dispersions Z-pot is less than -20 mV, and the additional hydrophobic effect of the surfactant alkylic chains extensively adsorbed on the smooth particles, which render them unstable in water [12].

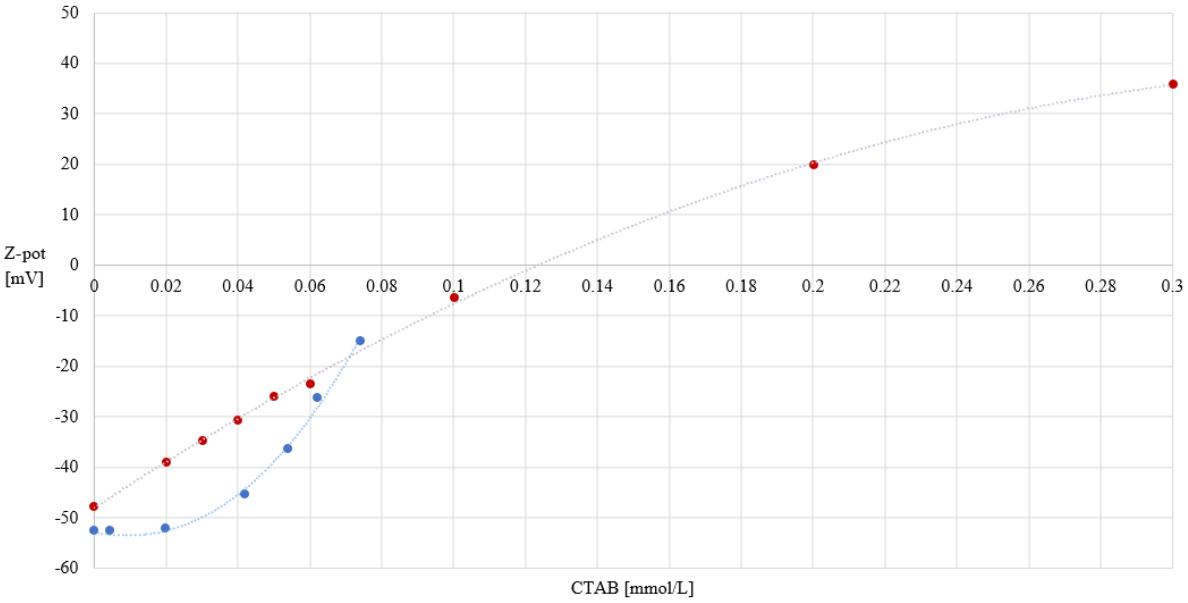

Fig. 5.5. Zeta potential of wrinkled (red) and smooth (blue) silica-gel particles in water dispersion at different CTAB concentrations, with the corresponding trend lines.

Wrinkled particles manifested a completely different behaviour. In figure 5.5 is reported the Z-pot graph versus CTAB concentration (red points) and, for comparison, the Z-pot values of smooth particles (blue points) with corresponding trend lines. For wrinkled particles even at very low CTAB concentration Z-pot increases almost constantly for all the monitored range. Moreover, there is no sign of particles flocculation at every CTAB concentration, even at low surface charge conditions (0.10 mmol/L). The different behaviour of wrinkled particles is due to the different structure of the particles. Likely, the linear-trend of the Z-pot is due to the diffusion of the CTAB into the core of the particles may slow down the Z-pot increase at higher concentration (>0.7mM). While at lower concentration (<0.7mM) the Z-pot is higher than the smooth particles Z-pot, likely because the surfactant molecules does not diffuse so much at this low concentration, hence accumulating at the external surface of the mesoporous particles that possesses smaller external area than the smooth particles surface. The same amount of CTAB molecules on the smooth and mesoporous particles increase the Z-pot the smaller is the external surface of the particles.

5.3 PICKERING EMULSIONS AND COLLOIDOSOMES STRUCTURE

The asymmetrical functionalization for Janus particles production, is carried out in this work by reaction between a silane agent and colloidosomes, that are formed by quenching an O/W Pickering emulsion of melted wax, water and silica-gel particles.

The characteristics of the produced Janus particles directly depend how parent colloidal particles arrange on the wax surface. For instance, penetration depth and cluster formation of the parent colloidal particles has some influence in the final Janus particles properties. The penetration level on the wax droplets will determine the parent particles unprotected area available for the asymmetrical reaction, which ultimately will define the physical-chemical properties of the Janus particles [4,13]; clusters formation at the interface causes the non-homogenous functionalization of the particles within the cluster. The concept is depicted in figure 5.6. Hence, understanding the parameters influencing the yield and how parent colloidal particles arrange at wax-droplet interface is extremely important to fine-tune the chemical and physical characteristics of the resulting Janus particles.

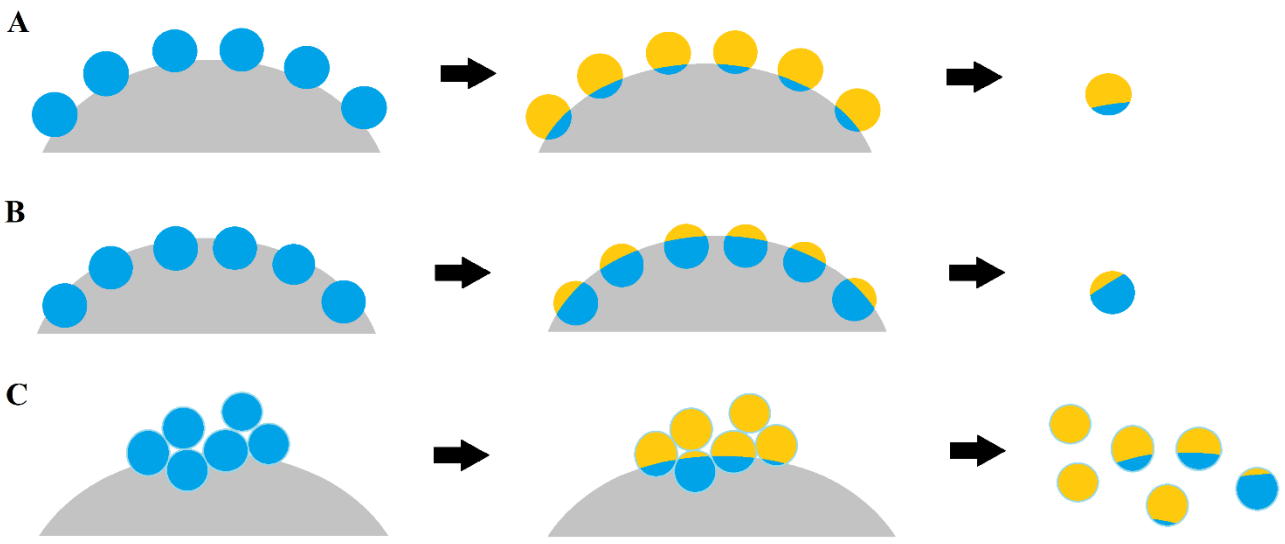

Fig. 5.6. Different arrangement of parent colloidal particles at wax interface. The penetration depth into the particles cause a different extent of functionalized area (A, B). While clusters formation cause heterogeneity in the final properties of Janus particles (C).

Moreover, an important parameter is the amount of particles retained at the wax interface, the yield of the process, defined as the ratio between the particles retained at the interface and the initial amount of particles used.

For this reason a preliminary study was conducted for better understand the emulsification process by using smooth silica-gel particles as Pickering emulsion stabilizer.

5.3.1 EMULSION WITH SMOOTH PARTICLES

Herewith, the preparation procedure is briefly described (for details see subsection 3.3.1). A mixture made of CTAB-particles dispersion in water and melted wax was mixed for 2 minutes, then the emulsion was quenched for solidifying the paraffin and fixing the particles at the wax interface.

We prepared two series of samples: one obtained with high shear mixer that is called “U” series and the other with an overhead stirrer called “O” series. Each sample of the series is characterized by a specific CTAB concentration (0.0044, 0.020, 0.042, 0.054, 0.062 and 0.74 mmol/L). The nomenclature of the samples contains a letter that refers to the type of mixing apparatus, and a number referring to the CTAB concentration used.

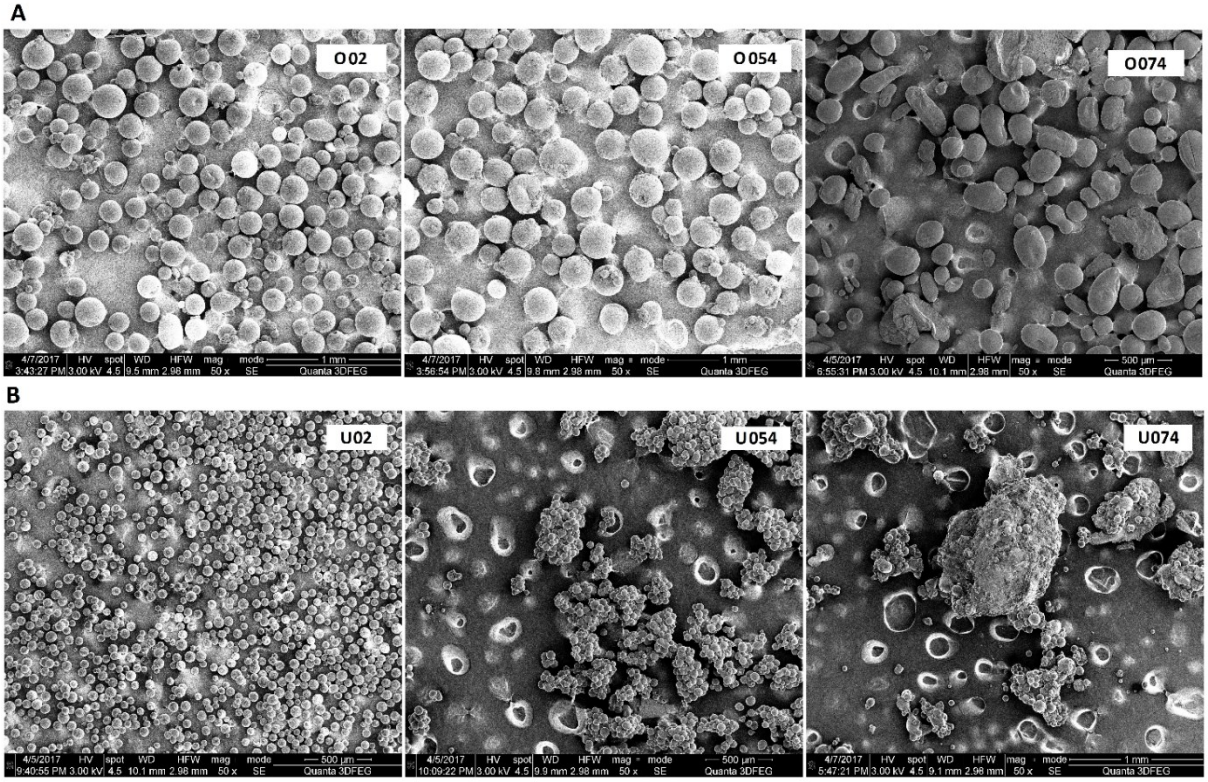

Fig. 5.7. SEM images (magnification 500X) of the solidified colloidosomes obtained with smooth particles dispersions containing 0.020, 0.054 and 0.740 mmol/L CTAB concentration, by using (A) overhead stirrer (the O samples) and (B) high shear dispersers (the U samples).

SEM micrographs of three samples for each series are shown in figure 5.7 and 5.9. Such samples came from CTAB-particles dispersion with 0.020, 0.054 and 0.74 mmol/L surfactant concentrations. These concentrations represent the three important dispersion states of the silica particles. First, at the regime where Z-pot is not affected by the surfactant (-52 mV), hence no CTAB adsorption is taking place; second, when a strong influence of CTAB adsorption is observed and Z-pot increases up to -35 mV and third, when the silica particles start to be unstable in the dispersion and Z-pot value raises above -12 mV (subsection 5.2.2).

In the figure 5.7 the magnification permits to focus on the shape and size of the wax colloidosomes. For the colloidosomes prepared with the overhead stirrer (O series, figure 5.7.A) the shape and size of the colloidosomes remains nearly the same ($\bar{r}$ =51±7 μm, estimated from

statistical analyses of SEM images), except for the highest CTAB concentration (O074), where the majority of the colloidosomes showed non-spherical shape. For the colloidosomes prepared with the high shear disperser (U series, figure 5.7.B) a much smaller size of the colloidosomes was found for all the CTAB concentrations. Figure 5.8 shows also that there was a large variation of the average size (and respective standard deviation) of the colloidosomes prepared with the high shear disperser, as a function of CTAB concentration.

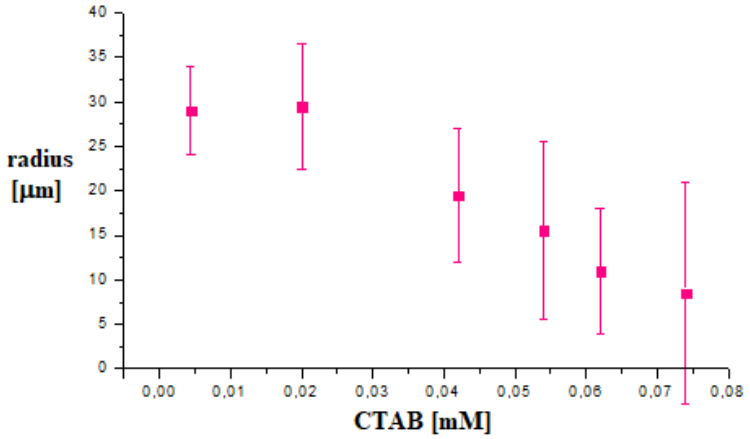

Fig. 5.8. Average radius against CTAB concentration for U series. Bars represent the standard deviation of each sample. The average size and standard deviation were calculated by measuring over 100 radii of colloidosomes on SEM micrographs using the ImageJ software.

The differences among the average size and shape of colloidosomes prepared with the two dispersers can be explained by the different energy level generated by the dispersion system used. As expected the high shear disperser applies high yield stress into the system resulting in much smaller wax droplets, as also observed for other oil-water systems [14] (for theoretical background see subsection 2.4.2).

Another important feature of the colloidosomes is the state of agglomeration of the wax spheres. For the O series no significant aggregation was observed (figure 5.7.A). However, in the U

series, flocculation of the wax particles and formation of aggregates can be observed at CTAB concentration of 0.042mM. These aggregates grow further with the increase of CTAB concentration. Indeed, at the highest CTAB concentrations (0.062, 0.074 mmol/L) the wax sticks at the glass walls of the reaction vessel during the emulsification process.

The surface coverage of the wax by the silica particles in the colloidosomes is a rather important aspect, in the sense that it relates to the efficiency of "protection" of the parent particles to be used for the Janus preparation. Figure 5.9 shows high magnification SEM images with details of the surface coverage of the colloidosomes (already shown in figure 5.9) prepared with the two dispersing methods described above. Regardless of the shape and size of the wax particles, both series showed a monolayer coverage of the wax by the silica particles, except for the O074 for which the surface is covered by clusters and multilayers. The presence of aggregates and multilayers of silica particles is in principle favourable for the stability of the oil (wax) phase, as suggested by many researchers, e.g. Binks et al stated that the most stable emulsions are formed from the most unstable particles dispersions [10]. However, from the point of view of using colloidosomes for the preparation of Janus particles a monolayer coverage is preferred, because in this case any exposed area of the particles will undergo a surface functionalization reaction. Hence, having multilayers will result in heterogeneous functionalization of the silica surface available from the different layers. Only a monolayer and uniform embedding of the silica particles on the wax surface will guarantee the production of uniformly one-side functionalized parent particles. From this point of view, using a CTAB concentration below the aggregation point of the silica dispersions seems to be the best choice.

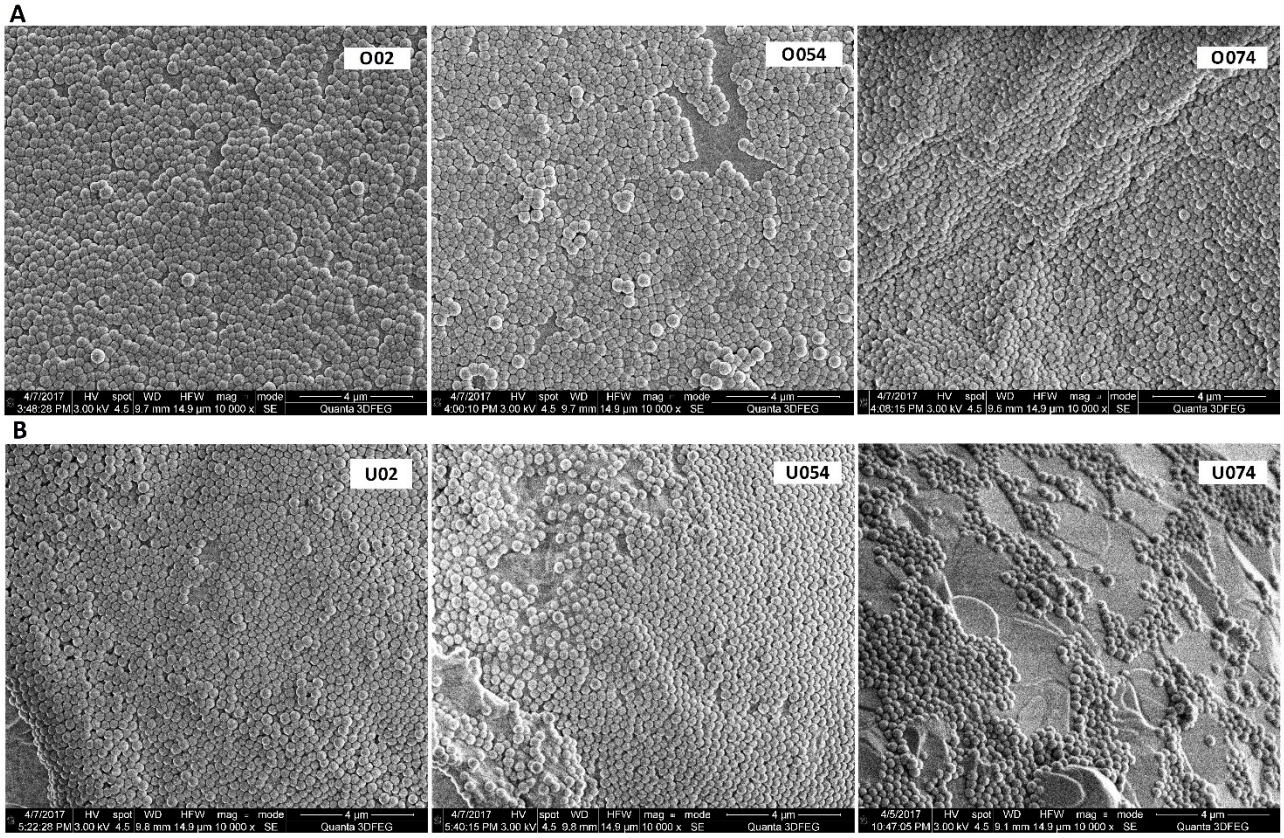

Fig. 5.9. SEM images of the smooth particles coverage on the wax surface for the O series (A) and U series (B), at 0.020, 0.054 and 0.740 mmol/L CTAB concentration (magnification 10,000 X).

Finally, the disperser used also had a big influence on the yield of silica particles embedded in the wax. For the O series the yield was less than 60% for all the CTAB concentrations, except for 0.074 mmol/L, where nearly 80% was reached (see figure 5.10). Instead, for the U series the yields were the highest among all, and nearly 100% was reached for a 0.020 mM CTAB concentration. The yield was evaluated by weighing the residue of particles within the water phase of the emulsion, the difference between this value and the initial amount of particles corresponds to the particles at the wax interface.

In conclusion, the high shear disperser is more suited to the preparation of the silica-wax system thanks to the higher yields of silica particles embedded on the wax. Among the U samples the best coverage of the wax with silica particles (monolayer type) was shown to occur between

the 0.020 and 0.042 mmol/L CTAB, even if at 0.042 mmol/L flocculation of the wax particles is already observed.

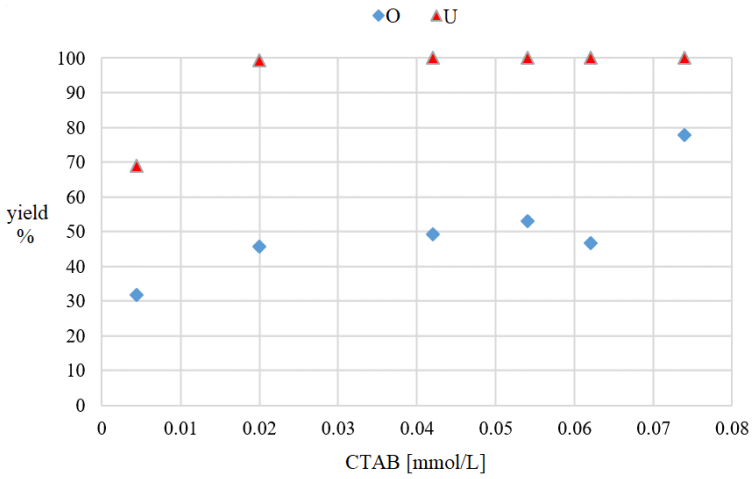

Fig. 5.10. Yield of the silica particles on the wax surface (%) for colloidosomes prepared from smooth particles dispersions with different CTAB concentration, and by using different preparation procedures: U series (red) O series (blue).

Procedure I

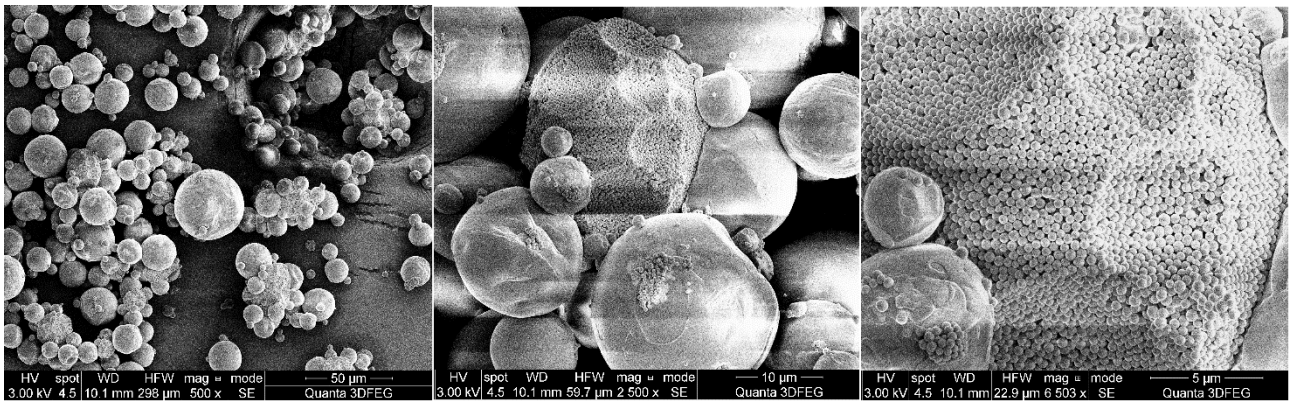

Fig. 5.11. SEM micrographs of the sample prepared with wrinkled particles-CTAB dispersion at 0.17 mmol/L CTAB by high shear mixer. Sample at different magnification (500 X, 2,500 X and 6,503 X) shows: colloidosomes shapes and sizes (left), surfaces of wax covered and not (center), detail of the particles coverage (right).

A mixture of wrinkled particles-CTAB dispersion in water and melted wax was mixed with the high shear for 2 minutes. The mixture was quenched and the solid wax droplets was collected and analysed. In figure 5.11 the SEM micrographs of a sample prepared in a 0.17 mmol/L of CTAB dispersion are shown. At lower surfactant concentration wrinkled particles did not cover the wax interface (subsection 2.4.4). Moreover, even though we can see particles at wax interface in the sample in figure 5.11, only few colloidosomes are completely covered, and the coverage is a multilayer or a thick aggregates layer of particles, not realizing the best condition for further functionalization.

Procedure II

Because of the bad surface coverage obtained from the previous procedure, we decided to use a different approach.

First, dry wrinkled particles were dispersed into melted wax and then water was added and the system mixed with a magnetic stirrer (for details see Procedure II subsection 3.3.2). Then the system was quenched and colloidosomes collected and analysed with SEM. We thought that the addition of particles into the melted wax can improve the yield of the process. Indeed, this approach gave good results (almost 100 % yield) in the works of Jiang et al [2,3,15] using smooth particles.

In figure 5.12, micrographs of the sample thus prepared are shown. In this case, the coverage is more similar to a mono-layer type rather than multilayer or clusters coverage and so better than the previous procedure. Nevertheless, the yield of the process is quite low (<5%). Then, from an industrial point of view, even this procedure is not suitable for Janus particles production.

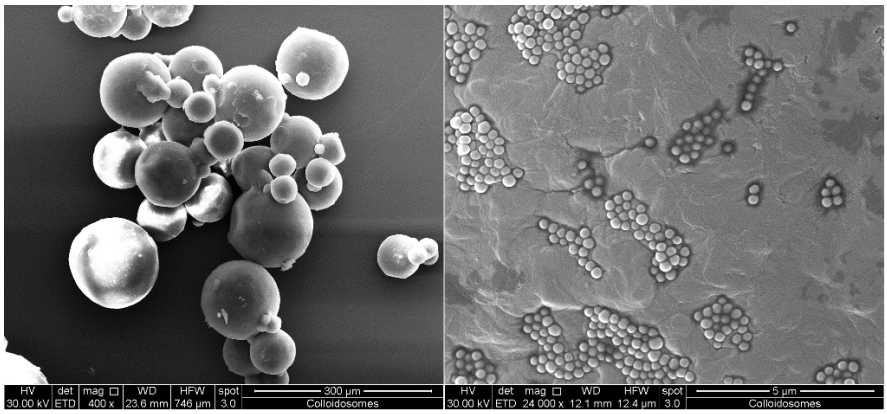

Fig. 5.12. Colloidosomes (left 400X) with surface details (right 24000X) obtained from dispersing wrinkled particles into melted wax and then adding water.

Procedure III

We decided to combine some aspects of the "Procedure I", such as the high shear mixer use, which forms high wax-water interface area, and the surfactant use, for reducing the hydrophilicity of particles, with one aspect from "Procedure II": dispersing dry particles into melted wax.

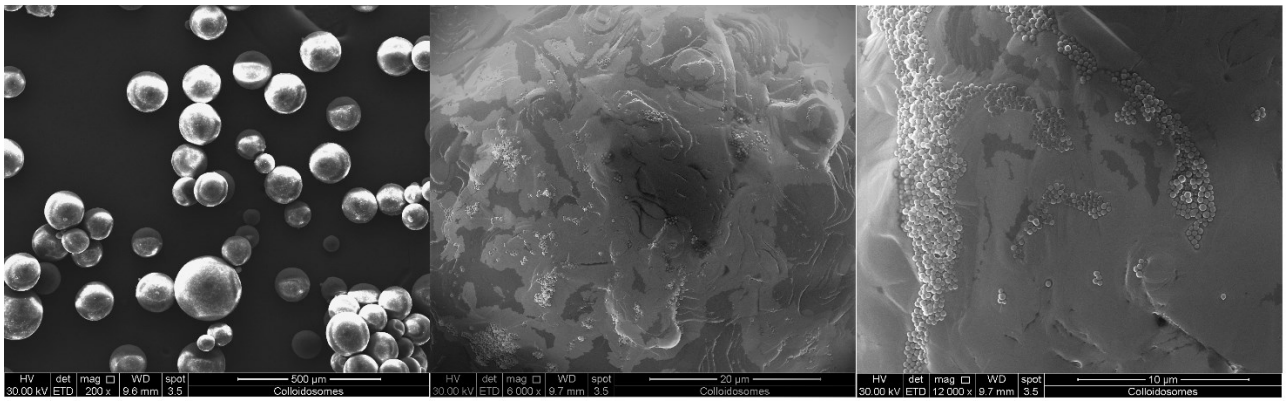

Fig. 5.13. Samples prepared with "Procedure III", (on the left, 200X) are shown the colloidosomes and (on the center and right, 6,000 X and 12,000 X respectively) surface details of the particles coverage.

In this new procedure particles and CTAB were mixed realizing a water solution with a surfactant concentration of 0.12 mmol/L. At this concentration (see Fig.5.5) the Zeta potential is almost 0 mV. Particles may be supposed to be completely covered by CTAB; the hydrophobic interaction may be so maximised so as the adhesion to the wax interface. Subsequently, particles-surfactant dispersion was centrifuged for drying the particles and then dispersed into melted wax by tip-sonication, to completely disperse the particles aggregates. In the end, particles-wax dispersion was poured into water and the emulsification was conducted with high shear mixer. In figure 5.13 are shown the micrographs of such sample where the coverage of the wax is more similar to a monolayer type. The yield of the process was estimated ∼100%, because the supernatant of the O/W emulsion did not contain particles.

5.5 POLYMER GRAFTED JANUS PARTICLES

The properties that hydrophilic-hydrophobic Janus particles imparted to substrates are astonishing, but unfortunately the layer of particles just lay on the substrates without any "strong" bond with it or with the particles themselves. For the reason, is it necessary to improve the mechanical resistance of the particles layer. Therefore, so prepared JWSPs are functionalized further by grafting a polymer chains (maleic anhydride-graft-polypropylene PPgMA) to the hydrophilic part of the Janus particles. In the end, such grafted particles were characterized to test the excellence of the reaction and then the wettability properties of plastic substrate covered by these Janus particles. PPgMA was chosen because of its high compatibility with polypropylene (component of the plastic dispensers). Therefore, this functionalization would be useful to anchor JWSPs to polypropylene surfaces.

In order to graft PPgMA, the JWSOs particles were functionalised with aminopropyltriethoxysilane (APTES). [26] APTES is expected to link to silica particles through condensation reactions of its alkoxy groups with JWSOs particles surface silanols. Moreover a

reaction may be promoted between the APTES amino group and PPgMA maleic anhydride side groups. (for further detail see subsection 3.4.2).

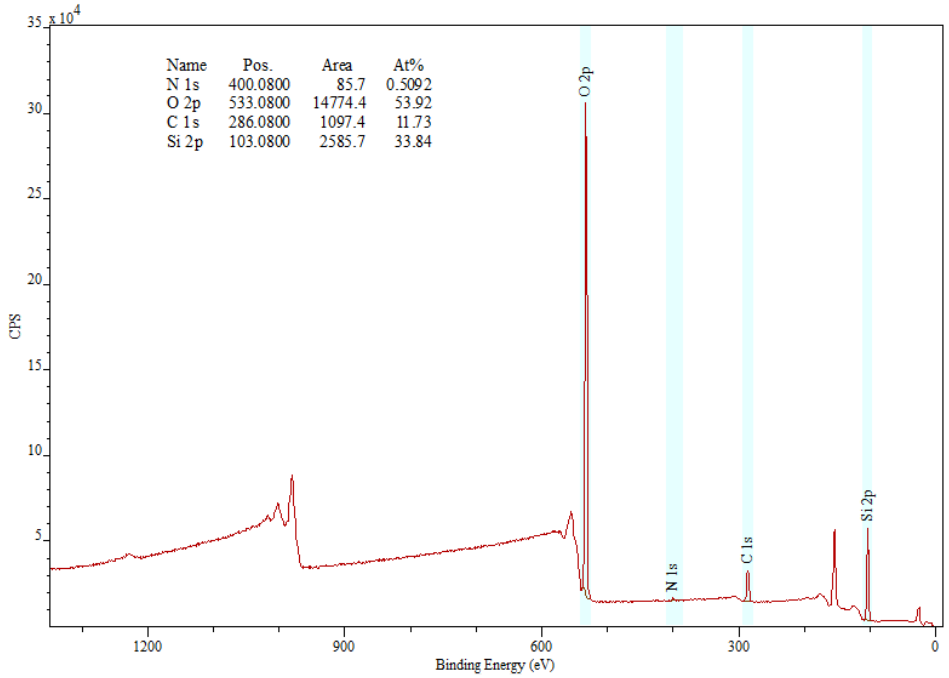

Fig. 5.23. XPS spectrum of Janus particles functionalized with APTES. The weak signal of nitrogen at 400 eV demonstrates reaction between APTES and surface occurred.

In figure 5.23 X-ray Photoelectron Spectroscopy (XPS) spectrum of the Janus-APTES powder is reported along with the percentage of the atoms at the surface. XPS can detect the low amount of nitrogen within APTES molecules bonded to the particles surface, proving the occurrence of the reaction between APTES and silanols groups.

After grafting reaction between PPgMA and APTES-Janus particles, ATR spectrum on powder of the product reaction was carried out. In figure 5.24 the spectra of particles and PPgMA were compared. Almost all the bands of PPgMA were found within the spectrum of the polymer grafted particles, except for the peaks of the carbonyl group (~1700 cm^{-1}), so indicating that some reaction has occurred involving the PPgMA side groups (anhydride groups). All the peaks at wavelengths lower than 1200 cm^{-1} cannot be seen, because they are hidden by the strong signal of the Si-O-Si stretching of the silica-gel particles structure (~1100 cm^{-1}).

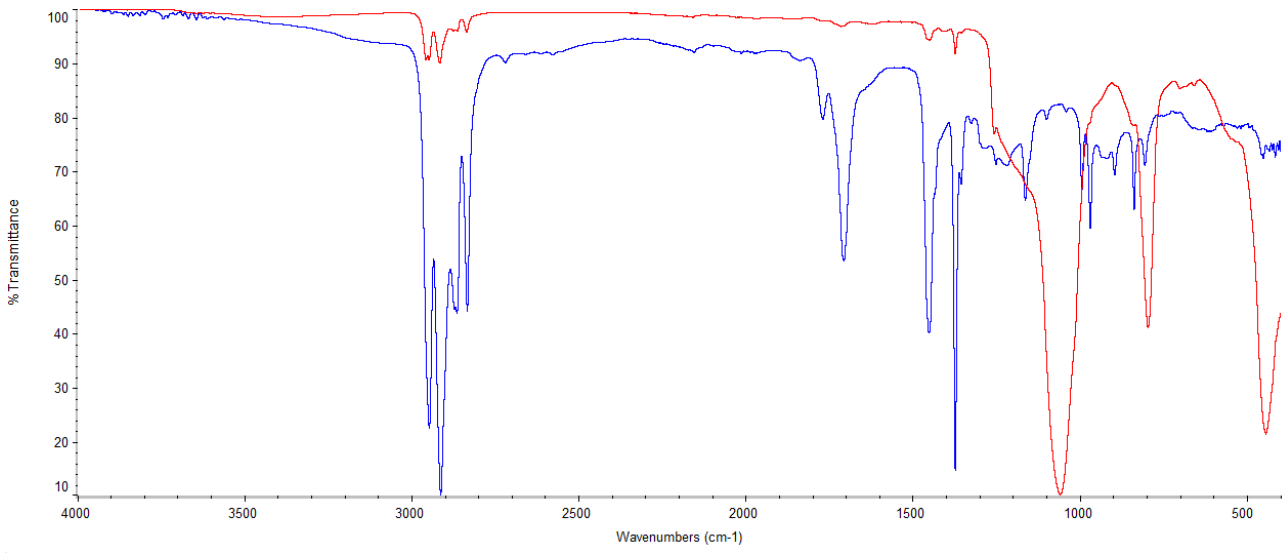

Fig. 5.24. ATR spectra of PPgMA (blue) and PPgMA grafted JWSPs (red).

TEM and SEM micrographs of the PPgMA grafted JWSPs (after all the cleaning procedure, see chapter 3) are reported in figure 5.25. From images A and B we can see the two faces of Janus: the one functionalized with dimethyidichlorisilane, characterized by the clear wrinkled structure, and the polymer grafted part characterized by the greyish ring. In figure C and D, TEM and SEM images shows particles clusters, where the polymer parts (irregular shape objects in figure 5.25.D) linked the silica particles to each other, likely for the insolubility of the PPgMA in xylene at ambient temperature causing a phase separation and formation of such aggregates. Indeed, the characterized samples were prepared from particles dispersion in xylene.

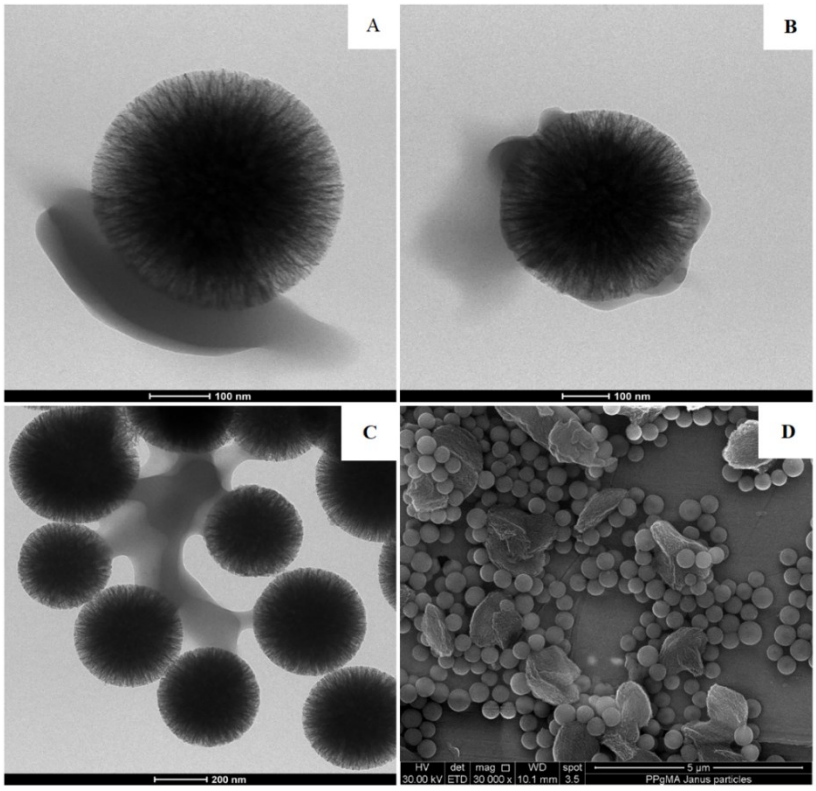

Fig. 5.25. TEM micrographs showing the Janus character of PPgMA grafted wrinkled particles (A, B) and TEM and SEM images showing clusters formation (C, D).

Coating of PPgMA grafted JWSPs on polypropylene were made through dip-coating from particles dispersion in xylene. The coating was analysed by SEM, before and after annealing at 120 °C for 1 h (figure 5.26). From the micrographs of the coating, we can see the particles clusters as shown in figure 5.25.D. Instead, the sample after annealing shows that polymer parts were melted to partially link the polymer parts of adjacent particles and with the polymer substrate.

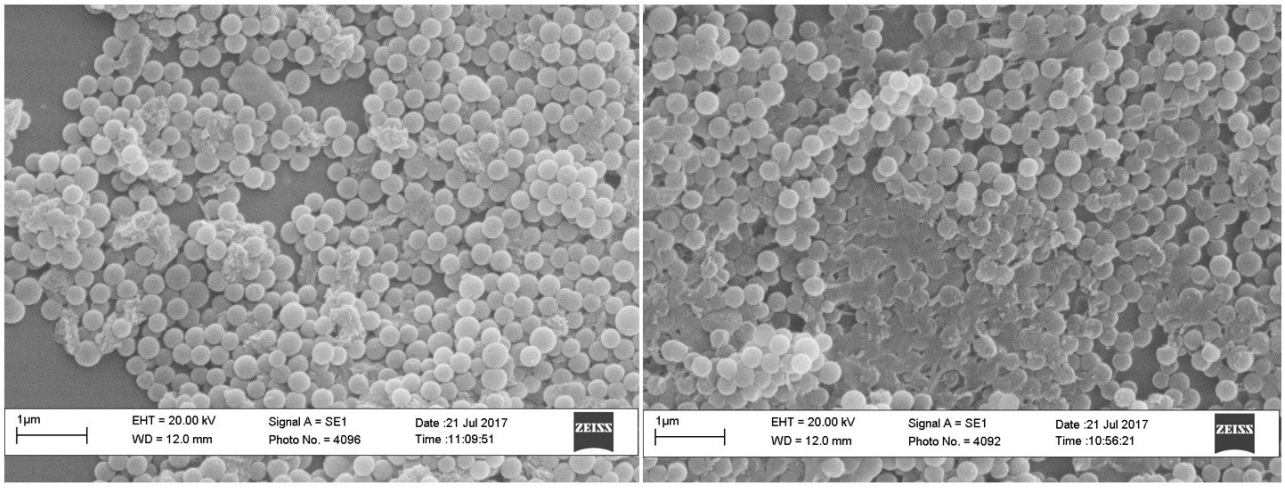

Fig. 5.26. SEM micrographs of the PPgMA grafted JWSPs coating on polypropylene substrate before (left) and after (right) annealing at 120 °C for 1 h.

5.6 RACCOMANDATIONS FOR FUTURE WORK

The wettability properties of the PPgMA grafted JWSPs coating before and after the annealing was qualitatively addressed by using a water droplet. The droplet rolls-off from the surface very easily at inclination < 10° without wetting the coating.

The robustness of the coating was qualitatively evaluated by touching the surface with a finger: the as prepared coating was damaged with the naked eye, the annealed coating does not seem damaged. Indeed, the slippery behaviour of the annealed coating was maintained.

These qualitatively tests must to be followed by quantitatively tests. Wettability properties of such coatings will be analysed by the sessile drop method through different type of solvents, before and after abrasion tests. The abrasion will be made by using cellulose-polystyrene wipe that will erode the coating by rubbing at a constant pressure (~3.5 KPa). Wettability properties were checked after different rubbing length to estimate the robustness of the annealed coating.

References

[1] S. Jiang, Q. Chen, M. Tripathy, E. Luijten, K.S. Schweizer, S. Granick, Janus particle synthesis and assembly, Adv. Mater. 22 (2010) 1060–1071. doi:10.1002/adma.200904094.

[2] L. Hong, S. Jiang, S. Granick, Simple Method to Produce Janus Colloidal Particles in Large Quantity, Langmuir. 22 (2006) 9495–9499. doi:10.1021/la062716z.

[3] S. Jiang, M.J. Schultz, Q. Chen, J.S. Moore, S. Granick, Solvent-free synthesis of janus colloidal particles, Langmuir. 24 (2008) 10073–10077. doi:10.1021/la800895g.

[4] S. Jiang, S. Granick, Controlling the geometry (Janus balance) of amphiphilic colloidal particles, Langmuir. 24 (2008) 2438–2445. doi:10.1021/la703274a.

[5] D.S. Moon, J.K. Lee, Tunable synthesis of hierarchical mesoporous silica nanoparticles with radial wrinkle structure, Langmuir. 28 (2012) 12341–12347. doi:10.1021/la302145j.

[6] D. Montesarchio, G. Mangiapia, G. Vitiello, D. Musumeci, C. Irace, R. Santamaria, G. D'Errico, L. Paduano, A new design for nucleolipid-based Ru(iii) complexes as anticancer agents, Dalt. Trans. 42 (2013) 16697. doi:10.1039/c3dt52320a.

[7] J. Jiang, Y. Zhu, Z. Cui, B.P. Binks, Switchable Pickering Emulsions Stabilized by Silica Nanoparticles Hydrophobized In Situ with a Switchable Surfactant, Angew. Chemie Int. Ed. 52 (2013) 12373–12376. doi:10.1002/anie.201305947.

[8] Y. Zhu, J. Jiang, K. Liu, Z. Cui, B.P. Binks, Switchable pickering emulsions stabilized by silica nanoparticles hydrophobized in situ with a conventional cationic surfactant, Langmuir. 31 (2015) 3301–3307. doi:10.1021/acs.langmuir.5b00295.

[9] H. Hassander, B. Johansson, B. Törnell, The mechanism of emulsion stabilization by small silica (Ludox) particles, Colloids and Surfaces. 40 (1989) 93–105. doi:https://doi.org/10.1016/0166-6622(89)80010-1.

[10] B.P. Binks, J.A. Rodrigues, W.J. Frith, Synergistic interaction in emulsions stabilized by a mixture of silica nanoparticles and cationic surfactant, Langmuir. 23 (2007) 3626–3636. doi:10.1021/la0634600.

[11] D.W. Fuerstenau, Pradip, Zeta potentials in the flotation of oxide and silicate minerals, Adv. Colloid Interface Sci. 114 (2005) 9–26. doi:https://doi.org/10.1016/j.cis.2004.08.006.

[12] Y. Liu, M. Tourbin, S. Lachaize, P. Guiraud, Silica nanoparticles separation from water: Aggregation by cetyltrimethylammonium bromide (CTAB), Chemosphere. 92 (2013) 681–687. doi:https://doi.org/10.1016/j.chemosphere.2013.03.048.

[13] E. Sharifzadeh, M. Salami-Kalajahi, M. Salami Hosseini, M.K. Razavi Aghjeh, S. Najafi, R. Jannati, Z. Hatef, Defining the characteristics of spherical Janus particles by investigating the behavior of their corresponding particles at the oil/water interface in a Pickering emulsion, J. Dispers. Sci. Technol. 38 (2017) 985–991. doi:10.1080/01932691.2016.1216861.

[14] P. Walstra, Principles of emulsion formation, Chem. Eng. Sci. 48 (1993) 333–349. doi:10.1016/0009-2509(93)80021-H.

[15] S. Jiang, S. Granick, Janus balance of amphiphilic colloidal particles., J. Chem. Phys. 127 (2007) 161102. doi:10.1063/1.2803420.

[16] S. Jiang, Q. Chen, M. Tripathy, E. Luijten, K.S. Schweizer, S. Granick, Janus particle synthesis and assembly, Adv. Mater. 22 (2010) 1060–1071. doi:10.1002/adma.200904094.

[17] X. Bai, C.H. Xue, S.T. Jia, Surfaces with Sustainable Superhydrophobicity upon Mechanical Abrasion, ACS Appl. Mater. Interfaces. 8 (2016) 28171–28179. doi:10.1021/acsami.6b08672.

[18] A. Yildirim, H. Budunoglu, B. Daglar, H. Deniz, M. Bayindir, One-pot preparation of fluorinated mesoporous silica nanoparticles for liquid marble formation and superhydrophobic surfaces, ACS Appl. Mater. Interfaces. 3 (2011) 1804–1808. doi:10.1021/am200359e.

[19] C. Pereira, C. Alves, A. Monteiro, C. Magén, A.M. Pereira, A. Ibarra, M.R. Ibarra, P.B. Tavares, J.P. Araújo, G. Blanco, J.M. Pintado, A.P. Carvalho, J. Pires, M.F.R. Pereira, C. Freire, Designing novel hybrid materials by one-pot co-condensation: From hydrophobic mesoporous silica nanoparticles to superamphiphobic cotton textiles, ACS Appl. Mater. Interfaces. 3 (2011) 2289–2299. doi:10.1021/am200220x.

[20] H.B. Eral, D.J.C.M. 'T Mannetje, J.M. Oh, Contact angle hysteresis: A review of fundamentals and applications, Colloid Polym. Sci. 291 (2013) 247–260. doi:10.1007/s00396-012-2796-6.

[21] T.G. Cha, J.W. Yi, M.W. Moon, K.R. Lee, H.Y. Kim, Nanoscale patterning of microtextured surfaces to control superhydrophobic robustness, Langmuir. 26 (2010) 8319–8326. doi:10.1021/la9047402.

[22] J. Zhi, L.Z. Zhang, Durable superhydrophobic surfaces made by intensely connecting a bipolar top layer to the substrate with a middle connecting layer, Sci. Rep. 7 (2017) 1–12. doi:10.1038/s41598-017-10030-9.

[23] K. Zhang, X. Yang, N. Zhu, Z.C. Wang, H. Yan, Environmentally benign paints for superhydrophobic coatings, Colloid Polym. Sci. 295 (2017) 709–714. doi:10.1007/s00396-017-4053-5.

[24] J. Bravo, L. Zhai, Z. Wu, R.E. Cohen, M.F. Rubner, Transparent Superhydrophobic Films Based on Silica Nanoparticles Transparent Superhydrophobic Films Based on Silica Nanoparticles, 23 (2007) 7293–7298. doi:10.1021/la070159q.

[25] H. Wang, J. Fang, T. Cheng, J. Ding, L. Qu, L. Dai, X. Wang, T. Lin, One-step coating of fluoro-containing silicananoparticles for universal generation of surface superhydrophobicity, Chem. Commun. (2008) 877–879. doi:10.1039/B714352D.

[26] W.-C. Liaw, P.-C. Huang, C.-S. Chen, C.-L. Lo, J.-L. Chang, PPgMA/APTS compound coupling compatabilizer in PP/clay hybrid nanocomposite, J. Appl. Polym. Sci. 109 (2008) 1871–1880. doi:10.1002/app.28294.

ACKNOWLEDGMENT

During my PhD project, I spent 6 months at the Chemical Engineering and Chemistry Department (Physical Chemistry Section) of TU/e, supervised by Dr. Esteves. During this period I understand the emulsification issues of colloidosomes by using smooth particles. This step of the thesis was of crucial importance for the success of the Janus particles synthesis.

Many thanks to Dr. Catarina de Carvalho Esteves for her tips and to cheer me up and above all for caring more about my personal growth than her success, popularity or visibility.